PHYSIK DEPARTMENT

Molecular principles governing the organization of active actin networks

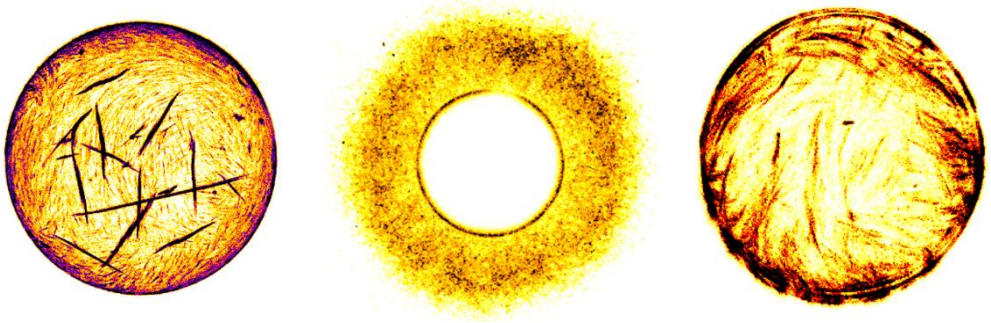

Dissertation by

Walter Philip Bleicher

Technische Universität München

Physik Department

Lehrstuhl für Zellbiophysik E27

Molecular principles governing the organization of active actin networks

Walter Philip Bleicher

Vollständiger Abdruck der von der Fakultät für Physik der Technischen Universität München zur Erlangung des akademischen Grades eines

Doktors der Naturwissenschaften (Dr. rer. nat.)

genehmigten Dissertation.

Vorsitzender:	Prof. Dr. Martin Zacharias
Prüfer der Dissertation:	1. Prof. Dr. Andreas Bausch
	2. TUM Junior Fellow Dr. Zeynep Ökten

Die Dissertation wurde am 03.12.2020 bei der Technischen Universität München eingereicht und durch die Fakultät für Physik am 20.01.2021 angenommen.

Abstract

Reconstituted systems of active actin networks are a powerful tool to study the interactions of the various cytoskeletal proteins. On the one hand, imaging of fluorescently labeled proteins in biomimetic frameworks provides insights in the elusive field of actin dynamics without the limitations set by the complex and noisy background of the cell. On the other hand, the field is moving towards the formation of synthetic cells emulating the ill-understood autonomous movement of living matter. This thesis provides important steps towards this goal by achieving multiple requirements of reconstructed motility for the first time: Firstly, to build an active actin turnover maintained by the nucleator formin and the recycling proteins cofilin and CAP1. This is described and quantified in depth in the first part of this thesis. Surprisingly, a synergistic relationship of the nucleators Arp2/3 and formin emerged in these globally treadmilling networks. Here, filaments elongated by formin protected the dense Arp2/3 networks from debranching by locally depleting cofilin through binding. In the second part, the molecular details underlying these processes were further quantified by measuring the binding affinities of the involved proteins by microscale thermophoresis (MST) and kinetics by nucleotide exchange assays. Together, a complete mechanism can be postulated by which cells maintain an active pool of monomers while regulating local concentration of monomers and binding partners autonomously by a growth-depletion feedback. In the final part of this thesis, actin turnover is coupled with contractions mediated by the motor protein myosin and the networks are adhered to biomimetic supported lipid bilayers (SLB). In this cortex-like system, intra-bundle contractions could be observed which led to the formations of extensile clusters. The expansile actin networks described here provide a way for the cortex to break the symmetry and are reminiscent of structures found in cells. This important correlation is of equal importance to our understanding of cellular motility as it is to advance the attempts of creating artificial cells.

Zusammenfassung

Rekonstruktionen aktiver Aktinnetzwerke in vitro sind ein wichtiges Werkzeug zur Untersuchung von Interaktionen der zahlreichen Proteine des Zellskeletts. Einerseits kann man durch die Bildgebung von fluoreszenzmarkierten Proteinen Einsichten in das Gebiet der Aktindynamik gewinnen, wenn sie in biomimetische Umgebungen eingebaut sind – und zwar ohne die optischen

Limitierungen, die der komplexe, signalstörende Hintergrund der Zelle hervorruft. Andererseits schreitet das Forschungsfeld voran, um synthetische Zellen nachzubauen, welche die wenig verstandenen Bewegungen lebendiger Materie imitieren. Diese Dissertation liefert wichtige Schritte zur Verwirklichung diese Ziels, da hier zum ersten Mal mehrere Anforderungen zur Rekonstruktion zellulärer Motilität erfüllt wurden: Einerseits, den aktiven Umsatz von Aktinmonomeren, der durch den Nukleator Formin und die Recyclingproteine Cofilin und CAP1 aufrechterhalten wird. Dies wird im ersten Teil dieser Arbeit im Detail beschrieben und quantifiziert. Überraschenderweise konnte eine synergetische Beziehung zwischen den Nukleatoren Arp2/3 und Formin in diesen Netzwerken entdeckt werden. Hierbei werden die dichten, von Arp2/3 polymerisierten Netzwerke durch die elongierten Filamente, die von Formin gebildet werden, vor Disassemblierung durch Cofilin geschützt, indem freies Cofilin durch die Bindung an die elongierten Filamente lokal dezimiert wird. Im zweiten Teil werden die molekularen Details dieser Vorgänge entschlüsselt indem die Bindeaffinitäten der beteiligten Proteine mithilfe von Mikroskala-Thermophorese (MST), sowie kinetische Beiträge über Nukleotid-Austausch-Assays bestimmt werden. Zusammen erlaubt dies die Formulierung eines mechanischen Gesamtbildes, wie Zellen einen Vorrat aktiver Monomere für globales Treadmilling aufrechterhalten und wie lokal die Konzentrationen von Monomeren und Bindepartnern autonom durch ein Feedback der Wachstums-Depletion reguliert werden. Im Schlussteil dieser Arbeit wird der Aktin-Umsatz mit Kontraktionen gekoppelt, vermittelt durch das Motorprotein Myosin und zusätzlich das Netzwerk an eine biomimetische Lipiddoppelschicht geankert. In diesem Kortex-ähnlichen System konnten Kontraktionen innerhalb eines Bündels und das Auftreten expansiver Aktin-Kluster beobachtet werden. Sich ausdehnende Netzwerke dieser Art ermöglichen es dem Kortex die Symmetrie zu brechen und erinnern an Strukturen, die in Zellen zu finden sind. Diese wichtige Korrelation ist nicht nur von Bedeutung für unser Verständnis von zellulärer Motilität, sondern auch ein wichtiger Schritt zur Rekonstruktion artifizieller Zellen.

Excerpts of this thesis have appeared in the following publications:

Bleicher, P., Nast-Kolb T., Sciortino, A., de la Trobe Y. A., Pokrant T., Faix J. & Bausch, A. R. Intra-bundle contractions enable extensile properties of active actin networks. (Submitted)

Bleicher, P., Sciortino, A. & Bausch, A. R. The dynamics of actin network turnover is self-organized by a growth-depletion feedback. Sci. Rep. 10, 6215le (2020).

Acknowledgements:

Ich bedanke mich bei meinem Doktorvater Professor Dr. Andreas Bausch, der mich auf der ganzen abenteuerlichen Reise meiner Doktorarbeit begleitet hat. Danke für Deine unermüdliche Fähigkeit, Dich für Wissenschaft zu begeistern und die Unterstützung, ohne die gerade in den schwierigeren Projekten überhaupt nichts vorangegangen wäre.

Mein Dank gilt außerdem sämtlichen Mitarbeitern der Lehrstühle E22 und E27. Zuallererst natürlich meinen ehemaligen und aktuellen Bürokollegen im „Jungle“: Alfredo Sciortino, der mir große Unterstützung bei allen quantitativen Fragen hat zukommen lassen, und Katharina Dürre, die mir so manches Einkapseln ermöglicht hat, Felix Keber und Dominik Ritzer für die gute Atmosphäre im Büro und die ein oder andere fachliche oder nicht-fachliche Diskussion.

Joanna Deek und Katarzyna Tych danke ich für unzählige gute Ratschläge, all die guten Lunchies, das Korrekturlesen von Papern und Kapiteln dieser Arbeit, und für die großartige Zeit, die ich nicht missen möchte. Für ihre Unterstützung und zahlreiche Ganggespräche bedanke ich mich bei meinen Kollegen Henry Dehne, Ben Buchmann, Timon Nast-Kolb, Pablo Fernandez, Fabian Hecht, Ryo Suzuki, Martina Lindauer, Etienne Loiseau, Leone Rossetti, Samuel Randriamanantsoa, Fabian Engelbrecht und Iris Ruider.

Eine besondere Erwähnung gehört auch meinen ehemaligen Studenten, Anja Wurzer, Jannis Lawatschek, Hanna Brunner, Melina Grasmeier, Christoph Deisenhofer und inoffiziell auch Yu Alice de la Trobe. Ihr habt mir mit eurer hervorragenden Arbeit und eurem Fleiß wirklich weitergeholfen.

Liebe TAs, Monika Rusp-Post, Gabriele Chmel, Karin Vogt und Thi-Hieu Ho, ohne eure unschätzbare Hilfe wäre der Laboralltag nicht zu bewältigen, die vielen Proteine, Plasmide und all die anderen Dinge, die ihr für uns bereitstellt. Ganz besonders möchte ich mich auch bei Katerina Girgensohn bedanken, die mich mit ganz viel Freundlichkeit und Zuverlässigkeit in all den ungeliebten organisatorischen und bürokratischen Angelegenheiten unterstützt hat.

Abschließend bedanke ich mich bei meiner Familie, meinen Eltern und meiner Schwester, die mir die Geduld und moralische Hilfestellung gegeben haben die ich bis zum Ende gebraucht habe. Vielen Dank auch an Roman, der sich so manches allabendliches Gejammer über verschüttete Proteine und geplatzte Vesikel hat anhören dürfen.

Contents

1. Introduction

The ability of mammalian cells to actively change their shape is at the heart of many fundamental physiological functions. Cellular motility, cell division, as well as exo- and endocytosis come to mind among those processes. For a cell to be able to stretch or retract, form protrusions or actively transport cargo material throughout the cytosol requires the capability to tightly control its very own mechanical properties. This is accomplished by the characteristics of active biological matter, which can only be fully understood by unraveling the underlying molecular mechanisms.

The actin cytoskeleton is the essential scaffold of cellular dynamics and has been studied intensively since many years, yet our understanding of the details on a molecular level remains elusive. Although the integration of fluorescent dyes in living cells[1] has moved the field into a new era, *in vivo* studies are limited by the optical resolution of single actin filaments. The cytosol is tightly packed with actin as it is the most abundant protein in the cell at concentrations of up to 500 µM, which makes it hard to distinguish between different actin structures without respective antibodies[2]. Other labeling methods like LifeAct or Phalloidin can lead to significant defects because of their invasive interactions with the actin cytoskeleton[3]. Thus, actin dynamics are best studied in reconstituted systems.

A solution of reconstituted actin monomers above a critical concentration in the presence of ATP and the bivalent cation Mg^{2+} as a cofactor is able to spontaneously nucleate actin oligomers that act as seeds to polymerize into filaments by associating further monomers to their ends, thereby forming an actin network. Actin filaments are polar and have a faster polymerizing end - the barbed end - and an end with a slower on-rate and a faster off-rate called the pointed end. Due to the hydrolysis of ATP in filamentous actin, there is more ADP- and ADP-Pi-actin located at the pointed end of the filament, conversely there is mostly ATP-actin at the barbed ends, where fresh, ATP bound monomers are built in fastest. In equilibrium, the barbed end elongation rate equals the pointed end net depolymerization rate and the total length of the filament remains constant. This process is called treadmilling and is fundamental for the inherent dynamics of active actin networks (Figure 1.1).

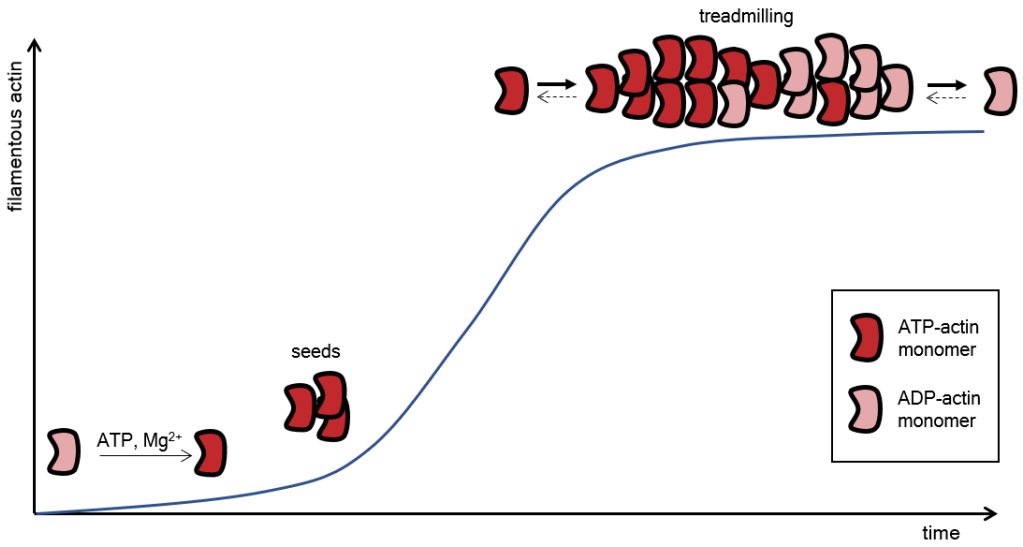

Figure 1.1: Typical actin polymerization curve. In the presence of ATP and the cofactor cation Mg^{2+}, actin can nucleate into oligomers if the concentration of actin monomers is above the critical concentration c_c. These oligomers act as seeds that polymerize into filaments, thus forming a network of filamentous actin. Due to the high free energy barrier of monomers associating with one another in the absence of seeds, the nucleation step is hereby rate limiting. Once the seeds have formed, elongation of filaments occurs more rapidly. The system equilibrates once the concentration of filamentous actin reaches their plateau value. Here the net elongation at the barbed ends equals the net depolymerization at the pointed ends and the length of the individual filaments remains constant, a process called actin treadmilling.

1.1 Reconstitution of global actin turnover

In cells, actin treadmilling is regulated by a myriad of actin binding proteins leading to a global turnover throughout the cell that is collectively competing for a common monomer pool. Depending on the requirements the actin network can be locally contracted, crosslinked, disassembled or polymerized, enabling the network to meet the contradicting properties of stability and dynamics. To mimic this global turnover in a reconstituted system, first of all a minimal set of actin binding proteins has to be identified.

Cofilin, specifically human cofilin 1, is a 15 kDa protein that is involved in the regulation of actin disassembly. Cofilin has the ability to bind actin monomers and also bind to the sides of actin filaments, effectively decorating the filament. Hereby cofilin prefers ADP bound monomers over ATP bound monomers, consequently it decorates preferentially the pointed ends of filaments and is more sparsely found at the barbed ends. Filaments can be saturated by cofilin when the cofilin concentration is high enough relative to the actin concentration. Binding by cofilin changes the twist[4] of the filament by inducing the dissociation of ions that were originally associated to the filament[5]. Concurrently with this, the bending stiffness of actin filaments decreases 5-fold where cofilin is bound[6],

leading to a more flexible filament. Surprisingly, severing of filaments can occur when a filament is partially decorated by cofilin[7]. This happens at the transition sites between decorated and undecorated parts of the filaments, most likely due to the mechanical asymmetry of the filament (Figure 1.2). This asymmetry occurs only at partial decoration, not when the filament is undecorated or completely saturated with cofilin. Additionally, the filament has to be able to freely fluctuate, as thermal energy drives the severing at the bare and decorated boundaries. Consequently, bundled or crosslinked filaments, or filaments that are immobilized by surface anchors that attach to filament sides interfere with the severing activity of cofilin. This can be partially compensated by the presence of the motor protein myosin which synergizes with cofilin by inducing stresses on filaments or bundles to disassemble them even when crosslinked[8].

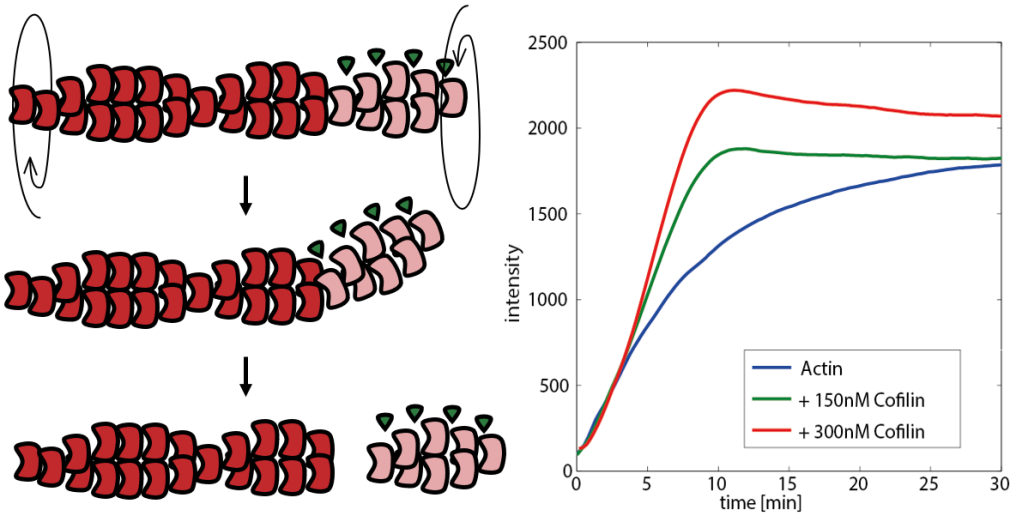

Figure 1.2: Severing activity of cofilin. Binding of cofilin induces a change in the filament twist and increases the bending flexibility of filaments. The mechanical asymmetry leads the way for severing at the boundaries between decorated and bare parts of the filament, induced by thermal fluctuations. Severing creates new nucleation seeds and consequently the number of barbed ends in the network. Thus, at concentration below filament saturation, increasing the cofilin concentration also increases the overall dynamics and shortens the time until the polymerization reaction reaches its plateau and equilibrates. Here, the polymerization is monitored by means of the fluorescence of pyrene labeled monomers, which increases with the amount of filamentous actin.

Another effect of cofilin is the enhancement of the overall dynamics by increasing the on- and off-rates on both filament ends, albeit altering the rates in favor of depolymerization[9]. There is a direct effect on the fraction of monomers in the equilibrated state depending on the cofilin concentration, as the fraction of unpolymerized actin increases with increasing cofilin concentration[10]. Depolymerizing actin is an important factor for intracellular dynamics, as

continuous global actin turnover can only be achieved by recycling monomers and maintaining a pool of polymerizable monomers[11].

To be able to recycle monomers that have been depolymerized by cofilin, the dephosphorylated ADP has to be exchanged with fresh ATP. However, the nucleotide exchange is strongly inhibited by binding of cofilin, as cofilin stabilizes the ADP state of monomers[12]. CAP1 - specifically the C-terminally tail of CAP1 - interacts with monomers by catalyzing the nucleotide exchange of ADP actin even when bound with cofilin[13]. Additionally, activity mediated by the N-terminal domain of CAP1 increases the overall depolymerization rate of cofilin by two orders of magnitude[14,15]. Thus, in the presence of CAP1 the biphasic activity of cofilin due to stabilization by saturation of filaments is altered, as cofilin decorated actin is rapidly disassembled by pointed end depolymerization.

These insights constitute the basis of recreating cellular dynamics in vitro. The goal achieved in this thesis was to combine the localized polymerization of actin while upkeeping an active pool of monomers, effectively forming a turnover cycle. The surprisingly high dynamics achieved in this manner are a critical step towards the formation of artificial cells, as the localized turnover of actin provides forces which could ultimately lead to the deformation and motility of reconstituted cytosolic vesicles.

1.2 Reconstitution of a biomimetic actin cortex

The key to precisely controlled morphological changes is the actin cortex[16]. Present in most mammalian cells, the cellular cortex is a layer of membrane bound actin, myosin and over 150 actin binding proteins[17]. Among these proteins are the previously mentioned regulators of actin turnover[18,19]. Turnover and recycling of monomers has been shown to be critical, since depletion of cofilin leads to an increase in the thickness of the actin cortex. This suggests that the cortex is in a steady-state, constantly maintaining a well-balanced fraction of polymerized and depolymerized actin. Additionally, the polymerization of actin at the cortex is controlled by nucleators and elongators[20]. Among those proteins formin (mDia1), the Arp2/3[21] complex and VASP[22,23] are found, which are responsible for elongated[24], branched[25] and bundled[26,27] actin architectures respectively.

One requirement for mechanical stability and the ability to maintain cortical tension is the crosslinking of bundles of actin into more rigid structures[28]. Many different crosslinkers are found within the cortex, among which fascin[29] is

responsible for the crosslinking of parallel bundles, while α-actinin can form anti-parallel structures[30]. Additionally, the actin network needs to be linked to the membrane to be able to transmit forces, for example to accomplish processes like the formation of blebs[31,32]. The final and crucial component not only necessary to maintain cortical tension but also drive the turnover of actin monomers and active shape deformations too is the motor protein myosin. Myosin actively exerts tension by pulling on contractile fibers[33] (Figure 1.3). How myosin organizes the cortex however remains poorly understood and lack of experimental proof impedes the proposal of molecular mechanisms that underly all cortical functions.

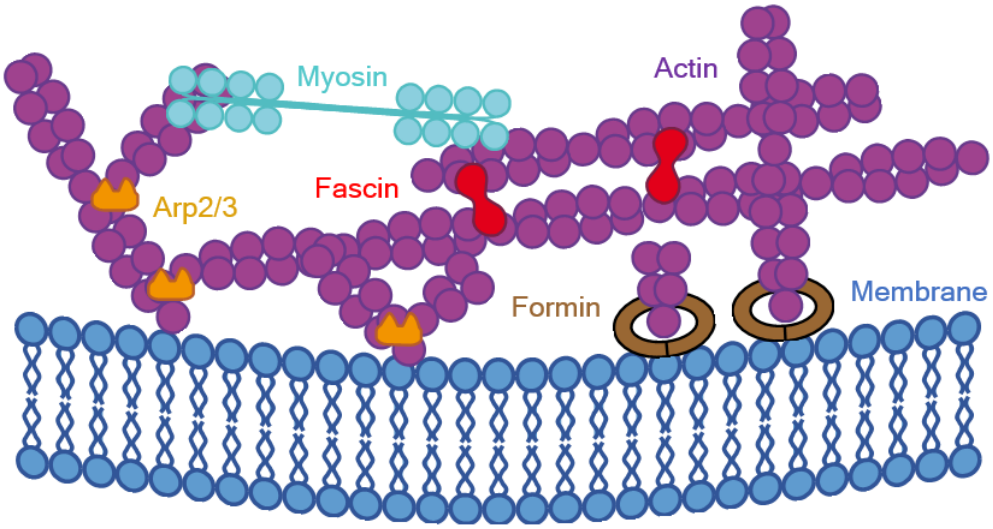

Figure 1.3: Organization of the actin cortex. Actin binding proteins that have been identified in the organization of the cortex are nucleators like Arp2/3 (orange) which forms branched actin networks and formin (brown), mediating elongated structures. Fascin (red) acts as a crosslinker of filaments, thus modulating the stiffness of the network. Myosin (cyan) creates cortical tension via contractions.

The goal of this thesis was to study this elusive molecular basis of actin organization in active networks. Reconstructing a biomimetic cortex which fulfills the demands of an active actin turnover by global treadmilling and contractility mediated by the motor protein myosin is a powerful tool, first established in the experiments described here. By reconstituting these networks in vitro, it is possible to image individual components involved in the network organization by high-resolution fluorescent microscopy techniques in a minimal set of proteins and without the noisy background of the cell.

By using different model systems such as functionalized agarose microspheres, giant unilamellar vesicles and supported lipid bilayers, the turnover and reorganization by myosin can be studied in a biomimetic manner. This data is

supplemented with binding studies that quantify the molecular interactions of the individual components. Taken together, it was possible to discover and quantify fundamental mechanisms such as a synergetic relationship of the nucleators formin and Arp2/3 when colocalized on the same surface, surprisingly guided by a growth-depletion feedback. Another molecular mechanism discovered in these networks were contractions on an intra-bundle level which enabled the extensile properties of active actin networks. These findings contribute to our current understanding of the complex processes that drive the motility of cells. Additionally, the ability to reconstitute active actin turnover in vitro is an important step towards the formation of artificial, autonomously moving cells.

2. Material and Methods

2.1 Molecular Cloning

Several protein constructs were amplified via polymerase chain reactions (PCR) and subsequently inserted in a standard plasmid. For His-Tagged constructs like formin, a pET28b(+) vector was chosen utilizing the His-Tag already present on the plasmid, for other constructs a pGEX-6P2 vector was used. To create fusion constructs of actin binding proteins with fluorescent proteins, PCR primers were designed to create an overlapping DNA sequence between the two fragments.

Name	Sequence (5'-3')	Restrictase
mDia1 _f	GCG CGA ATT CAA AAA TGA AAT GGC AAG CCT GAG C	EcoRI
mDia1_r	CAG TTC ACC GCT TGA GCC GCT TGC ACG ACC	N/A
GFP_f	GGC TCA AGC GGT GAA CTG GTG CCG CGC GGT	N/A
GFP_r	GGC CCT CGA GTT ATT TAT ACA GTT CGT CCA TAC C	XhoI
hCof_f	ATA TAT GGA TCC ATG GCC TCC GGT GTG GCT	BamHI
hCof_r	CGG CAC CAG GCC GCT GCT CAA AGG CTT GCC	N/A
mCherry_f	AGC AGC GGC CTG GTG CCG CGC GGC AGC CAT	N/A
mCherry_r	GGC CGA ATT CTT ACT TGT ACA GCT CGT CCA TGC C	EcoRI
CAP1_N_f	CCC GGA ATT CAT GGC TGA CAT GCA AAA TCT TGT A	EcoRI
CAP1_N_r	AGA TGG CAA TCC ACT CAG TTC TTT TGC CAC	N/A
CAP1_C_f	CTG AGT GGA TTG CCA TCT GGA CCC TCT GTG	N/A
CAP1_C_r	GAG ACT CGA GTT ATC CAG CGA TTT CTG TCA CTG T	XhoI

Table 2.1: Primers used in the production of fusion proteins.

The two fragments were amplified in a first PCR with the primers containing the overlaps. In a second PCR reaction using the primers flanking the full-length sequence a covalently coupled construct was produced.

The obtained PCR fragments were cut with the corresponding restriction enzymes listed in Table 2.1 to produce sticky ends and subsequently ligated into pET28b(+) for GFP-formin and pGEX-6P2 for mCherry-cofilin. CAP1 was only available as N-terminal and C-terminal fragment and therefore had to be fused in the same way as the fluorescent fusion proteins to obtain the full length CAP1 with the primers shown in Table 2.1. The following cycling conditions were used to amplify DNA fragments via PCR, using 2.5 mM dNTPs, 25 µM of each primer, 0.1-1 µg template DNA and 0.4 Units of Phusion DNA polymerase in Phusion high fidelity buffer (HF buffer, New England Biolabs):

95 °C	2 min	
95 °C	30 s	35x
55 °C	30 s	
72 °C	1 min	
72 °C	5 min	
8 °C	∞	

Amplified DNA inserts were incubated for 1 h at 37 °C with >20 Units of each restriction enzyme purchased form New England Biolabs in their corresponding buffer and the restriction reaction was stopped by inactivating the restriction enzymes for 20 min at 65 °C. The ligation into the corresponding plasmids was achieved by maxing restricted plasmids and inserts with T4 DNA Ligase in T4 DNA Ligase buffer both purchased from New England Biolabs. The molar ratio of plasmid to insert was kept at two to five and the ligation was allowed to incubate for 1 h at room temperature, followed by an incubation at 4 °C overnight. Recombinant *E. coli* strains were produced by transformation. To this extent, the ligated plasmids were combined with chemically competent *E. coli* XL-1 blue cells for DNA production and *E. coli* BL-21 CodonPlus for protein expression, both purchased from Agilent Technologies.

2.2 Protein purification

2.2.1 Actin and ADP-actin

Actin was produced via a method modified by Spudich et al[34]. Lyophilized powder was dialyzed fresh every week by dissolving the powder in Millipore water and subsequently dialyzing the dissolved actin overnight in G-buffer

(2 mM Tris-HCl, 0.2 mM NaATP, 0.2 mM $CaCl_2$, 0.005% NaN_3 and 0.2 mM DTT, pH 8). Initially, the buffer was exchanged every hour three times before overnight dialysis. Then, the actin solution was centrifuged in an ultra-centrifuge at 90000g for 1 h at 4 °C. The supernatant was kept on ice for further use.

For the production of ADP actin, 1 g of lyophilized CnBr activated Sepharose (GE Healthcare) was washed in 1 mM HCl. The resulting slurry was washed for about 15 min in 200 mL of 1 mM HCl in a glass filter, resulting in about 3.5 mL of slurry. About 1500 Units of dry hexokinase (Sigma Aldrich) were dissolved in 5 mL of coupling buffer (0.5 M NaCL, 0.1 M $NaHCO_3$, pH 8.3) and 1 mL of washed slurry was added and incubated on a rotating wheel for 1 h at room temperature. Excess ligand was washed away with 5 times the volume of coupling buffer on a clean disposable column. To block any other reactive groups, the resin was transferred to blocking buffer (0.1 M Tris, pH 8.0) and incubated for 2 h at room temperature. The resin was washed in three cycles alternating with wash buffer A (0.5 M NaCl, 0.1 sodium acetate, pH 6.8) and wash buffer B (0.5 M NaCl, 0.1 M Tris, pH 8.0).

To remove all free nucleotides, a volume of dialyzed G-actin solution was mixed with a half volume of watery Dowex-1 (Sigma Aldrich) slurry. The solution was incubated for 5 min rotating at room temperature, spun down briefly in a table centrifuge and the supernatant was collected. To hydrolyze the remaining actin bound ATP, one tenth volume of hexokinase bead slurry was added as well as 2 mM glucose. The mixture was incubated for 2 h at 4 °C. The slurry was spun down briefly and the supernatant collected to recover the resulting ADP-actin. Hexokinase beads were used for about one month before fresh hexokinase beads were produced. Since ADP-actin is very unstable, it had to be prepared freshly every day.

2.2.2 Profilin

Profilin (mouse profilin 2) was expressed by means of autoinduction[35] of *E. coli* BL-21 CodonPlus cells (Agilent Technologies), which resulted in a higher yield than regular expression protocols. To achieve this, 2x 2 mL LB medium (10 g/L tryptone, 5 g/L yeast extract, 10 g/L NaCl) supplied with 100 µg/mL carbenicillin and 20 µg/mL chloramphenicol were inoculated and precultured for 6 h at 37 °C. The autoinduction medium was mixed by adding 928 ZY medium (12 g/L tryptone, 24 g/L yeast extract) with 1 mL of 1M $MgSO_4$, 20 mL 50x5052 (250 g/L glycerol, 25 g/L D-glucose, 100 g/L α-lactose), 50 mL 20x NPS (0.5 M

$(NH_4)_2SO_4$, 1 M KH_2PO_4, 1 M Na_2HPO_4), 400 µg/mL carbenicillin and 80 µg/mL chloramphenicol. The autoinduction medium was inoculated with the preculture, incubated shaking for 6 h at 37 °C, then for further 60 h at 15 °C. Cells were harvested by centrifugation at least at 5000 xg for 20 min at 4 °C.

The cell pellet was resuspended in 20-30 mL STE buffer (50 mM Tris pH 7.0, 150 mM NaCl, 1 mM EDTA, 1 mM DTT) supplied with 200 µL lysozyme (10 mg/ml), 25 µL Benzonase (Merck) and 1 tablet cOmplete protease inhibitor (Roche). The cells were thoroughly brought into suspension and then disrupted in a French press. Subsequently, the resulting lysate was centrifuged at 17000 rpm in a JA-17 rotor for 30 min and the supernatant was filtrated. 4 mL of Glutathione Sepharose 4B (GE Healthcare) were equilibrated with STE buffer and the equilibrated resin then added to the clear supernatant. To allow the GST-Tag to bind to the glutathione resin, the slurry was incubated for 2 h at 4 °C on a rotating wheel. Afterwards, the slurry was put on a clean disposable column and the supernatant was allowed to flow through. The resin was washed with 20 mL of ice-cold STE in three individual washing steps. A total volume of 1.5 mL of STE was left above the resin and 20 µL of PreScission Protease (GE Healthcare) were added and incubated for at least 2 h at 4 °C. Elution of cleaved protein was carried out in 6 fractions of 1 mL by successively adding STE to the resin. The fractions containing the highest concentrations of profilin were pooled, dialyzed against profilin buffer (20 mM Tris pH 7, 150 mM NaCl, 1 mM EGTA, 1 mM DTT) over night, flash frozen in liquid nitrogen and then stored at -80 °C.

2.2.3 Capping Protein

Capping protein was expressed by growing the bacterial culture containing the plasmid for both protein subunits until it reached an OD_{600} of 0.6 and subsequently adding 0.5 mM IPTG. The induced culture was incubated shaking at 26 °C overnight. The pelleted cells were then disrupted in a buffer containing 20 mM Tris-HCl at pH 8.0, 20 mM imidazole, 250 mM NaCl, 1 mM EDTA, 5% glycerol and 1 mM DTT, centrifuged at 17000 rpm in a JA-17 rotor for 30 min and the supernatant was filtrated. For 100 mL of lysate, a volume of 100 µL Anti-Flag M2 Affinity resin (Sigma Aldrich) was added and incubated 90 min rotating at 4 °C. The beads were washed several times in the same buffer by centrifugation at 14000 rpm in a table centrifuge at 4 °C for 15 min, then taking off the supernatant and adding 1 mL of fresh buffer to the beads. 140 µL Flag

peptide solution (Sigma Aldrich) was added to the beads and incubated at 4 °C for 1h to elute the protein. The beads were sedimented by centrifugation at 14000rpm for 2 min at 4 °C in a table centrifuge and the eluted capping protein dialyzed over night against capping protein buffer (10 mM Tris-HCl at pH 8.0, 50 mM KCl and 1 mM DTT).

2.2.4 Formin (mDia1) and GFP-Formin

Formin was expressed by means of autoinduction as described previously in medium supplemented with the antibiotics kanamycin and chloramphenicol. For a high yield of active protein, all reagents were kept on ice at any time during the purification. When the autoinduction was finished the induced cells were sedimented by centrifugation at 17000 rpm in a JA-17 rotor for 45 min at 4 °C and the supernatant was filtrated. 2 mL of NiNTA functionalized Sepharose resin (cOmplete, Roche) were equilibrated in soni buffer (50 mM Na_2HPO_4, 50 mM $NaH_2PO_4 \cdot 2H_2O$, 300 mM NaCl at pH 8.0) with 20 mM imidazole. The resin was added to the cleared supernatant and incubated rotating on a wheel for 1 h at 4 °C. Then, the resin was added to a clean disposable column and washed with 10 mL soni buffer with 20 mM imidazole, then with 10 mL soni buffer with 50 mM imidazole. Finally, the bound protein was eluted by adding 1.5 mL soni buffer containing 500 mM imidazole. This was repeated six times to collect six fractions of formin. The fraction containing most formin was chosen via SDS-PAGE and added to a NAP-25 gel filtration column (GE Healthcare) equilibrated in PBS at pH 7.4 containing 2 mM DTT.

2.2.5 Cofilin (hCof1) and mCherry-Cofilin

Cofilin was expressed in LB medium containing carbenicillin and chloramphenicol which was further supplied with 2 mM Betaine-HCl. The induction was started by adding 0.5 mM IPTG after an OD_{600} of 0.5 was reached and conducted at 25 °C. Cells were harvested by centrifugation at 4 °C and the cell pellet was resuspended in TBSE (25 mM Tris-HCl at pH 7.4, 300 mM NaCl, 1 mM EDTA and 1 mM DTT) which was further supplied with 50 µg/mL lysozyme, 2,5 µL benzonase (Sigma Aldrich) and 1 tablet of protease inhibitor (cOmplete, Roche). Then, the pellet was disrupted in a French press and the supernatant was cleared by centrifugation at 17000 rpm in a JA-17 rotor for 30 min at 4 °C. 2 mL of glutathione Sepharose 4B (GE Healthcare) were equilibrated in TBSE and subsequently added to the supernatant. To allow the

binding of the GST-tag to the glutathione resin, the slurry was kept rotating for 2 h at 4 °C. The resin was washed multiple times with ice cold TBSE (3x 10 mL), then 20 µL of Precission Protease (GE Healthcare) were added to the slurry and incubated rotating for 2 h at 4 °C. The cleaved cofilin was eluted by opening the column and the resin was further washed by adding 1 mL of ice cold TBSE and collecting 6 fractions in total. The best fractions were chosen via SDS-PAGE and dialyzed overnight against cofilin buffer (10 mM Tris-HCl at pH 7.4, 150 mM NaCl and 2 mM DTT).

2.2.6 CAP1

The expression of CAP1 was realized in LB medium containing kanamycin and chloramphenicol. The culture was grown until it reached an OD_{600} of 0.6 at 37 °C, induced with 0.5 mM IPTG and set to 18 °C to incubate for 16 h. After harvesting the cells, the pellet was dissolved in lysis buffer (25 mM Tris-HCl at pH 8.0, 300 mM NaCl, 1 mM EDTA and 1 mM DTT) supplemented with a protease inhibitor cocktail (cOmplete, Roche). The resuspended cells were disrupted in a French press, cleared by centrifugation and 2 mL of equilibrated NiNTA resin (cOmplete, Roche) were added. The slurry was incubated for 1 h at 4 °C and then put on a clean disposable column. The resin was washed twice with 10 mL wash buffer (25 mM Tris-HCl at pH 8.0, 300 mM NaCl, 1 mM EDTA, 5 mM imidazole and 1 mM DTT). The elution was then achieved by adding 1.5 mL of wash buffer containing 500 mM imidazole. This was repeated six times to collect six fractions. The fractions containing most CAP1 were chosen via SDS-PAGE and then dialyzed overnight against dialysis buffer (25 mM Tris-HCl at pH 8.0, 150 mM NaCl and 1 mM DTT). Then, 25 U per ml of elution of thrombin were added. The mixture was incubated for 2 h at 4 °C on a rotating wheel to allow the cleavage of the His-Tag. After this time, to remove the cleaved His-Tag, 100 µL per mL of elution of equilibrated NiNTA resin were added, and to remove the remaining thrombin, 50 µL per mL of elution of equilibrated para-aminobenzamidine Sepharose (Sigma Aldrich) was added. The slurry was then incubated for 10 min rotating at 4 °C and subsequently passed through a clean disposable column. Finally, the cleaned protein was passed through a NAP-25 gel filtration column (GE Healthcare) equilibrated in dialysis buffer.

2.2.7 VASP

A construct of VASP containing a His-Tag, a GST-Tag and a SNAP-Tag was expressed by growing the corresponding culture to an OD_{600} of 0.6-0.8 at 37 °C. The induction was achieved by adding 1 mM of IPTD and setting the temperature to 21 °C overnight. After harvesting the cells the next day, the pellet was redissolved in PBS at pH 7.5 additionally supplied with 1 mM EGTA, 2 mM DTT, 50 µg/mL lysozyme, 2,5 µL benzonase (Sigma Aldrich) and 1 tablet of protease inhibitor (cOmplete, Roche). After disrupting the cells in a French press, the supernatant was cleared by centrifugation. Then, 2 mL of equilibrated Glutathione Sepharose 4B (GE Healthcare) were added and incubated as a slurry for 1 h at 4 °C while rotating on a wheel. The resin was put back on a clean disposable column and washed twice with 20 mL of ice-cold PBS at pH 7.5 with 1 mM EGTA and 2 mM DTT. Then, 20 µL Precission Protease (GE Healthcare) were added and the reaction was incubated for 2 h at 4 °C while rotating on a wheel. Cleaved VASP was eluted by opening the column. Further VASP was extracted by adding 1 mL fractions of ice-cold buffer six times in total. The fractions containing most VASP were chosen via SDS-PAGE and finally dialyzed against a buffer containing PBS at pH 7.5, 60% sucrose and 2 mM DTT. Due to the high molarity of the dialysis buffer, this decreased the volume inside the dialysis tube drastically, effectively increasing the concentration of the protein. VASP was removed from the dialysis tube carefully and stored at -20 °C. Freezing VASP without sucrose or at -80 °C drastically decreased the fraction of functional protein.

2.2.8 Non-Muscle Myosin II

Myosin was purified utilizing a method adapted from Pollard et al[36,37]. Human platelets from fresh human platelet extract were spun down at 800 g for 10 min at room temperature, washed with PBS by resuspension and spun down again using the same centrifugation conditions. The resulting cell pellet was frozen at -20 °C and defrosted in 2 mL per gram of pellet extraction solution (0.9 M KCl, 15 mM sodium pyrophosphate, 30 mM imidazole, 5 mM $MgCl_2$, and 3 mM DTT at pH 7) by gently stirring the extract with a magnetic stirrer for 30 min on ice. The pellets lysed during thawing. The crude cell extract was clarified by centrifugation at 17000 rpm in a JA-17 rotor for 30 min at 4 °C. Then, 3 volumes of ice cold 2 mM $MgCl_2$ were added to the supernatant while stirring. While still stirring on ice with a magnetic stirrer, the pH was slowly and carefully adjusted to pH 6.4 with 0.5 M acetic acid. The actomyosin was then pelleted by

centrifugation at 17000 rpm in a JA-17 rotor for 30 min at 4 °C. The supernatant was discarded and the pellet was kept, which was crude actomyosin. The pellet was then dissolved in 10 mL of KI-ATP buffer (0.6 M KI, 5 mM ATP, 5 mM DTT, 1 mM $MgCl_2$ and 20 mM imidazole at pH 7) with a Dounce homogenizer. Undissolved material was spun down at 17000 rpm in a JA-17 rotor for 10 min at 4 °C. Then, myosin precipitated from solution by ammonium sulfate fractionation. Ice cold, saturated ammonium sulfate with 0.01 M EDTA was used and ammonium sulfate was always added very slowly while stirring. Each precipitation step was incubated for 10 min stirring. The first fraction was precipitated by increasing the ammonium sulfate concentration from 0 to 1 M ammonium sulfate and was spun down in a JA-17 Rotor at 17 000 rpm for 15 min at 4 °C. The second fraction, which was enriched with myosin, was precipitated by increasing the ammonium sulfate concentration from 1 M to 1.9 M and spun down exactly like the first fraction. Only this precipitate was used for further purification. The precipitate was dissolved in 8 mL of KI-ATP buffer, clarified by centrifugation (30 min in a JA-17 Rotor at 17 000 rpm at 4 °C) and finally applied to a 4% agarose gel filtration column which was well equilibrated it KI-ATP buffer. By size exclusion, myosin was separated from actin and other impurities. All fractions containing pure myosin were combined and precipitated again by adding 66% ammonium sulfate. The precipitate was dissolved again in a small volume of 1.5 mL myosin buffer (0.6 M KCl, 10 mM mono sodium phosphate at pH 7 and 60% sucrose). Myosin was preferably stored at only -20 °C to avoid artifacts by freezing.

2.3 Microscopy

Confocal images of fluorescent samples were taken with a 63× oil immersion objective with a numerical aperture (NA) of 1.4 or, when a lower resolution was sufficient with a 20× oil immersion objective with a NA of 0.7 on a Leica TSC SP5. In all measurements, the pinhole was set to 2. Images with a resolution of 1024 × 1024 pixels were acquired; the scanning speed was set to 100 Hz and the laser power of the used lasers was set to maximal 50%. The imaging was initiated 1 minute after the initiation of the reaction. The images and movies acquired by confocal microscopy were analyzed by using a Fiji distribution. By this means lengths and intensities, such as radial intensity profiles of actin networks on beads were precisely measured. For TIRF microscopy a 100× oil immersion objective with a NA of 1.47 was used on a Leica DMi8 microscope.

Images were captured with a Leica Infinity Scanner. The acquisition frame rate was set to 10 s.

2.4 Bead Assays

An aliquot of cOmplete Ni-NTA resin (Roche) was washed three times with water in a clean disposable column and subsequently stored in water for up to one week at 4 °C. To coat the beads by binding with His-tagged proteins they were carefully mixed with a total amount of 25 nmol of either formin, VCA or an equimolar mixture of both per mL of bedded resin. The proteins were allowed to bind to the resins for 10 minutes and washed afterwards by adding a 100x aliquot of water. The super natant was removed and functionalized beads were stored on ice and used for no longer than one day. Reaction mixtures were pipetted according to the following table in polymerization buffer (10 mM imidazole, 3 mM MgCl2, 0,2 mM CaCl2, pH 7.2):

Concentration	Component
1 mM	DTT
1 mM	ATP
12 µM	Profilin
100 nM	Capping Protein
100 nM / 2 µM / 10 µM	Cofilin
1 µM	CAP1
0.5 µL per 50 µL	Functionalized Beads
5 µM	Actin

Table 2.2: Proteins and other components used in the reconstitution experiments of dynamic actin networks on functionalized agarose spheres.

Only for experiments with beads functionalized with VCA, the polymerization mixture was further supplied with 300 nM Arp2/3. Capping protein is able to debranch F-actin structures polymerized by Arp2/3, therefore the concentration of capping protein was reduced to 10 nM in experiments with Arp2/3 and VCA. The order of which the components were pipetted was of importance, since the polymerization is started with the addition of actin. Therefore, the functionalized beads were added last, only followed by the addition of 5 µM actin.

2.5 Fluorescence Recovery after Photobleaching

Fluorescent samples were photobleached and the fluorescence recovery quantified by using the Leica FRAP Wizard software on a 63× oil immersion objective with a NA of 1.4 on a Leica TSC SP5 microscope. The Zoom In method was used for bleaching and the acquisition speed was set to 400 Hz with 25% laser power for acquisition and 100% laser power for photobleaching. Rectangular regions of interest of different sizes were used to bleach spots directly at the surface of agarose beads. These spots were chosen to avoid the influence of fluctuating filaments in the network. The fluctuation in z-direction specifically can strongly affect the signal and result in a false positive recovery after photobleaching.

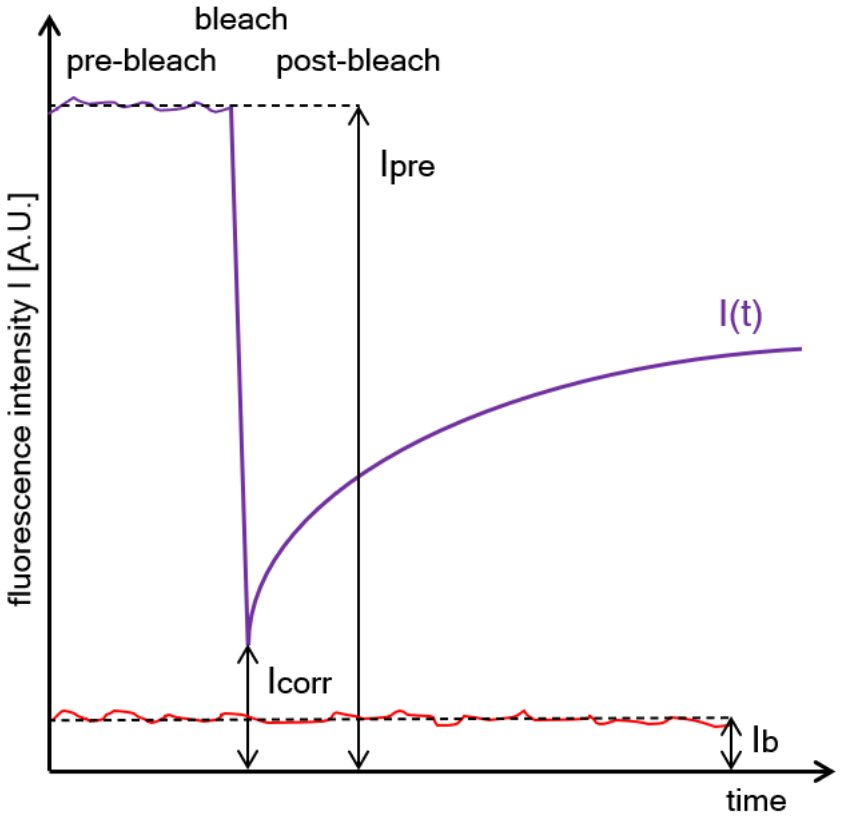

Figure 2.1: Fluorescence recovery curve. The signal of a typical FRAP experiment curve is shown in purple. Important terms used to normalize the data are marked by I(t), the measured intensity signal, I_b, the average background fluorescence, I_{corr}, the minimal signal reached during the bleaching period and I_{pre}, which is the average signal of the pre-bleaching phase.

The acquired data was analyzed by subtracting the background fluorescence as described by the following formula:

$$I(t)_b = I(t) - I_b$$

where I_b is the average fluorescence intensity of the background. The normalization of the signal was done according to the formula

$$I_{b,norm}(t) = \frac{I(t)_b - I_{corr}}{I_{pre} - I_{corr}}$$

By fitting single exponentials to the post-bleach recovery signal, the FRAP half times can be extracted which are used as a measure for the dynamics of the actin network. This was achieved by fitting the data to the following expression:

$$f(t) = a\left(1 - e^{-t/\tau}\right) + c$$

The half time and recovery rates were then calculated by using the formula

$$t_{1/2} = \tau \cdot ln2$$

2.6 Microscale Thermophoresis

Microscale thermophoresis (MST) is a method which quantifies the affinities of a fluorescently labeled target towards a binding partner. Specifically, in this thesis the binding of actin binding proteins towards fluorescently labeled actin is measured. The underlying physical principle is the directed motion of molecules along temperature gradients, which is strongly affected by the hydration shell of proteins and thus differs for bound and unbound ligands[38]. The local depletion of the fluorescent target by inducing a temperature gradient can be measured while varying the concentration of its binding partner. This results in binding curves which can be fitted with the expression

$$\Delta I(x) = I_{unbound} + \frac{I_{bound} - I_{unbound}}{2(c_{fluo} + x + K_D - \sqrt{(c_{fluo} + x + K_D)^2 - 4 \cdot c_{fluo} \cdot x})}$$

where ΔI is the difference between the depleted and initial fluorescence signal at the ligand concentration x, I the fluorescence intensities in A.U. in the bound or unbound state respectively, c_{fluo} the constant concentration of the fluorophore target and K_D the dissociation constant, resulting in a sigmoidal curve.

Samples were pipetted in PCR tubes. In each tube a 10 µL aliquot of fluorescently labeled actin monomers or ADP-actin monomers was pipetted. Subsequently, a dilution series was made, starting with an equal volume of the highest concentration of ligand available. Different concentrations were made

by mixing the 10 µL aliquots with 10 µL from the previous tube to decrease the concentration by half with each time mixing. The final concentration of fluorescent actin was kept constant at 100 nM in each tube.

The binding reaction was allowed to incubate for 5 minutes on ice. Then, capillaries were filled, one per concentration. The fluorescence of capillaries was measured in a NanoTemper Monolith device. A capillary scan was performed before each measurement to make sure that each sample had roughly the same amount of fluorescence counts. Only 10% difference from the average peak fluorescent count was tolerated or the concentration was discarded.

2.7 Nucleotide exchange assays

The nucleotide exchange assay is performed on previously prepared ADP-actin and reflects the spontaneous or cofactor assisted exchange of ADP with fresh ATP. Similar to pyrene assays which monitor the polymerization of actin by the increase fluorescence of the pyrene molecule in the F-actin state, the nucleotide exchange assay takes advantage of the enhanced fluorescence of ε-ATP (1-N6-ethenoadenosine 5'-triphosphate) when bound to G-actin. The fluorescence thus increases proportionally with the amount of ε-ATP bound to actin monomers[39].

In black quartz cuvettes suitable for fluorescence, a solution of 2 µM ADP-actin was prepared in G-buffer. Optionally actin binding proteins were added when stated accordingly. A final concentration of 50 µM ε-ATP was added to start the exchange reaction. The reaction was monitored in 10 s intervals for 1500 s with a 350 nm excitation wavelength and a 410 nm emission wavelength in a Jasco FP 8500 spectrofluorometer. The linear part of the recorded exchange kinetics was used to fit a line and the slopes were used to calculate exchange rates. Nucleotide exchange rates were then normalized to the exchange rate of only ADP-actin.

2.8 Production of Supported Lipid Bilayers

The following cleaning and edging protocol was used to prepare coverslips for the production of supported lipid bilayers: First, coverslips were sonicated for 20 min in a solution of 20% Hellmanex, followed by sonication for 30 min in 2 M potassium hydroxide. After the sonication steps the coverslips were washed

thoroughly with Millipore water, followed by a final wash step with ethanol. Edged coverslips were stored in ethanol for multiple weeks. Right before use, a coverslip was taken out, dried in a flow of nitrogen and cleaned in a UVO cleaner for 5 min.

To produce a supported lipid bilayer, small unilamellar vesicles (SUVs) had to be formed first. Here, an extrusion method was used to generate SUVs. Lipid mixed for SUVs were produced by the following recipe with a total concentration of 20 mM in chloroform:

Concentration	Component
97.4%	Egg-PC (L-α-phosphatidylcholine from chicken egg)
2.5%	Ni-NTA lipids (1,2-dioleoyl-sn-glycero-3-[(N-(5-amino-1-carboxypentyl)iminodiacetic acid)succinyl] (nickel salt))
0.1%	Texas Red™ 1,2-dihexadecanoyl-sn-glycero-3-phosphoethanolamine triethylammonium salt

Table 2.3: Composition of lipid mixes used for the production of SUVs. Lipid mixes were prepared in chloroform at a total concentration of 20 mM and stored at -20 °C in brown glass vials to protect lipids from oxidation and photobleaching. After taking vials out of the freezer they were allowed to reach room temperature before opening them to avoid the contamination of chloroform by water condensation.

A volume of 50 µL mixed lipids in chloroform was dried in a glass vessel under nitrogen flow until the lipid film looked dry. To remove any traces of chloroform, the lipid film was subsequently dried for 2 h in a vacuum chamber. Then, 1 mL of PBS (137 mM NaCl, 2.7 mM KCl, 10 mM Na_2HPO_4 and 1.8 mM KH_2PO_4 at pH 7.4 was added and vortexed for at least one minute until the lipids were homogenized. To homogenize the lipids further, the glass vessel was sonicated for 30 mins. Then, a syringe was filled with the lipid emulsion and passed ten times through a polycarbonate membrane stabilized with filter supports in a commercially available extruder from Avanti Polar Lipids. To increase the purity of the formed SUVs, the emulsion was centrifuged for 20 min at 30000 g in an ultracentrifuge and stored in the cold room at 4 °C for up to two weeks.

A flow chamber was built by sticking two parallel strips of parafilm on an edged coverslip and closed with a smaller quadratic coverslip. The parafilm was softened by heating the chamber on a heating plate to 60 °C for 30 seconds which closed the edges of the chamber tightly. Then, the chamber was filled

with an SUV solution which was previously diluted to 20% in PBS. The bilayer formed by SUVs bursting on the edged glass for 5 min, then the chamber was flushed extensively with PBS. At least 1-2 mL of PBS were flushed through the flow chamber in multiple steps to remove any remaining SUVs.

2.9 Electroswelling of Giant Unilamellar Vesicles

Electro-formation of vesicles was performed on glass slides coated with a conducting layer of indium tin oxide (ITO). These cover slides had to be prepared by cutting slides from ITO glass and gluing those thin, coated slides on more durable microscopy slides. ITO cover slides prepared in this way were generally washed first with mineral oil, then soap and hot water and finally with chloroform to remove all remaining traces of oil. Ethanol and Hellmanex were avoided as cleaning agents to not disturb the ITO layer.

A lipid mix was prepared in chloroform with a total concentration of 20 mM. Phase separated vesicles were generated by mixing two lipids with a relatively high or low melting temperature T_M respectively and cholesterol leading to non-mixing, coexisting liquids[40,41]. DOPC was chosen as low melting temperature lipid, while DPPC was chosen as high melting temperature lipid at a concentration of 20% cholesterol for stable phase separation at room temperature. The full list of lipids used in the lipid mix is presented in Table 2.4.

Concentration	Component
38.7%	DOPC (1,2-dioleoyl-sn-glycero-3-phosphocholine)
38.7%	DPPC (1,2-dipalmitoyl-sn-glycero-3-phosphocholine)
20%	Cholesterol
2.5%	Ni-NTA lipids (1,2-dioleoyl-sn-glycero-3-[(N-(5-amino-1-carboxypentyl)iminodiacetic acid)succinyl] (nickel salt))
0.1%	Texas Red™ 1,2-dihexadecanoyl-sn-glycero-3-phosphoethanolamine triethylammonium salt

Table 2.4: Composition of lipid mixes used for the production of phase-separated GUVs by electroswelling. Lipid mixes were prepared in chloroform at a total concentration of 20 mM and stored at -20 °C in brown glass vials to protect lipids from oxidation and photobleaching. After taking vials out of the freezer they were allowed to reach room temperature before opening them to avoid the contamination of chloroform by water condensation.

A Hamilton syringe was then cleaned three times with chloroform and loaded with a volume of 15 µL of the lipid mix. The lipid mix was then applied on two ITO-covered slides by carefully and evenly spreading the mix on about two thirds of the conducting side of the slides while leaving about 2 mm blank at the edges. To remove all chloroform the slides were dried at room temperature for 10 min and subsequently transferred to a desiccator. They desiccator was evacuated with a vacuum pump and the slides stored in the vacuum for multiple hours or overnight to remove all traces of chloroform.

Chambers for the production of giant unilamellar vesicles (GUVs) were then produced by covering the rims of about two thirds of the ITO slides with a thin line of vacuum grease and adding two strips of Teflon spacers with a thickness of 1 mm to the edges of one slide. The slides were connected to a function generator via two electrodes that were stuck to the end of the cover slides that was not lined with vacuum grease using a small piece of duct tape, one per slide. The chamber was then closed by sticking the two slides together and subsequently filled with the desired aqueous solution. Solutions contained only sucrose for empty vesicles or the desired proteins for treadmilling actin networks described previously in polymerization buffer. Buffers with higher amounts of salt were not feasible as the resulting current would heat up the chambers.

A solution of 2M sucrose was added to the solutions to the point where an osmolarity of 700-900 mOsm was reached as determined by an osmometer. The total volume of the swelling solution was 300 µL. Then the swelling was started by setting the function generator to a frequency of 500 Hz and varying the amplitude starting with 0.1 V for 5 min, followed by 0.9 V for 20 min and finally 2.6 V for 90 min. When the electroswelling was completed, the chamber was disconnected from the function generator and the sucrose solution containing the vesicles was washed multiple times by sedimentation of the vesicles in an equally osmotic glucose solution of at least 2 mL volume. Vesicles sedimented slowly in the glucose solution due to the lower molecular weight of glucose as compared to sucrose. The sedimented vesicles at the bottom of the tube were collected and added to another tube containing fresh glucose or used directly by diluting them at least 1:100 in a closed, vacuum grease chamber on a microscopy slide.

2.10 Active Actin Cortex Arrays

To mimic a cellular cortex, a supported lipid bilayer was produced as described previously and used as a model cell membrane. VASP was expressed with a His-Tag which was able to bind to the fraction of NiNTA functionalized lipids. In a first step, VASP was diluted with PBS to 3 µM and flushed in the prepared flow chamber containing a supported lipid bilayer. After 5 minutes, free VASP which did not bind to the membrane was removed by flushing with PBS. Then, a polymerization mixture was prepared in KMEI (10 mM imidazole pH 7.0, 1 mM $MgCl_2$, 1 mM EGTA, and 50 mM KCl) buffer by using the following recipe in Table 2.5.

Concentration	Component
1 mM	DTT
1 mM	ATP
0.4% / 0.8%	Methylcellulose
10 U/mL	Glucose oxidase
1 kU/mL	Catalase
0.66 % (w/v)	Glucose
10 mM	Creatine phosphate
20 U/mL	Creatine phosphokinase
0 mM / 200 mM	Non-Muscle-Myosin II (NMMII)
500 mM	Actin

Table 2.5: Components used in the reconstitution of model cell cortices on SLBs. 0.4% methylcellulose was sufficient for most experiments, only for controls without VASP bound to the SLB the concentration had to be increased to 0.8% or no bundles could be formed on the model membrane. Glucose oxidase, catalase and glucose form a scavenger system which was able to neutralize radicals that form during the illumination and would otherwise be damaging to the samples. Creatine phosphate, creatine phosphokinase and ATP are used as an ATP regeneration system to keep the concentration of ATP constant during they experiment.

3. Depletion Effects as a Consequence of Global Actin Turnover

In vitro reconstitution assays of actin dynamics has been achieved on the level of single filament actin turnover[42]. In these systems, phenomena like stochastic cofilin severing[43], funneling of monomers[10] and formation of cofilin resistant filaments by inducing an antagonistic twist[44] can be observed. Although all of those insights contribute to our understanding of single filament dynamics, reconstituted systems have to advance towards the projection of the dynamics of whole actin networks. Recent studies suggest a model of a coordinated, global actin turnover in living cells, in which branched, linear bundled or unbundled and contractile actin geometries coexist, while being maintained and organized by a common monomer pool (Figure 3.1)[11]. Specifically, the organization of actin at the lamellipodium, where branched and linear actin structures are present to drive the protrusion of the membrane at the leading edge are hereby dominated by the effects of global actin turnover. Depolymerization and recycling of monomers are key to keep up a continuous polymerization of filaments and thus maintain the force generation at the membranes.

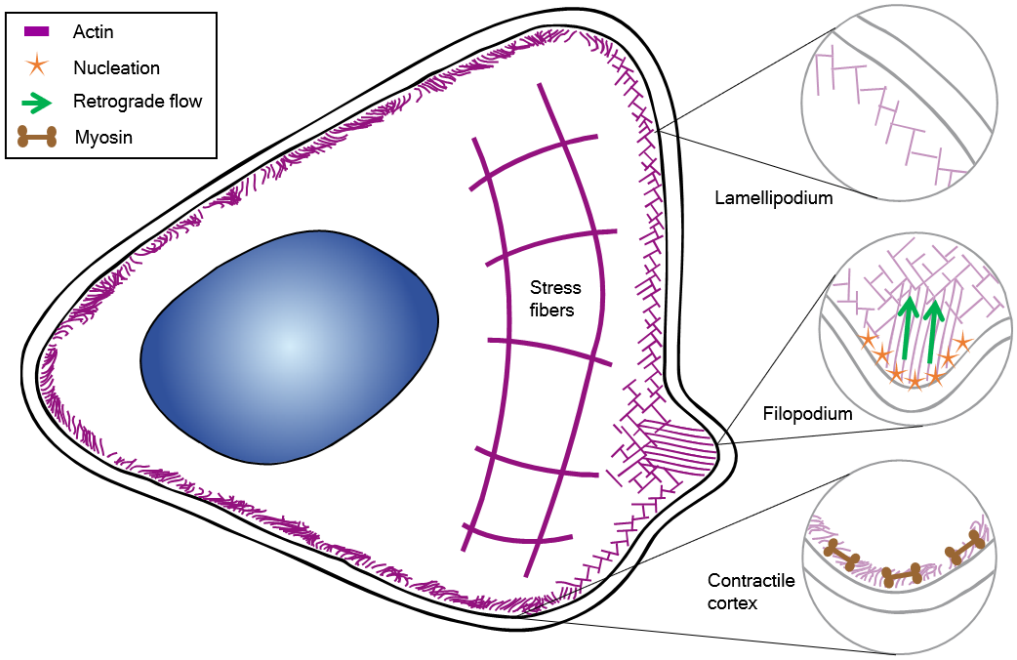

Figure 3.1: Actin organization in motile cells. Different architectures of actin networks coexist and share a common monomer pool. Antiparallel, contractile stress fibers and the contractile cortex exert forces to retract the cell by associating with the motor protein myosin. The lamellipodium is composed of branched actin networks, while filopodia are finger-like protrusions that are produced by parallel actin bundles. Filopodia are

elongated by a constant polymerization at the membrane, while simultaneously being retracted by cytosolic myosin. This leads to a retrograde flow of actin filaments, a flow in the opposite direction of the filopodium growth. Simultaneously, actin is constantly disassembled in the filopodia. Disassembly and recycling of monomers maintains the pool of available monomers.

To reconstruct a novel, biomimetic system of global actin turnover that goes beyond the description of single filament dynamics, multiple factors that are also met in living cells as described previously have to be considered.

1) The nucleation of the system has to be controlled. In cells, nucleation seeds are often capped by capping proteins and monomers bound by profilin, which prevents the spontaneous association to filaments.
2) The localization of actin filaments needs to be limited towards specific sites. Bulk polymerization is not able to exert forces specifically towards surfaces. *In vivo*, this is achieved by nucleating proteins that are located close to the membranes of filopodia and lamellipodia.
3) Disassembly of actin filaments must be ensured. By enhancing the pointed end depolymerization, a faster overall turnover can be achieved. In closed systems fresh monomers cannot be supplied and have to be disassembled from the network itself.
4) Monomers that have been recovered by pointed end depolymerization have to be recycled. Pointed end monomers are likely in the ADP state and need to be replenished with fresh ATP to be able to be used again for polymerization.

Here, experimental conditions are identified in which such a biomimetic system can be implemented by coupling the elongator protein formin towards the functionalized surface of agarose microspheres. The networks polymerized in this system meet all the conditions set by the example of living cells and are used to study the dynamics of global actin turnover in vitro. It is shown experimentally that these networks are highly dynamic and display properties that can only be observed in dense, treadmilling networks. A striking consequence of the turnover dynamics at the surface is the propulsion and spinning of agarose microspheres as a consequence of force generated by actin elongation at the surface. This is an example how actin turnover even without motor proteins is able to produce force, potentially to initiate and elongate protrusions on biological membranes. Surprisingly, globally treadmilling networks are strongly controlled by local depletion effects. The depletion of monomers has been previously described to dominate micropatterned,

branched actin networks aswell[45]. This study extends this model to also include the depletion of actin binding proteins by associating with the treadmilling network. Ultimately, it is shown how this system can be coupled to the surface of GUV's moving the field of actin reconstitution significantly closer to the production of self-organizing artificial cells.

3.1 Reconstitution of global treadmilling in dynamic actin networks

To fulfill the required properties of a global treadmilling system, the actin elongator formin is expressed with a 6xHis-Tag. By using surfaces with immobilized nickel cations, most commonly NiNTA, it is possible to bind His-tagged proteins due to electrostatic interactions between the cation and the partial charges of the amino acid histidine. Polymerization solutions of actin are supplied with polymerization buffer (10 mM imidazole, 3 mM MgCl2, 0,2 mM CaCl2, 1 mM DTT, 1 mM ATP, pH 7.2), 12 µM profilin and 100 nM capping protein to suppress the background polymerization and funnel monomers towards the surface bound formin. This polymerization reaction is first tested without functionalized microspheres in a pyrene assay. Here, a typical polymerization curve can be observed for actin only, but in the presence of 12 µM profilin the polymerization is slower. In the presence of profilin and capping protein, no polymerization can be observed, meaning that all monomers and actin seeds are profilin bound or capped respectively, thus preventing all oligomerization. The addition of 1 µM formin allows for a rapid, formin catalyzed elongation even in the presence of profilin and formin (Figure 3.2, left).

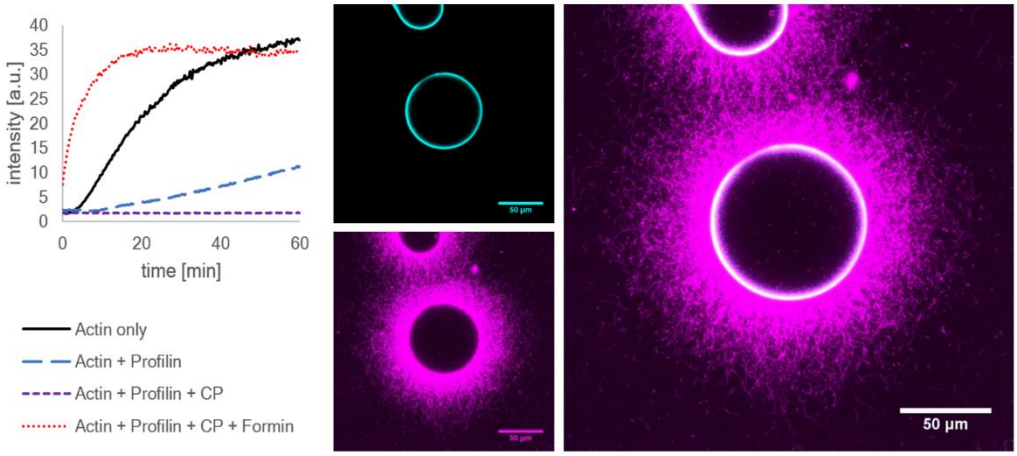

Figure 3.2: The functionality of profilin, capping protein and formin and labelling of filaments by using fluorescently labeled phalloidin. On the left, a pyrene assay is shown which displays the polymerization kinetics of an actin network in the presence of 3 µM

actin only, actin and 12 µM profilin, or additionally 120 nM capping protein or additionally 1 µM formin. Profilin slows down the polymerization speed, while profilin in combination with capping protein completely prevent the nucleation and polymerization of actin. Formin leads to a high polymerization speed even in the presence of profilin and capping protein. On the right a microsphere functionalized with a His-tagged mCherry-formin (cyan) construct is shown. The background solution is spiked with the same proteins used in the pyrene assay. Thus, the background polymerization of actin (purple) is completely suppressed and actin elongation can only occur from the surface.

By using Alexa Fluor 647 conjugated phalloidin (Thermo Fisher Scientific), the polymerization of filaments can be visualized by means of confocal microscopy. Phalloidin bind filamentous actin but does not bind to monomers. Here, phalloidin is shown in magenta and the fluorescence of a GFP-formin construct is shown in cyan (Figure 3.2, right). Since phalloidin binds exclusively to filaments, it can be observed that filaments are only polymerized from the surface. Additionally, formin is only located at the surface. Due to the affinity of formin to the barbed ends of filaments, the assumption that all filaments are oriented with their barbed ends towards the surface is plausible.

This system meets the first and second prerequisite for global actin treadmilling, the control of actin polymerization as well as the localization of nucleation towards specific, functionalized sites. However, in the presence of phalloidin filaments are stabilized and depolymerization is completely suppressed. Therefore, actin treadmilling cannot be reconstituted in such a manner. Covalently labeled monomers have to be used to visualized actin and cofilin as they do not interfere with pointed end depolymerization. Additionally, cofilin is used to increase the overall dynamics and facilitate the disassembly of the network.

3.2 Growth depletion in treadmilling networks

Initially, the turnover kinetics of a system without disassembly by cofilin and monomer recovery is examined. In Figure 3.3, the elongation kinetics of a single filament is shown next to the elongation of a whole network. The slope is the elongation speed v, which depends on the formin dependent rate constant k, the length of an individual monomer δ which is estimated to be 3 nm and the monomer concentration G. In both cases the monomer concentration is 5 µM, however in the single filament case individual filaments are polymerized from formin bound to a glass surface by using an antibody against formin and

visualized via TIRF microscopy. The network case is prepared by functionalizing a microsphere as described previously.

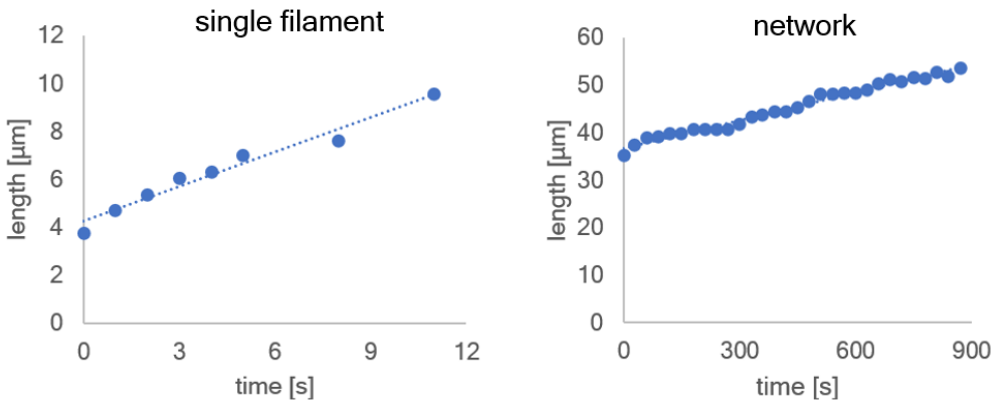

Figure 3.3: Elongation speed of TIRF single filaments and network elongation speed on functionalized microspheres. Single filaments are polymerized by immobilizing a formin antibody (Anti-DIAPH1, abcam) diluted 1:1000 on a cleaned microscope slide. After incubation with formin, a protein mix equivalent to the mix used for bead measurements is added to the functionalized microscope slide. Here, the polymerization of filaments is monitored by means of TIRF microscopy. For bead networks, the network width is measured after an initial polymerization of 10 minutes. Assuming the filaments elongate normal to the bead, the network width can be used to account for the growth rate of individual filaments. For a single filament, the rate k_0 is close to 10 $\mu M^{-1}s^{-1}$ and the elongation speed 0.2 µm/s, ten times faster than the elongation speed on a bead, which is 0.02 µm/s.

The elongation speed for a single filament is 0.2 µm/s and remains constant for an observed time of 30 minutes, while the elongation speed for a network is initially equally fast and only reaches a plateau value after 10 minutes of initial polymerization, which is than 0.02 µm/s, ten times slower than the individual filaments. As the only difference between the two scenarios is the density of the nucleator, this slowdown can be explained by the local depletion of monomers at the elongation site. Due to the linear dependence of the elongation speed towards the monomer concentration, it can be assumed that the local concentration is only a tenth of the initial, global actin concentration of 5 µM.

To compensate for the slowdown of the elongation kinetics in diffusion limited actin networks, monomer recycling is now introduced. This is achieved by adding the protein cofilin which facilitates pointed end disassembly and promotes filament severing, albeit the former effect is strongly enhanced by the presence of CAP1. CAP1 also facilitates the nucleotide exchange of cofilin bound ADP-actin monomers, thus recycling monomers for polymerization (Figure 3.4, left).

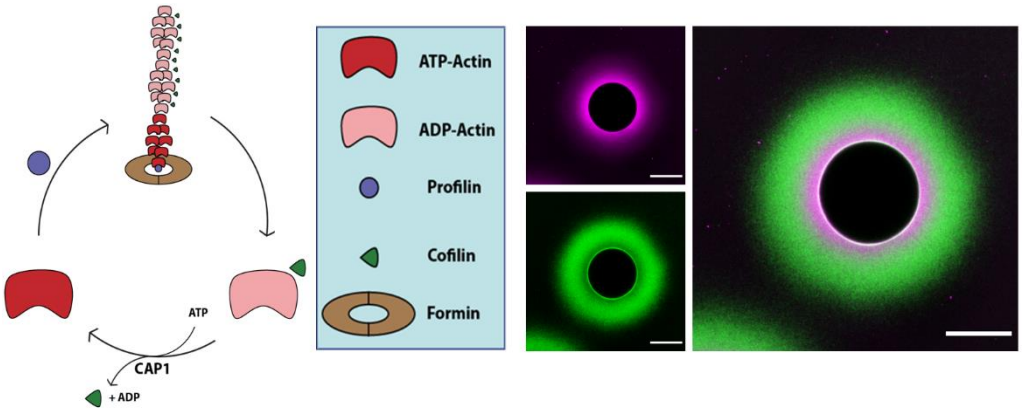

Figure 3.4: Reconstitution of actin turnover on microspheres. On the left, a graphical representation of the experimental setup is shown. Formin processively elongates actin barbed ends by recruitment of profilin bound ATP-actin-monomers. Due to the higher ATP hydrolyzation rates of ATP in F-actin, monomers are rapidly transferred into their ADP-state and are then bound by cofilin due to the high affinity of cofilin towards ADP-actin-monomers. Cofilin then promotes the sequestering of the filament enhanced by CAP1, which also catalyzes the nucleotide exchange. Thus, monomers are supplied with ATP, bind profilin and are able to be recycled. The resulting network is shown on the right. Here, actin is shown in magenta and cofilin in green. Due to the upkeeping of the turnover, an area close to the surface of the microsphere remains undecorated by cofilin. The part of the filament which is closer to the pointed ends is highly decorated by cofilin, resulting in a diffusive cloud of cofilin around the network which likely consists of severed, decorated actin fragments, cofilin bound monomers and dissociated cofilin.

In confocal microscopy images, cofilin appears as a diffusive cloud around the constantly growing network (Figure 3.4, right. Cofilin is shown in green, actin is shown in magenta). This can be explained by the fact that pointed end depolymerization creates cofilin bound monomers in equilibrium with free cofilin which is detached by the activity of CAP1. Cofilin bound monomers and free cofilin are highly diffusive, however are enriched in an area around the bead where the pointed ends of the network are supposedly located. The high concentration of cofilin in this area is due to the constant binding to the pointed ends and unbinding due to depolymerization followed by nucleotide exchange. However, cofilin is only sparsely close to the surface of the bead, as this is where the barbed ends are located. The barbed ends are constantly supplied with fresh ATP-actin monomers. Due to the preference of cofilin towards ADP-actin binding, a zone close to the surface is created where cofilin is excluded.

3.3 Network composition is coupled to the cofilin concentration

To demonstrate the effect of the cofilin concentration on the networks, the cofilin concentration is varied. Concentrations of 100 nM, 2 µM and 10 µM are chosen to cover a wide concentration regime. At 100 nM cofilin the network is hardly decorated by cofilin, only pointed ends seem to be bound by cofilin. At 2 µM the length of decorated and undecorated actin is roughly equal and at 10 µM all actin appears to be in the cofilin-decorated state. The plot Figure 3.5 at the bottom right shows that the absolute widths of the actin networks does not change significantly. Remarkably, in the intermediate regime (2 µM cofilin) the plateau width of the network is reached about 10 min faster than in the other two regimes (Figure 3.5, top right). Hence, the time necessary for the network to reach its plateau increases when more than 2 µM cofilin is present. This slowdown seems to be in contrast with the severing activity of cofilin that should increase the number of filaments ends and therefore increase the net polymerization rate[9]. However, since here filament elongation occurs only from the bead surface, barbed ends created by severing do not contribute to the net polymerization rate. Consequently, the growth rate of the network width should only depend on the balance of the elongation rate at the surface and the depolymerization rate at the pointed ends.

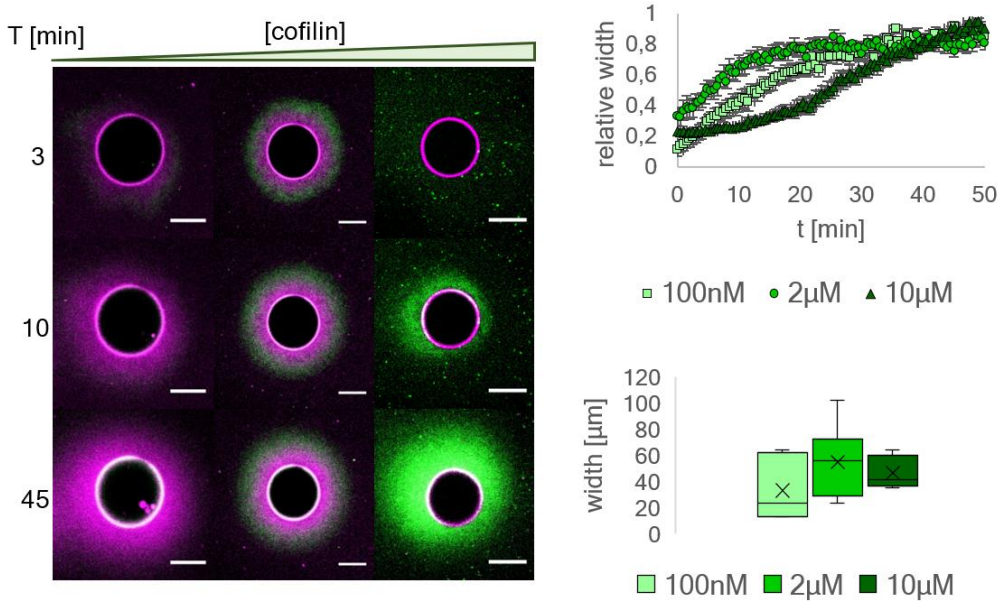

Figure 3.5: By varying the cofilin concentration networks can be divided into three regimes. Network polymerization in the presence of 100 nM cofilin (left column), 2 µM cofilin (middle column) and 10 µM cofilin (right column), actin is shown in magenta, cofilin is shown in green. At 100 nM cofilin (left column), the network consists mostly of cofilin undecorated actin. At 2 µM (middle column), the cofilin decorated and

undecorated regions of the networks are balanced and at 10 µM cofilin (right column) the network is mostly decorated. In the top right plot, the growth kinetics of all networks are affected by the cofilin concentration. Here, the network width is plotted against time. At 2 µM cofilin networks reach their plateau width in the shortest time. This can be explained by the increased net turnover compared to the 100 nM cofilin network. At 10 µM cofilin, the net growth rate of the cortex is slowed down by the excess of cofilin and the resulting enhancement of disassembly rates. In the bottom right plot, the statistical analysis of network widths is shown. The absolute values of plateau widths (n=6) vary at all concentrations and don't depend on the cofilin concentration. This can be explained by the fact that labeled monomers are employed to determine the network width. Labeled monomers don't allow to distinguish between actin filaments and severed actin fragments. Thus, the determined values don't take into account what fraction of the network has been severed.

The radial intensity profiles of actin and cofilin demonstrate the development of the network width and composition over time (Figure 3.6a). The actin intensity profiles (magenta) are measured by means of covalently labeled monomers and therefore represent the local density of the network. All networks are densest at the surface and, as a consequence of the spherical bead geometry, less dense with increasing distance. The most notable difference between the initial and equilibrated state can be observed at 10 µM cofilin. In accordance to our previous observations, there is almost no actin polymerized in the initial state and the net elongation is slowed down by the excess of cofilin. After equilibration however, the actin profiles in all regimes display the same trend in relative intensity, width and slope.

The cofilin profile (green) is relatively low and flat in the 100 nM regime, indicating that most actin in the network is undecorated. At 2 µM cofilin, the cofilin profile has a peak at 12 µm from the bead surface that grows wider during equilibration while the position of the maximum does not change. At 10 µM cofilin a similar peak is visible even closer to the bead, which exhibits a similar broadening, however in this regime the apex migrates away from the surface over time. The broadening of the profiles can be explained by the activity of cofilin. By severing and disassembly of fragments, cofilin creates a fraction of elements that are diffusive, unlike the network. Until the severed, cofilin-decorated actin fragments are completely disassembled, they can diffuse freely and therefore contribute to cofilin peak broadening over the course of the experiment.

The ratio of cofilin to actin intensities (Figure 3.6b) can be used as relative measure to estimate the fraction of decorated to undecorated actin, and which can be assumed to be proportional to the severing and disassembling activity of

cofilin. Since this ratio is not constant throughout the network, it is possible to pinpoint areas where depolymerization and hence recycling of monomers is highest. At 100 nM cofilin, the ratio is lowest close to the bead and increases until a plateau is reached at 40 µm distance. In contrast, at 2 µM and 10 µM cofilin the profiles are in the vicinity of the surface and decrease from there. Now, maxima are fitted to the decoration profiles of multiple beads for 2 µM and 10 µM cofilin (Figure 3.7) to find that over time all regimes have a tendency towards a decoration maximum at a distinct distance, depending on the cofilin concentration: 15 µm at 2 µM cofilin and 10 µm at 10 µM cofilin. For 100 nM cofilin no clear boundary within the network was detectable and 40 µm was determined to be the total width of the actin network.

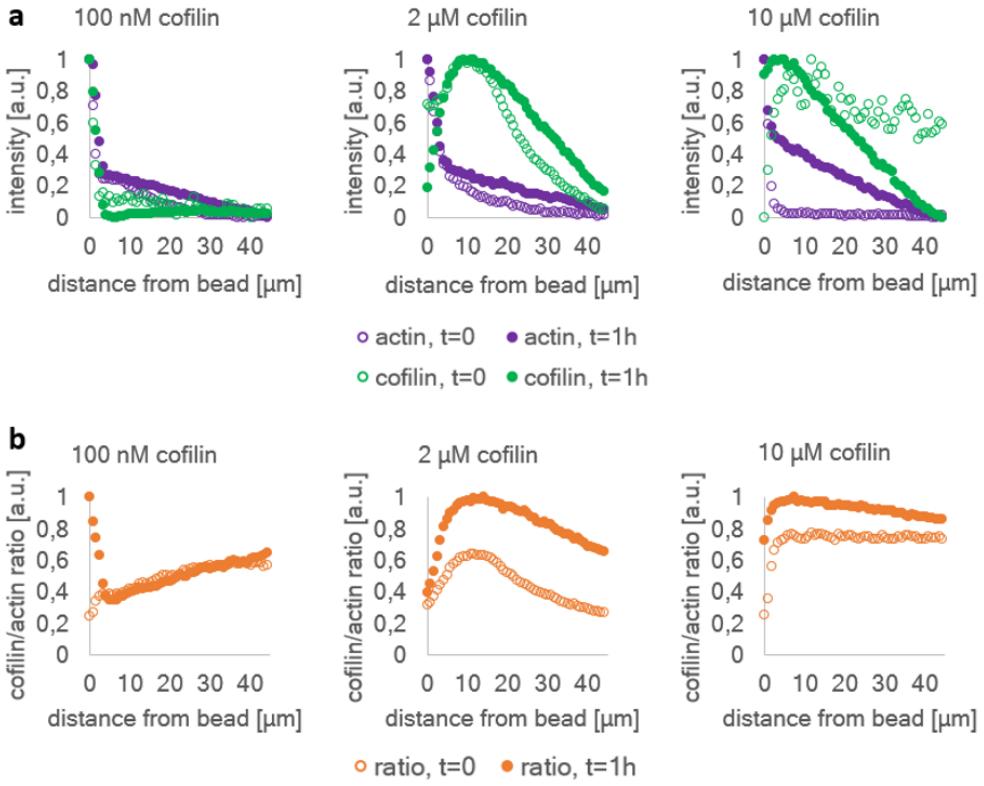

Figure 3.6: Radial intensity profiles of actin networks polymerized on agarose beads in the presence of different cofilin concentrations. **a** Actin intensity profiles (magenta) display a similar trend in shape and width at all cofilin concentration. The cofilin intensity profiles (green) depend however strongly on the used cofilin concentration. At 100 nM cofilin, the cofilin profile is low and flat throughout the cortex, however, after 1 h of polymerization an increase towards the outside solution where the pointed ends are located can be observed. This indicates that most of the actin in this network is not decorated with the exception of the pointed ends at around 40 µm from the bead surface where the network ends. At 2 µM and 10 µM cofilin a maximum in the cofilin intensity profile is visible. **b** Comparison of the cofilin to actin intensity ratios. These ratios reflect the fraction of cofilin decorated actin of the network, thus identifying regions in the network that are most affected by the effects of cofilin. At 2 µM and 10 µM cofilin a decoration maximum is visible at a distinct distance of 15 µm from the surface for 2 µM cofilin and 10 µm from the surface for 10 µM cofilin. At 100 nM cofilin no maximum can be fitted to the ratios, but the profiles display a trend to reach a plateau at around 40 µm where the networks end

At all cofilin concentrations an equilibrium is reached after 20 min (2 µM cofilin), 30 min (100 nM cofilin) and 50 minutes (10 µM cofilin) where neither the length of the network, nor the ratio between width of cofilin-decorated actin and actin changes. This suggests that a steady state of collectively treadmilling filaments is reached.

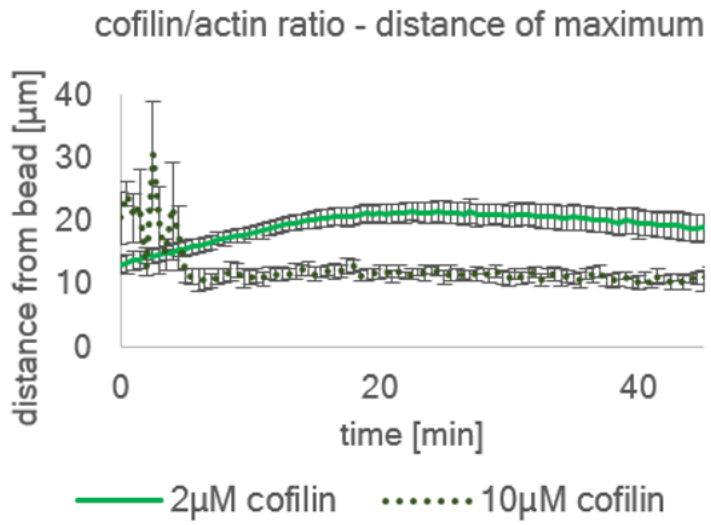

Figure 3.7: Tracking the decoration maximum as an indicator for local cofilin activity. Fitting maxima to the cofilin/actin ratios for multiple beads (n>3) visualizes the distance towards the bead surface of the maximum over time.

3.4 Networks are highly dynamic at intermediate cofilin concentrations

To quantify the internal dynamics monomers with a different fluorescent label are added to functionalized pre-polymerized as shown previously (Figure 3.8a, pre-polymerized label is shown in magenta, secondary label in cyan). The intensity profiles demonstrate how the secondary color is incorporated from the surface outwards (Figure 3.8b). Due to the dynamics introduced by the presence of cofilin, the incorporation of the second label is much faster when cofilin is at an intermediate concentration of 2 µM or higher, at 10 µM (Figure 3.8c).

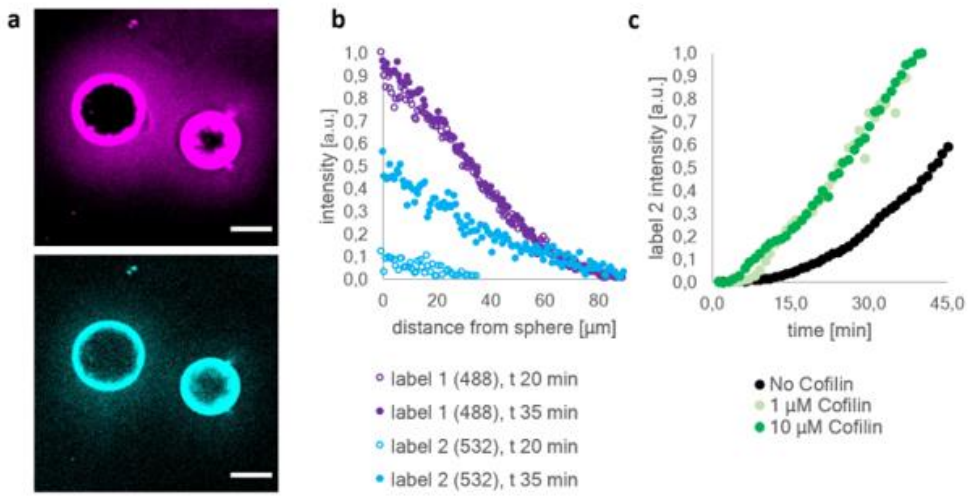

Figure 3.8: Introduction of monomers labeled with a different fluorescent color to networks polymerized on formin functionalized agarose beads. Formin functionalized agarose spheres were incubated in a polymerization mixture containing 12 µM profilin, 100 nM capping protein and 5 µM actin with 10% monomers fluorescently labeled with an Atto 488 NHS-ester. After 30 minutes of initial incubation, an additional amount of 500 nM of monomers labeled with an Atto 532 NHS-ester were added. **a** Incorporation of the second label (cyan, bottom) occurs from the bead surface. The initially polymerized network containing the first label (magenta, top) remains mostly unchanged. No unlabeled areas appear in the initially polymerized network where the 532-monomers are incorporated, indicating that monomers with both labels are still available and built into the network together. **b** Intensity profiles of the networks for both monomer types, at 20 minutes and 35 minutes after addition of the 532-monomers. At 20 minutes the incorporation of the second monomers into the network can be observed. The lag time of 20 minutes can be explained with the slow diffusion of the monomers through the optical chamber, as mixing would disturb the initially polymerized networks. 35 minutes after addition of the second monomers, more monomers have been built into the network. The growth occurs specifically from the surface towards the outside solution, revealing that the filaments are indeed most likely oriented with the barbed ends bound at the bead surface and the pointed ends extend towards the outside solution. The intensity values have been normalized by their respective maximal value at the bead surface. Here, formins get saturated with actin and therefore have an intensity value that depends only on the density of formins. Additionally, the background intensity of the monomers has been subtracted. **c** The kinetics of the incorporation of the second monomers is faster in the presence of cofilin and 1 µM CAP1. For both cofilin concentrations, 1 µM and 10 µM, the incorporation of the second monomer is faster, although no difference in incorporation speed can be observed between 1 µM and 10 µM cofilin. This is in agreement with further analysis of the internal dynamics of this system. An offset time accounting for the lag time due to diffusion of the additional monomers has been subtracted and the intensity values have been normalized as described previously.

This is further quantified by means of FRAP measurements. To this end a region directly at the bead surface is bleached. A kymograph shows the region of interest's initial fluorescence, the bleaching phase indicated by orange lines and the fluorescence recovery (Figure 3.9, left). For each region of interest, the recovery is also represented by the intensities over time (Figure 3.9, right).

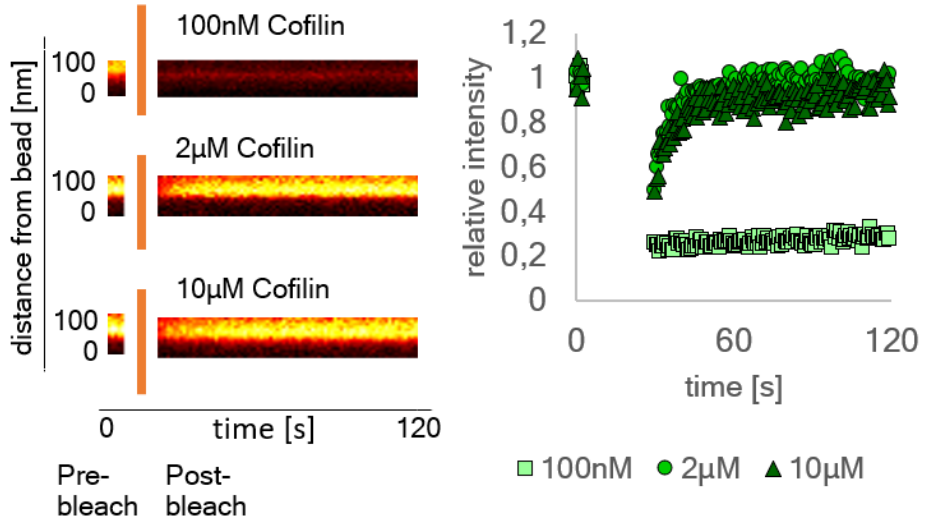

Figure 3.9: FRAP measurements of networks at different cofilin concentrations. A spot directly on the bead surface has been bleached. Left, a kymograph of the bleached spot depicts the intensity profile over two minutes. Shown are the frames pre-bleach and post-bleach. At 2 µM cofilin and 10 µM cofilin the recovery is fast compared to the 100 nM network. Additionally, the kymographs show that the recovery emerges from the bead surface (bottom) towards the exterior solution (top). The right plot shows the fluorescence intensity of the bleached spots is plotted against time. There is no significant difference visible between the networks at 2 µM cofilin and 10 µM cofilin. However, at 100 nM cofilin the recovery is slowed down. This suggests that the fluorescence recovery is strongly affected by the disassembly and replenishment activity of the cofilin machinery.

Additionally, the recovery of the fluorescence intensity measured at different time points (Figure 3.10). At 100 nM cofilin, the recovery time is slower than 0.1 s^{-1} as soon as 10 minutes after the beginning of the experiment. At 2 µM and 10 µM cofilin, these rates remain constant above 0.2 s^{-1}.

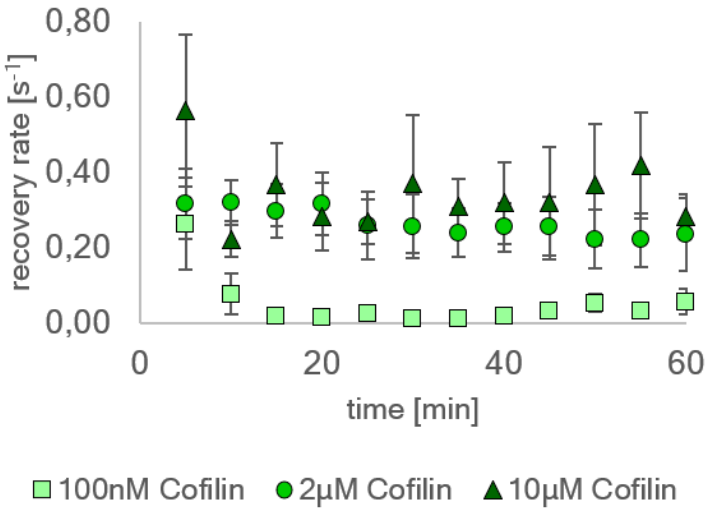

Figure 3.10: FRAP measurements used to quantify the actin turnover during different stages of the network elongation. The extracted fluorescence recovery rates are plotted over time for multiple beads. The recovery rates at 2 µM and 10 µM cofilin display the same trend over time, while the recovery rates at 100 nM cofilin decrease after 10 minutes of polymerization, which can be explained by monomer depletion. The networks at 2 µM and 10 µM cofilin do not show this decrease. Hence, disassembly and the recovery of the monomer pool can be accounted for maintaining the fluorescence recovery in these networks.

3.5 Actin turnover induces microsphere propulsion and spinning

One of the observations made in reconstituted, dynamic actin networks is the propulsion and spinning of microspheres (Figure 3.11). Surprisingly, this dynamics can only be achieved at intermediate concentrations of 2 µM cofilin. This suggests that a high actin turnover as determined by FRAP is necessary to propel a bead. One explanation why the spinning cannot be observed at higher cofilin concentrations is the missing net growth at these concentrations, as the balance of polymerization is shifted towards depolymerization due to the high sequestering activity of cofilin enhanced by CAP1.

The question arises why the beads are spinning. This can be explained by interactions with the glass surfaces. Here, the network has to push against the glass to polymerize normal to the bead. Although it has been observed that beads can push upwards through network growth by a maximum of 2 µm, this breaks the symmetry of the cortex. Thus, rotations parallel to the glass surface are highly favored.

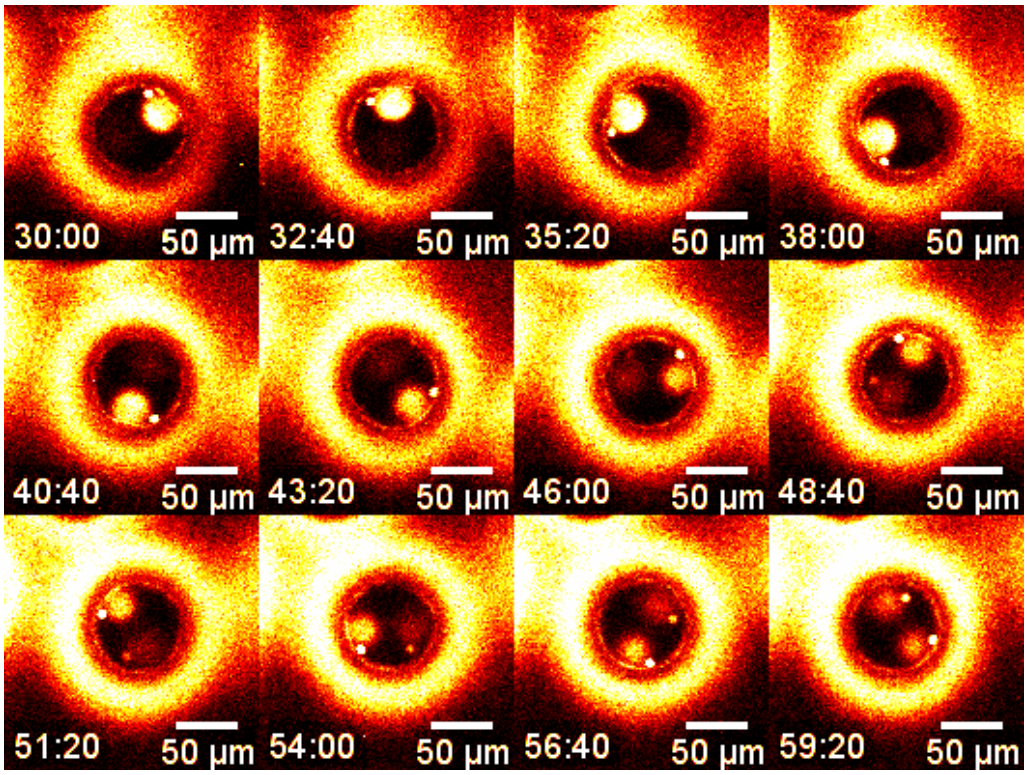

Figure 3.11: In the presence of ideal concentrations of cofilin, spinning of beads can be observed. Here, a network is formed by formin functionalized beads in the presence of 1.5 µM mCherry-cofilin. Depicted are individual frames of a timeseries, after 30 minutes of initial polymerization at a framerate of 80 s. For better visualization, only the fluorescence of the cofilin channel is shown.

No preferred directionality of the rotation could be observed. However, due to obstacles like other beads, the direction of spinning could change during the course of the experiment. The highest rotational speed that could be achieved was 0.3 rad/min, while typically slowing down after 1 h. After 2 h rotations completely stopped even in the presence of an ATP regeneration system. This can be explained by the degradation of formins which do not remain active at room temperature for longer than few hours.

3.6 Synergy between branched and linear treadmilling networks

To address the question how the dynamics of different network types interact with each other, is it necessary to test the effect of cofilin on actin networks polymerized by Arp2/3. To this end beads are functionalized with VCA (25 nmol per ml bead resin) which activates the Arp2/3 complex (300 nM) and thus initiates the formation of a localized branched actin network at the bead's

surfaces. The formin-induced networks exhibit dynamic turnover behavior, reaching network widths of 50 µm while the Arp2/3 induced branched network continues to polymerize reaching only widths of 5 to 10 µm but with a much higher filament density (6x higher density in branched compared to parallel network, Figure 3.12a-c).

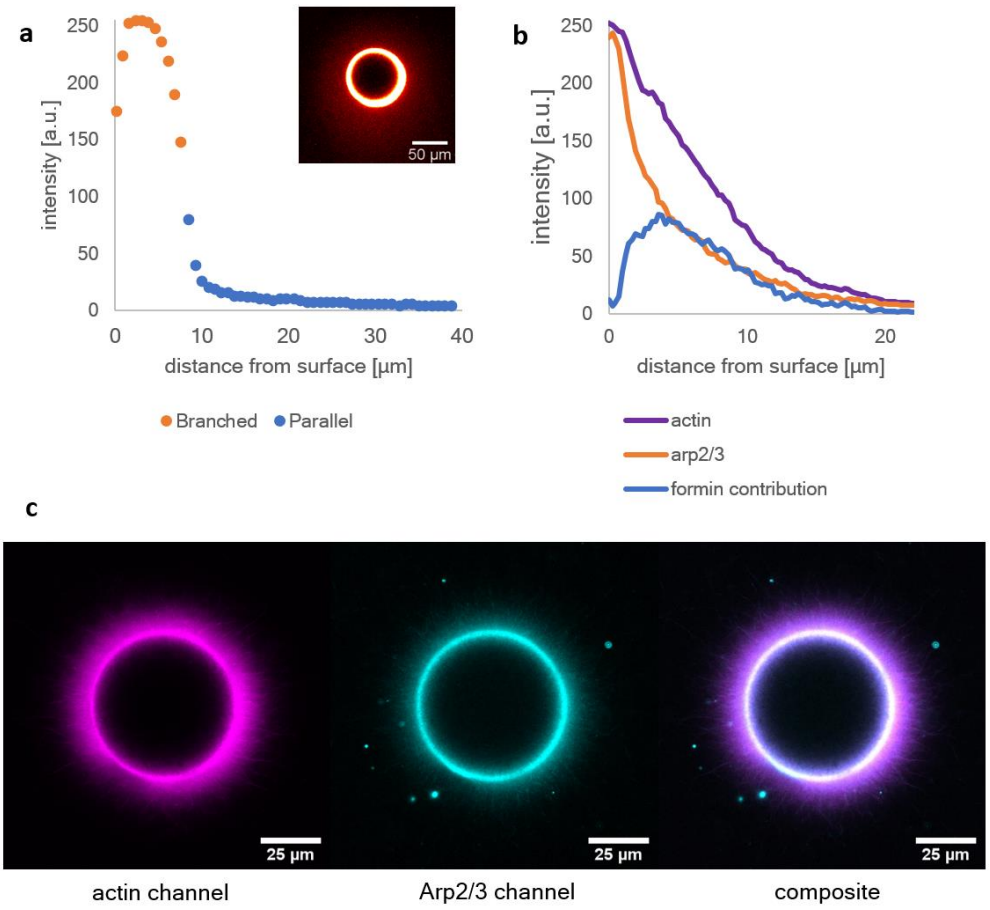

Figure 3.12: Visualization of the network colocalization in the presence of VCA/Arp2/3-complex and formin. Arp2/3 and formin are colocalized on the same surface. Two different types of networks form in the presence of 5 µM actin, 12 µM profilin 100 nM capping protein and 1.5 µM cofilin. **a** By adjusting the lookup table, the colocalized formin network can be visualized (confocal image corresponding to the depicted intensity profile). The intensity profile reveals a difference in intensities which accounts for the different densities of the colocalized networks. An arbitrary threshold (40% of maximal intensity in a.u.) is defined to distinguish between the branched and the formin polymerized part of the network. For geometrical reasons, the profile decreases over time. Therefore, to compensate for the dependence on the distance from the surface, the ratio between the intensities times the corresponding distances is used to calculate the intensity ratio. By calculating the intensity ratio of the branched to the formin polymerized network in that manner, the intensity of the branched part of the network is 6 times higher. **b** Intensity line plot corresponding to actin channel and Arp2/3 complex channel depicted in **c** Arp2/3 complex labeled with an Atto647N-maleimid dye is used to visualize the localization of Arp2/3 to confirm that the dense part of the network is indeed branched. The data shows that the Arp2/3 complex is colocalized with the densest area of the actin, which is in close proximity to the surface. This indicates that the 6 times higher intensity of this fraction of the network is indeed due to branching

activity. With increasing distance, less Arp2/3 is present compared to the fluorescence of actin. By subtracting the Arp2/3 fluorescence from the actin fluorescence, the contribution of formin induced polymerization to the network can be roughly visualized.

Already nanomolar concentrations of cofilin suffice to debranch and depolymerize the networks completely[46]. Indeed, no network can be polymerized in the presence of 50 nM cofilin (Figure 3.13b).

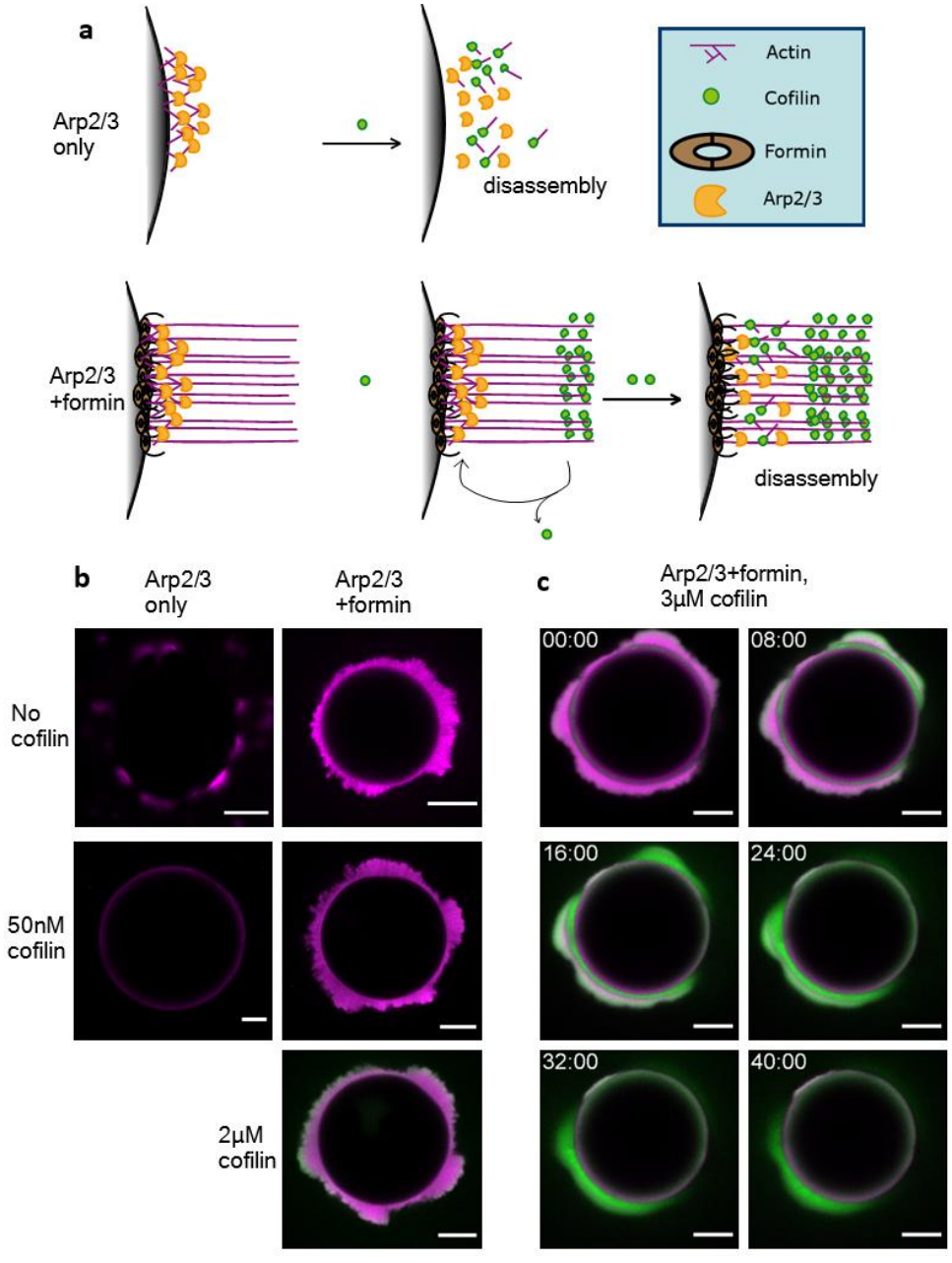

Figure 3.13: Colocalization of branched Arp2/3 polymerized networks with treadmilling formin networks. **a** Proposed model for the disassembly of branched networks in the absence or presence of formin. Arp2/3 (orange) is activated by His-VCA, which is immobilized on the NiNTA functionalized bead surface (25 nmol per mL of bead resin) and a branched actin (magenta) network forms. When cofilin (green) is present, the branches are disassembled. Therefore, no network is polymerized already in the presence of nanomolar cofilin concentrations at the employed nucleator density. When

formin (brown) is also present (12 nmol per mL of bead resin each), a colocalized network forms normal to that bead. By binding to the continuously polymerizing formin network, a steady state is achieved that locally depletes cofilin. Therefore, the branched network is still intact at concentrations up to 2 µM cofilin. Disassembly of the Arp2/3 polymerized network occurs only at higher concentrations. **b** Beads are functionalized with His-VCA with or without His-formin simultaneously. At 50 nM cofilin, no branches form when VCA and Arp2/3 are present alone, however, when formin is colocalized, a dense branched cortex forms that reaches a width of 5-10 µm. The density of the branched network is 6 times higher, hence the colocalized formin network appears too dark to be resolved simultaneously. The branched network remains stable in the presence of the formin network up to concentrations of 2 µM cofilin. Here, the tips of the branches that point away from the bead start to be decorated by cofilin. All beads were incubated in the corresponding cofilin concentration until there was no visible change to the network width or cofilin decoration for at least 10 minutes. **c** By increasing the cofilin (green) concentration above 2 µM, the actin (magenta) barbed ends of the network that point towards the bead surface are also decorated. Under these conditions, the branched network is gradually disassembled. In all images, actin is shown in magenta, cofilin is shown in green. The depicted timescale is in minutes. All scale bars represent 20 µm.

Yet, when both Arp2/3 and formin are present and mixed on the same bead surface (12.5 nmol each per ml bead resin), both network types polymerize simultaneously and colocalize. By gradually increasing the concentration of cofilin, it is possible to find that the branched network stays stable even up to cofilin concentrations of 2 µM (Figure 3.13b). Only once the cofilin concentration is increased from 2 µM to 3 µM does the branched network disassemble completely (Figure 3.13c). Thus, formin induced actin networks which extend beyond the Arp2/3 formed network shield the Arp2/3 networks against the effect of cofilin. This enables Arp2/3 networks to remain stable against debranching by cofilin even at high cofilin concentrations through the control of the local free cofilin concentration by the competing network (Figure 3.13a). Together, this shows how the local depletion of actin monomers and its binding partner cofilin affects the network and its resulting dynamics (Table 3.1).

Regime	Depletion	Net Growth	Dynamics
100 nM Cofilin (low)	Actin+Cofilin	+	-
2 µM Cofilin (intermediate)	Cofilin	+	+
10 µM Cofilin (high)	N/A	-	+

Table 3.1: Summary of the quantification of the network dynamics at different cofilin concentrations. A low cofilin concentrations, most of the actin is built into a stable network and the recovery is low due to low cofilin activity at only 100 nM. Thus, also cofilin is depleted at the surface and only binds to the pointed ends far away from the elongators. The net growth of the network is high; however, the internal dynamics are very low as determined by FRAP. At intermediate cofilin concentrations, actin is

recovered and high dynamics can be measured even in the presence of a net growth of the network. As shown by combining the formin network with Arp2/3, cofilin is depleted directly at the surface, thus creating a zone of undecorated actin. In these conditions, the spinning of microspheres can be observed. This can be explained by the presence of a network to push against while simultaneously maintaining high turnover. At high cofilin concentrations, the balance is shifted towards depolymerization. No net growth of networks can be observed, however the turnover at the surface remains high. This indicates that F-actin gets disassembled immediately after being elongated on a barbed end by formin.

3.7 Coupling of treadmilling actin networks to GUVs

The ability to control actin turnover actively opens up new possibilities when coupled with biomimetic frameworks like reconstituted GUVs. Analyzing the rotation of beads driven by global actin treadmilling has demonstrated how the actin polymerization is able to apply forces on functionalized surfaces. Thus, coupling this system with deformable surfaces should enable active shape changes. First, a network polymerized by formin without cofilin was encapsulated (Figure 3.14). Vesicles were produced with a phase separating lipid mix. In a lipid mix without separated lipid phases, the turnover should not be able to beak the symmetry on its own due to a homogenous force distribution.

The actin network is shown in magenta and appears as a diffusive cloud due to the density of actin and the noisy background due to labeled actin monomers. The phase separated lipids are shown in cyan. Without cofilin and CAP1 present, there should be no actin recycling. As a consequence, the vesicle's lipid channel does not display a difference in appearance when compared to typical empty vesicles as published elsewhere[41].

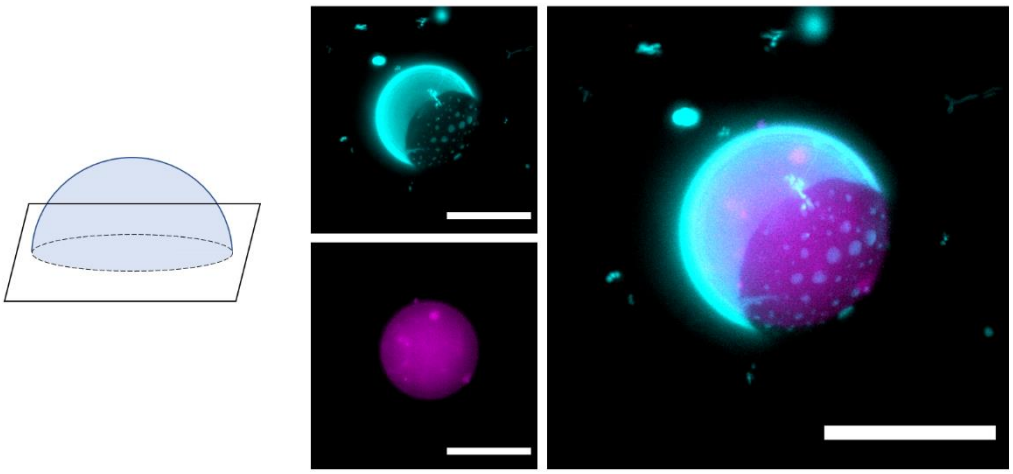

Figure 3.14: Phase separated vesicles combined with formin mediated actin network growth. Here, a hemisphere of a GUV is projected on a single plain. The Texas Red labeled lipid channel is shown in cyan, actin is shown in magenta. A lipid mix of 1 to 1 DOPC to DPPC is used to form vesicles displaying phase separation. Due to the labeling

of actin monomers, the network appears as a diffusive cloud. The solution encapsulated in the GUV contains the same proteins and concentrations used in bead experiments but without cofilin. Formin had to be added to the same solution instead of functionalizing the surface previously as washing or changing solutions is not possible in encapsulation experiments. A concentration of 1 µM formin is added and it can be assumed that all of the formin is binding towards the lipids due to the high availability (2.5% of total lipids) of Ni-NTA functionalized lipids.

Next phase-separated vesicles are prepared with formin elongated actin, cofilin and CAP1 to implement global actin treadmilling. Initially, these vesicles looked very similar to the vesicles prepared without the turnover system. Phase were clearly visible (Figure 3.15 a). For GUVs to be able to change their shape, excess membrane has to be available. Therefore, a deswelling procedure is used to slowly increase the osmolarity of the outside solution by 200 mOsm. Due to water being released from the vesicle, the vesicles deflate and become floppier due to excess membrane (Figure 3.15 b)

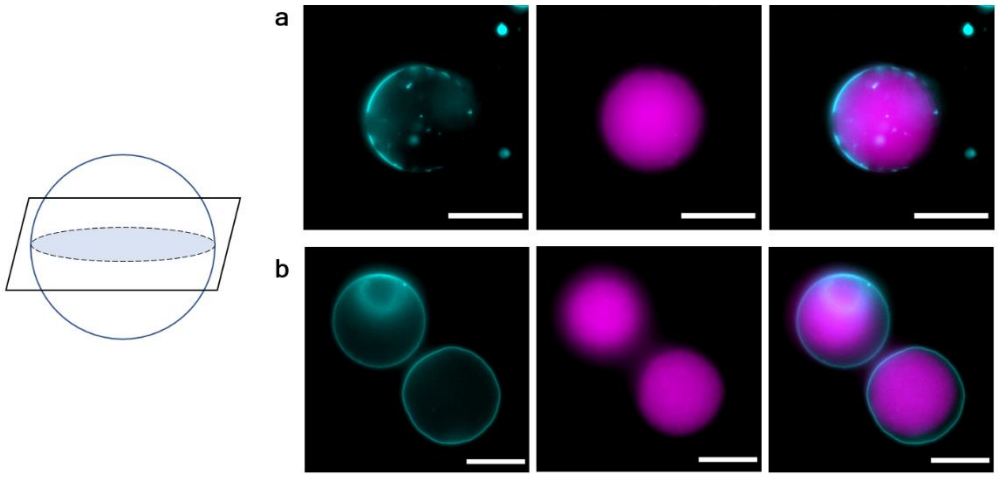

Figure 3.15: Phase separated vesicles before and after deswelling and coupled with cofilin mediated actin turnover. 2 µM cofilin are encapsulated in an actin polymerization solution prepared in the same way as described previously. Formins adhere to the NiNTA lipids. Due to the phase separation, the actin turnover should therefore be couple to the phases which appear fluorescent in the lipid (cyan) channel. **a** The equatorial plane of the vesicle before deswelling. The vesicle displays a clear phase separation. **b** The equatorial plane of vesicles after deswelling. The vesicles appear floppier and some vesicles show included vesicles, possibly due to the osmotic shock. The phase separation cannot be observed anymore.

Some vesicles show artifacts like inclusions of smaller vesicles due to the osmotic shock. Surprisingly, no vesicles display phase separation anymore after the deswelling. This might be due to the long incubation time to avoid drastic

changes in the osmotic pressure (about one hour per 100 mOsm). However, it is very likely that the phases get mixed due to the activity of the treadmilling network. The forces of the treadmilling filaments are directly transmitted to the lipids through formin which actively mixes the phases in the liquid membrane. Unfortunately, this cannot be shown by FRAP measurements, as it is not possible to fix the lipid layers of vesicles. Due to their fluidity it is impossible to define a stable region of interest.

Next, methylcellulose is added as a crowding agent. Methylcellulose is able to push filaments against the membrane. Thus, forces which are able to deform the vesicle might be possible. However, methylcellulose is also able to bundle filaments into bundles. This also occurred in the densely packed treadmilling vesicles. Since bundling inhibits the depolymerization by cofilin, no turnover is possible anymore and the network is trapped in a frozen state. Here, bundles are arranged almost nematically due to the dense packing at the membrane (Figure 3.16).

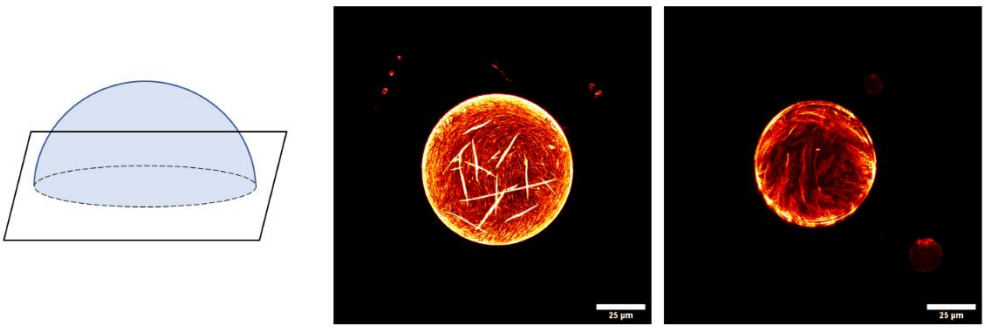

Figure 3.16: Vesicles with a treadmilling mixed trapped in a bundled state by methylcellulose. Here, 0.4% methylcellulose is encapsulated alongside the treadmilling mix. Only the actin channel is shown as a z-projection of a hemisphere. Due to the bundling, the network does not appear as a diffusive cloud anymore. However, the turnover is also prevented due to the inability of cofilin to depolymerize bundles. Thus, the network gets trapped in a bundled state and the previously active vesicles are completely passive.

3.8 Discussion

The presented experiments show that formin induced polarized network growth can reach the highest turnover rates at concentrations above 2 µM cofilin. Compared to single filament dynamics[47,48], these elongation speeds are 10 times slower. This can be attributed to the fact that the polymerization kinetics of networks is diffusion limited and that the actin monomers are locally depleted at the surface of the bead by the presence of a high density of active filament

ends. Similar effects were observed for branched networks polymerized by Arp2/3, at a significantly (10x) lower concentrations of cofilin[45,49].

The diffusion times limiting the growth rate depend critically on the cofilin concentration. This is best seen by analyzing the intensity profiles to identify areas in the network that are decorated by cofilin and where the disassembly of monomers thus occurs. Indeed, the distance at which the ratio of cofilin to actin is highest depends strongly on the cofilin concentration. At 100 nM mostly undecorated actin exists and only the bulk actin monomer concentration can be used for elongation, which needs to diffuse over the total actin cortex thickness of 40 µm. At 2 µM cofilin a clear cofilin decoration maximum is found at approx. 15 µm from the surface. Hence, for the latter the monomer diffusion time would be 7 times shorter than for 100 nM cofilin concentration. The recovery rates in these two equilibrated states drop on average by a factor of about 6 as measured by FRAP, which fits very well the diffusion time difference. The replenishment of the active monomer pool is achieved by the presence cofilin and enhanced by a factor of 2 by the addition of CAP1 (Figure 3.17).

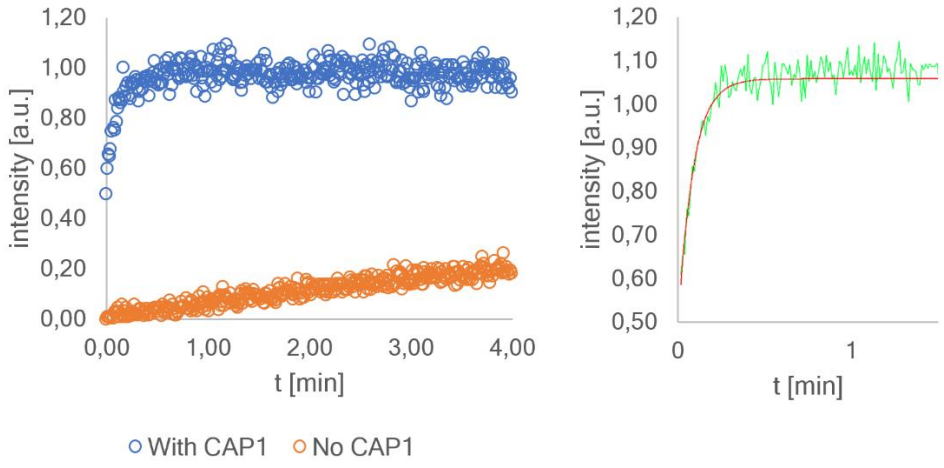

Figure 3.17: CAP1 dependent monomer turnover determined by FRAP recovery. The FRAP recovery of Atto 488 NHS-ester labeled actin is measured in the presence of 2 µM Cofilin with or without 1 µM CAP1. The recovery rates are extracted with a single exponential fit with the Leica FRAP wizard software. For samples without CAP1, a plateau value cannot be reached. For the shown experiment with 1 µM CAP1, the extracted FRAP recovery rate is 5,1 s. For all other cofilin concentrations, the recovery rate is at least double for samples with CAP1 when compared to samples without CAP1. An example for a single exponential fit achieved with the Leica FRAP wizard software is shown on the right, where the data is shown in green and the corresponding exponential fit as red line.

Thus, the increase of local disassembly and recycling of the monomers to ATP monomers at higher cofilin concentrations leads to an increase in the monomer flux and accounts for high turnover rates in even dense networks. Together, the polar networks described here are self-sustained by a constant flow of recycled monomers from the pointed ends to the barbed ends.

As these turnover dynamics occur at significantly higher concentrations of cofilin than those observed for Arp2/3 induced networks, the question arises of how the dynamics of these two types of networks interact. Branched networks are stable, even at concentrations up to 2 μM when polar formin-nucleated networks are simultaneously present and deplete the cofilin locally, and thus prevent its diffusion towards the Arp2/3 generated network. Therefore, the presence of the actin network itself sets the effective local concentration of cofilin by its local depletion by binding. This in turn determines the resulting local effects of cofilin on the network dynamics. Such localized depletion feedback loops may turn out to be essential for explaining the observed localized organization of treadmilling actin networks in cells. This work extends the concept of a global treadmilling process, where coexisting networks are modulated by a common actin monomer pool[11] to also include the localized depletion effects of the actin binding partners. Thus it is not only the actin monomer availability which regulates the homeostasis of actin cytoskeletal networks, but the local availability of depolymerization factors and accessory proteins as well[50,51].

The resulting effects are synergistic in nature and can ultimately be key to our understanding of the observed specificity of maintaining the competing and local demands of stability and dynamics of actin networks in cells.

4. Mechanistical analysis of CAP1 induced nucleotide exchange

Recent publications suggest an important role of CAP1 in the dynamic organization of the actin cytoskeleton[52,53]. One of the first discovered functions of CAP1 is its binding towards G-actin. Similar to profilin, CAP1 prevents the spontaneous polymerization by binding towards monomers to filament barbed ends[54–58]. As mentioned previously, CAP1 is a hexameric protein with an N-terminal part responsible for side-binding of actin filaments and enhancing cofilin activity by inducing discontinuities in the filament structure[59–61]. Conversely, the C-terminal part of CAP1 acts as a nucleotide exchange factor for actin and is used in reconstitution experiments in this thesis to maintain a pool of active monomers, similar to processes in cells[14,62–64].

In vivo, the sequence of CAP1 displays a surprising conservation throughout different species[65–67]. This suggests a fundamental role as an actin regulator. This conservation is especially pronounced in the N-terminal part of CAP1 where coiled β-sheets form six right-handed helices[68], although variation of the C-terminal part exist in different species. Among the functions of CAP1, the nucleotide exchange is suspected to be the most important one, although this function is partly met by profilin: Like CAP1, profilin is able to bind monomers and has been shown to connect signals sent by biochemical pathways to the actin cytoskeleton by binding several other proteins and membrane-associated phosphoinositides[69]. Additionally, profilin shares synergies with cofilin by promoting the actin turnover, by modulating barbed-end assembly rates and nucleotide exchange rates[70–73]. However, the role of profilin in enhancing the nucleotide exchange rates of actin is still unclear[74].

The goal of this chapter is to evaluate the long-standing debate on the importance of profilin and CAP1 in their role as nucleotide exchange factor. MST is used to determine binding affinities of multiple proteins associated with the turnover cycle of globally treadmilling actin networks. In combination with kinetical data derived from nucleotide exchange experiments a quantitative molecular mechanism can be postulated. By this means a synergistic effect is discovered, as cofilin and CAP1 facilitate the binding of the respective component towards the actin complex. From this data the idea arises that CAP1 is the crucial component necessary for nucleotide exchange in the presence of cofilin, while profilin is more efficient in the absence of cofilin, or, due to its higher affinity towards ATP-actin more involved in stabilizing ATP-monomers for

nucleator-assisted elongation. Taken together, the importance of CAP1 as a component in global actin treadmilling becomes evident as the maintenance of an ATP-monomer pool is a critical mechanism to achieve a high turnover and cannot be reached by profilin alone.

4.1 Analysis of the actin turnover system

Binding studies on the globally treadmilling actin complex are performed by means of microscale thermophoresis (MST). As described in the methods section, MST takes advantage of the movement of proteins along a temperature gradient. This can be written as a flow j along a temperature gradient ∇T[75-77].

$$j = -\nabla c \cdot D - c \cdot D_T \cdot \nabla T$$

Thermophoresis can lead to either depletion or accumulation of particles at a concentration c. The mass flow is determined by the diffusion coefficient D and the velocity of the thermo-diffusion given by the coefficient D_T. By integrating this expression, the steady-state c_{ss} at a temperature increase ΔT is described as

$$c_{ss} = c \cdot e^{-S_T \Delta T}$$

where S_T, the Soret coefficient determines the steady-state and is defined as

$$S_T = \frac{D_T}{D}$$

The ratio of particle concentrations at the hot or cold temperature can be written accordingly depending on the Soret coefficient and can - due to the low temperature difference applied in MST of typically only 2-6 K - be linearized[76].

$$\frac{c_{hot}}{c_{cold}} = e^{S_T \Delta T} \approx 1 - S_T \Delta T$$

The intensity signal I measured by the MST device is composed of the normalized fluorescence I_{hot}/I_{cold} and the T-jump $\delta F/\delta T$ which is the contribution of the enhanced fluorescence of the dye due to the increased temperature. When taking this increased fluorescence yield into account

$$I = 1 + (\frac{\partial F}{\partial T} - S_T) \cdot \Delta T$$

describes the analyzed signal. Now, the amplitude of the fluorescence signal is used to quantify the fluorophore and ligand binding reaction by titrating the

ligand in a concentration series. The amplitude changes depending on the fraction of ligands bound to the fluorophores and thus reflects the equilibrium as such[78]:

$$I = (1 - x) \cdot I_{unbound} + x \cdot I_{bound}$$

Here, x is the fraction of fluorophores bound to ligands. This results in thermophoresis traces and sigmoidal binding curves as shown in Appendix A1. Fitting the sigmoidal curves as described in the methods section is used to determine the dissociation constant K_D, which describes the ratio between unbound fluorophore [F] and ligand [L] and the fluorophore-ligand complex [FL], as shown below:

$$K_D = \frac{[F] \cdot [L]}{[FL]}$$

MST was used to quantify the binding affinities of actin towards the proteins used in global actin treadmilling (Table 4.1). The K_D of profilin towards ATP-G-actin was 3 times lower than towards ATP-F-actin. Surprisingly, the affinity of formin towards ATP actin was very high in comparison, as indicated by a ten times lower K_D.

Fluorophore	Ligand	K_D
G-Actin488	BSA	N/A
F-Actin488	BSA	N/A
G-Actin488	Profilin	251 ± 0.003 nM
F-Actin488	Profilin	721 ± 6.57 nM
G-Actin532	Formin	16.5 ± 18.75 nM
G-Actin647N	Cofilin	5.51 ± 0.179 µM
G-ADP-Actin647N	Cofilin	271 ± 18.8 nM

Table 4.1: Results of MST experiments on ATP-actin or ADP-actin and different actin binding proteins. Bovine Serum Albumin (BSA) is used as a negative control. G-actin and F-actin binding experiments are performed in G-buffer or F-buffer additionally containing 0.01% Tween20 respectively. Tween is added to avoid unspecific interactions or sticking of proteins to the capillaries. The MST traces and fits to the sigmoidal binding curves are shown in Appendix A1.

This allows for the postulation of a molecular model to describe the thermodynamic relationship between the proteins used in the reconstitution of globally treadmilling actin networks elongated by formin (Figure 4.1).

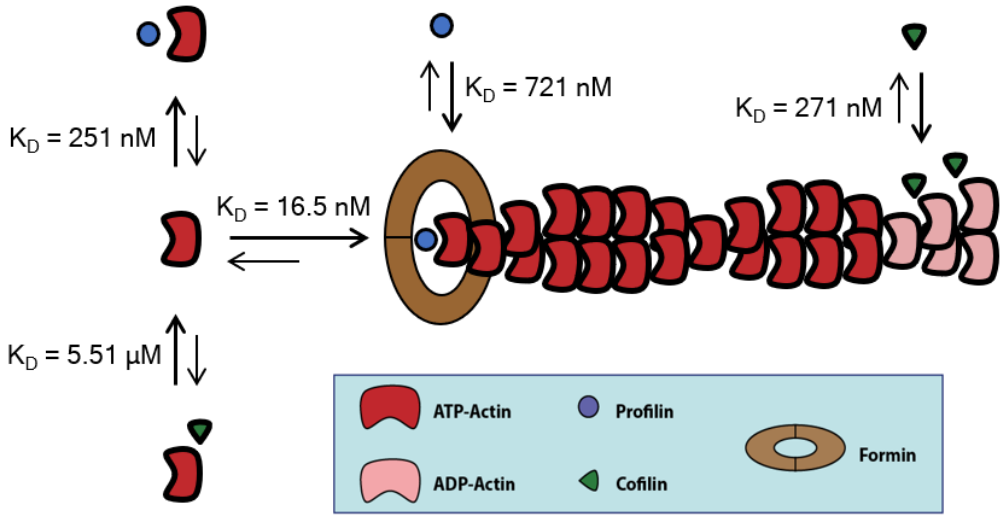

Figure 4.1: Model for formin mediated actin elongation in globally treadmilling actin networks. The determined dissociation constants are added to the model of formin mediated actin elongation. Larger arrows indicate the preferred state of the equilibrium. Profilin is shown in blue, cofilin in green, formin in brown and actin in red or light red for ADP-actin monomers.

Although profilin has been previously identified as nucleotide exchange factor in treadmilling networks, this data suggests that CAP1 has a dominant role in nucleotide recovery in the context of globally treadmilling networks. This is due to the stabilization of ADP-actin via cofilin binding. However, a tripartite complex composed of actin, cofilin and CAP1 seems to be responsible for the nucleotide exchange in networks with a monomer pool maintained by cofilin. This complex is now further quantified.

4.2 Kinetical analysis of actin nucleotide exchange

The exchange rates of nucleotides can be analyzed by using ε-ATP. The nucleotide exchange assay makes use of the increased fluorescence of ε-ATP when bound to an actin monomer. The rates were normalized to the recovery rate of only ADP-actin with no additional proteins present (Figure 4.2).

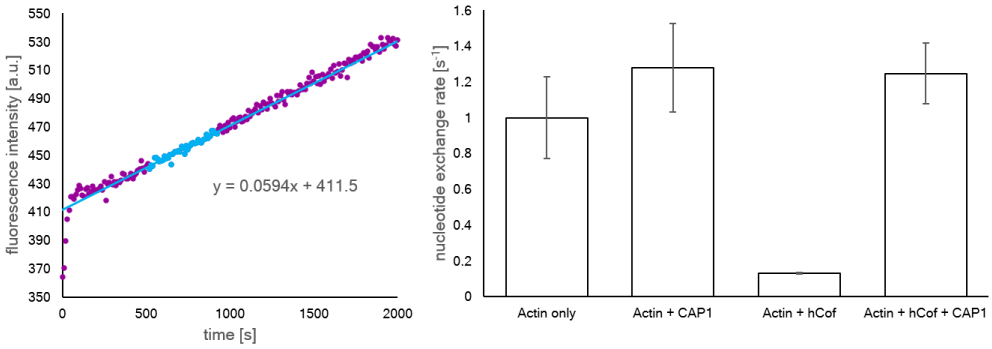

Figure 4.2: Nucleotide exchange assay and nucleation rates in the presence of various components of the nucleotide exchange complex. An example of a fluorescence recovery curve is shown on the left. The purple points represent the measured fluorescence intensity. The cyan dots were chosen to plot a line which determines the recovery rates shown on the right. At least three individual experiments were used for the statistical analysis of the recovery rates when only actin, actin and CAP1, actin and cofilin and the tripartite complex were present.

Indeed, when cofilin was present, a slowdown of the exchange rate by a factor of 10 could be observed. The addition of CAP1 did not change the exchange rate significantly compared to actin alone, however, when both CAP1 and cofilin were present, the exchange rate was recovered. In fact, the exchange rate even reached higher levels compared to actin alone.

4.3 Binding studies of the nucleotide exchange complex

This tripartite complex, responsible for the maintenance of an active monomer pool in actin turnover was further quantified with MST binding studies. MST was used to vary the concentration of a ligand while keeping a constant amount of the third component present. The resulting binding curve then represents the affinity of the ligand to the complex (Table 4.2).

Fluorophore	Ligand	Additive	K_D
mCherry-hCof	CAP1	-	111 ± 0.006 nM
mCherry-hCof	CAP1	ADP-Actin	71 ± 0.004 nM
mCherry-hCof	ADP-Actin	CAP1	89 ± 0.007 nM

Table 4.2: Results of MST experiments characterizing the nucleotide exchange complex. Binding affinities are determined in the presence of a third component (additive), thus characterizing the tripartite complex of actin, cofilin and CAP1.

Very low K_D values could be measured for all three components toward the complex. This suggests a cooperative kind of binding, meaning that each component facilitates the binding of the other components by binding (Figure 4.3).

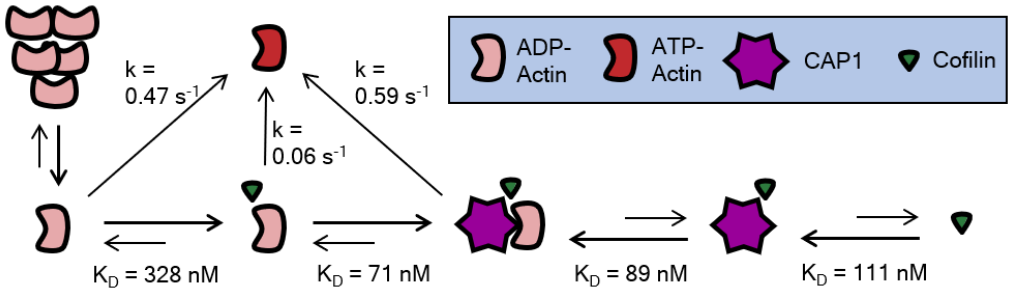

Figure 4.3: Quantitative molecular mechanism of the actin nucleotide exchange complex. The reported findings demonstrate a mutual interaction of all components involved in the tripartite complex. Together a highly efficient cycle of monomer recovery is formed. Hereby, cofilin assists in the dissociation of ADP-monomers, an activity further enhanced by CAP1. Then, monomers are bound to the cofilin-CAP1 complex in a cooperative manner. Due to the activity of CAP1, a fast recovery rate leads to nucleotide exchange and the dissociation of the ATP-monomer which is now activated again for nucleation.

4.4 Discussion

The mechanism discussed here describes the maintenance of an active monomer pool in globally treadmilling networks. This concludes that in a reconstituted network, these three components are sufficient to form a turnover cycle for globally treadmilling networks. Yet, open questions remain of how the two parts of the CAP1 protein interact in a complex with actin and cofilin[79]. The N-terminal part has been shown to be responsible for the cofilin binding quantified here[80], while the C-terminal part has been shown to interact with profilin and SH3 domains via its proline-rich regions[52,62,81]. Also, the CARP domain found in CAP1 is the requirement for the binding of ADP-actin specifically[63,68]. Only recently, the crystal structures of the nucleotide exchange complex were solved, showing that the nucleotide exchange occurs packed between the actin binding domain of CAP1 and two ADP-actin monomers[13]. Yet, this answers only one question of the elusive functions of this complex, while the different functionalities of this complex, such as the dissociation of monomers, the nucleotide exchange and interactions of the different units of the complex remain elusive.

5. Reorganization of active actin networks by intra-bundle contractions

One of the fundamental requirements of cellular motility, cell division and morphological changes is the ability of cells to modulate their shape[82-85]. This requirement is met by the cellular cortex which provides not only stability, but also the ability to adapt its mechanical properties. The cellular cortex is an array of filamentous actin, myosin and various actin-binding proteins. The role of myosin in actin-based shape modulation is crucial, as it provides not only contractility, but also drives the turnover of actin filaments[86,87]. Polar and apolar aligned filaments are able to organize into bundles and bundles can be temporarily stabilized by crosslinking molecules, for example during the formation of filopodia[88]. Stable, crosslinked bundles are also important for the formation of contractile stress fibers which act as crucial force transmitters throughout the whole cell[89,90]. The role of myosin is hereby especially evident, as it is not only essential for the contractions in the cortex or along stress fibers, but also adds to the turnover of actin by contributing to the depolymerization of filaments and bundles[8,91].

The goal of this chapter is to show how myosin introduces an active state in a reconstituted actin cortex elongated and anchored to a supported lipid bilayer (SLB) by VASP. VASP is not only able to elongate, but also to bundle actin filaments *in vitro* and is associated with the formation of filopodia and general lamellipodial motility[92-94]. Remarkably, myosin is able to contract on an intra-bundle level in these networks. This leads to extensile contractions, which have been predicted theoretically[95], but have so far only been reported for microtubules[96]. Furthermore, myosin strongly affects the network growth mechanism in this system. In networks without myosin, filaments are elongated along the previously formed VASP bundles. The extensile, intra-bundle contractions reported here, however, lead to a swelling of bundles into clusters. These clusters nucleate filaments and bundles of actin, leading to an aster shape. Their altered, swelling-like growth can be explained by a mechanism of contraction, stress-induced nicking and VASP-mediated repair by recruitment of monomers towards the newly formed barbed ends. The myosin-determined growth mechanism presented here may very well answer many open questions also *in vivo*, as it provides a fundamental way for cells to break the symmetry in their cortex while fulfilling both demands of stability and inherent dynamics.

5.1 Reconstitution of a model actin cortex

To reconstitute a system mimicking the properties of a cellular membrane, a supported lipid bilayer (SLB) was produced to provide a fluid surface which, among other biomimetic properties, enables the diffusion of His-tagged proteins bound to the Ni-NTA functionalized fraction of lipids. Actin networks containing a fraction of 10% fluorescently-labeled monomers were allowed to form both in the absence and presence of NMMII (Figure 5.1a-b).

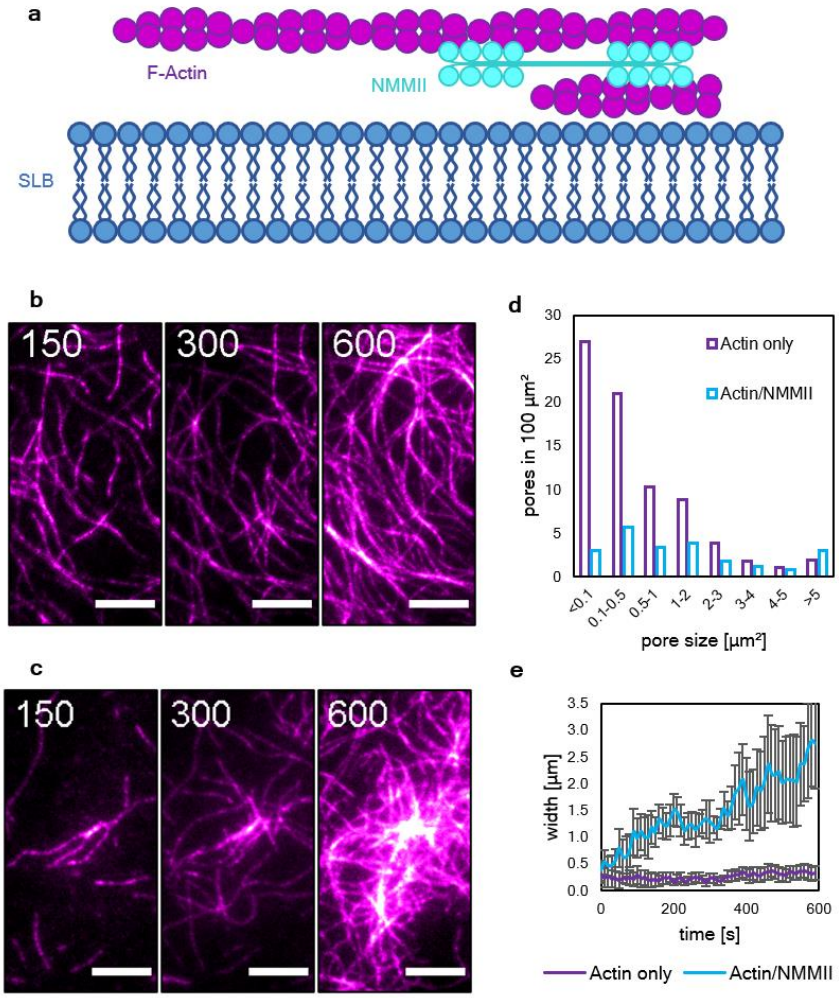

Figure 5.1: The activity of NMMII leads to the growth of clusters in actin networks bundled by methylcellulose. **a** Illustration of the experimental setup. A polymerization solution containing actin (magenta) in absence or presence of NMMII (cyan) was added to an SLB (blue). Actin was crowded on the fluid surface due to a high concentration of methylcellulose (0.8%). **b** The resulting actin network was imaged by TIRF microscopy. Bundles of actin formed spontaneously due to the presence of methylcellulose. **c** Here, the network was polymerized in the presence of NMMII and clusters formed in a swelling manner. In both cases, time frames at 150 s, 300 s and 600 s after the initiation of the experiment are shown. Scale bars = 10 µm. **d** Histogram of the pore sizes in both network types in an area of 100 µm. **e** The width of bundles and clusters in both networks type measured at multiple locations throughout the network. While the width of bundles in the absence of NMMII remains almost constant with 250 nm, NMMII-containing

clusters grow on overage almost ten times as wide and much more disperse. At least ten locations were evaluated for both network types.

In the absence of NMMII, after 10 minutes of polymerization, a network of bundles formed due to the presence of 0.8% methylcellulose. In the presence of NMMII, the initially polymerized bundles grew wider with time and eventually formed clusters (Figure 5.1c). These clusters did not display an aster-like shape that would be typical for clusters that pull bundles towards their center. Rather, actin monomers seem to be incorporated in the center of the cluster, effectively leading to an outwards growth. Both networks were further quantified by comparing the pore sizes (Figure 5.1d). In the absence of NMMII, smaller pores in the range of <0.1 to 0.5 µm² were about ten times more frequently found. In the presence of NMMII, much larger pores formed due to the altered growth.

The width of bundles in the absence of NMMII was considerably smaller and remained more or less constant over time (200 nm – 300 nm), while in the presence of NMMII bundles swell into cluster which were on average ten times as wide (Figure 5.1e).

5.2 Cortex adherence by VASP

To study this unanticipated effect of NMMII on actin bundles, the membrane associated protein VASP was adhered as a tether to the SLB to control the bundling and elongation of actin (Figure 5.2b). Additionally, a flow chamber was utilized with which protein mixtures can be added in a step-wise fashion. VASP, which was added initially, is an actin binding, tetrameric protein containing G-actin (GAB) and F-actin binding domains (FAB) (Figure 5.2a) and acts as processive actin polymerase able to form bundles *in vitro* by binding multiple filaments.

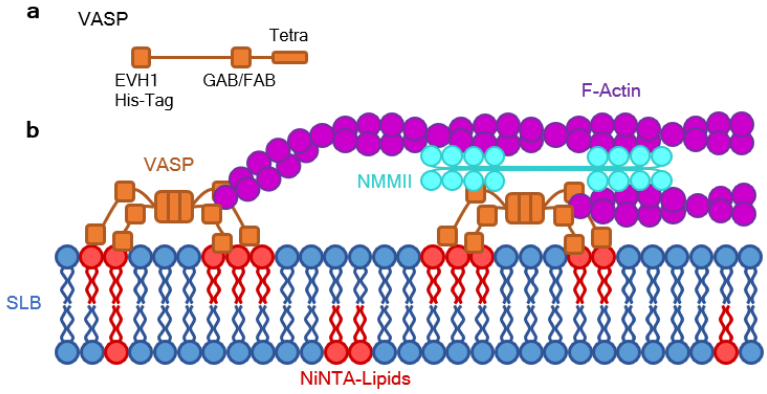

Figure 5.2: VASP construct and experimental setup. a A graphical representation of the employed VASP construct is shown to highlight the relevant domains. The N-terminal

EVH1 domain is functionalized with a 6xHis-Tag to enable association of VASP with the Ni-NTA lipids. GAB and FAB mark the localization of the G-actin and F-actin binding domains of VASP. Tetra represents the tetramerization domain. **b** Illustration of the experimental setup. VASP (orange) added to the supported lipid bilayer (blue) in an initial step allows binding to the fraction of 2.5% Ni-NTA functionalized lipids (red). A polymerization solution containing actin (magenta) with or without NMMII (cyan) was added. Here, VASP was able to anchor and bundle elongating filaments. NMMII was introduced to study the effect of the motor within the bundled network.

After incubating for five minutes, unbound VASP was removed and the same polymerization solution for TIRF microscopy was added, however the concentration of methylcellulose was lowered to 0.4% (w/v) which was below the critical concentration for bundling when only actin is present (Figure 5.3).

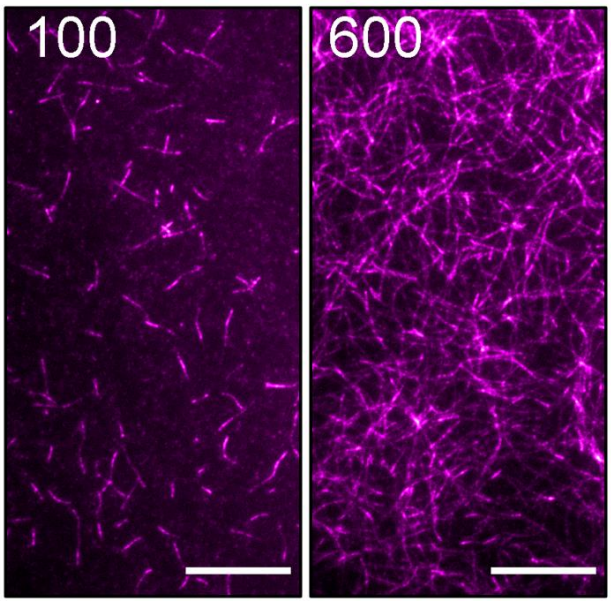

Figure 5.3: Critical concentration of methylcellulose for actin bundling. At concentration of 0.4% methylcellulose, no bundling of actin filaments can be observed in the absence of VASP. Here, an actin network on a supported lipid bilayer is polymerized without anchoring VASP as a control for low methylcellulose concentrations of 0.4%. Only the polymerization of single filaments can be observed. To form bundles and enable intra-bundle contractions without VASP, concentrations of 0.8% methylcellulose were used. The depicted time scale is in seconds, scale bars = 10 µm.

In these conditions, actin networks were polymerized both in the absence and in the presence of NMMII. In the absence of NMMII, a network of actin bundles was formed (Figure 5.4a). These bundles only appeared when VASP is present and are therefore a result of the bundling activity of VASP. In the presence of NMMII, the bundles appeared thicker and larger pores emerged in the network (Figure 5.4b). This was further quantified by analyzing the pore sizes in both networks. In the absence of NMMII, more small pores in the range of <0.1 to 2 µm² appeared in the network. However, the activity of NMMII led to more pores in the range of 3 to >5 µm² (Figure 5.4).

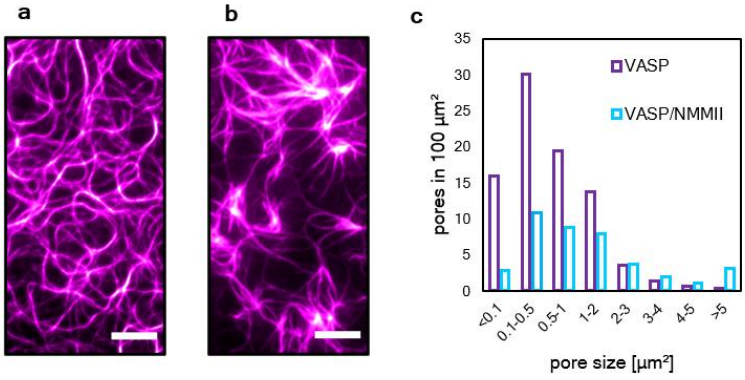

Figure 5.4: NMMII introduces a novel network phenotype on actin networks anchored to supported lipid bilayers by Ena/VASP. **a** Actin network polymerized on VASP-functionalized lipid bilayers imaged by TIRF microscopy. **b** Here, the network was polymerized in the presence of NMMII. Both images were taken 20 min after the initiation of the polymerization reaction. Scale bars = 5 µm. **c** Histogram of the pore sizes in both network types in an area of 100 µm². In the presence of NMMII, the network displays larger pores and less smaller pores in the range of <0.1 to 2 µm² compared to the network phenotype without NMMII.

5.3 NMMII activity is determined by intra-bundle contractions

With only VASP and actin present new filaments were initially nucleated within the first 3 – 5 min of network polymerization followed by bundling of these filaments and expansion of the network (Figure 5.5a). With NMMII present, the initial growth phase was very similar in terms of filament elongation and filament intensity, however, after 5 min large clusters with diameters of over 3 µm appeared. Large scale contractions with rupturing of bundles comparable to what has been reported with skeletal muscle myosin II[97] could not be observed, yet the clusters grow wider over time seemingly in a swelling manner (Figure 5.5b). To reveal more details about the molecular basis of this growth, a magnified version is shown (Figure 5.5c). Here, the activity of NMMII could be observed much more clearly. The depicted VASP bundle splits into two bundles within 100 s and 280 s of polymerization. The splitting and fluctuations of the bundle can also be observed in the z-projection of all frames between 100 s and 280 s (Figure 5.5d). The intensity profile of the here depicted yellow line is shown to visualize how the distance between the split bundles fluctuates and increases to almost 2 µm over time (Figure 5.5e-f). The bundle opens and closes multiple times until the intra-bundle distance increases linearly after 240 s. The maximal slope that can be measured here is 0.017 µm/s which is well in the range of what has been reported for NMMII[98]. This demonstrates how in this system, NMMII contractions occur on an intra-bundle level. Contractions that reach over multiple bundles cannot be observed. Intra-bundle contraction

events like the one depicted here can be observed all over the network and prime the emergence of clusters that can be observed at later stages of network growth.

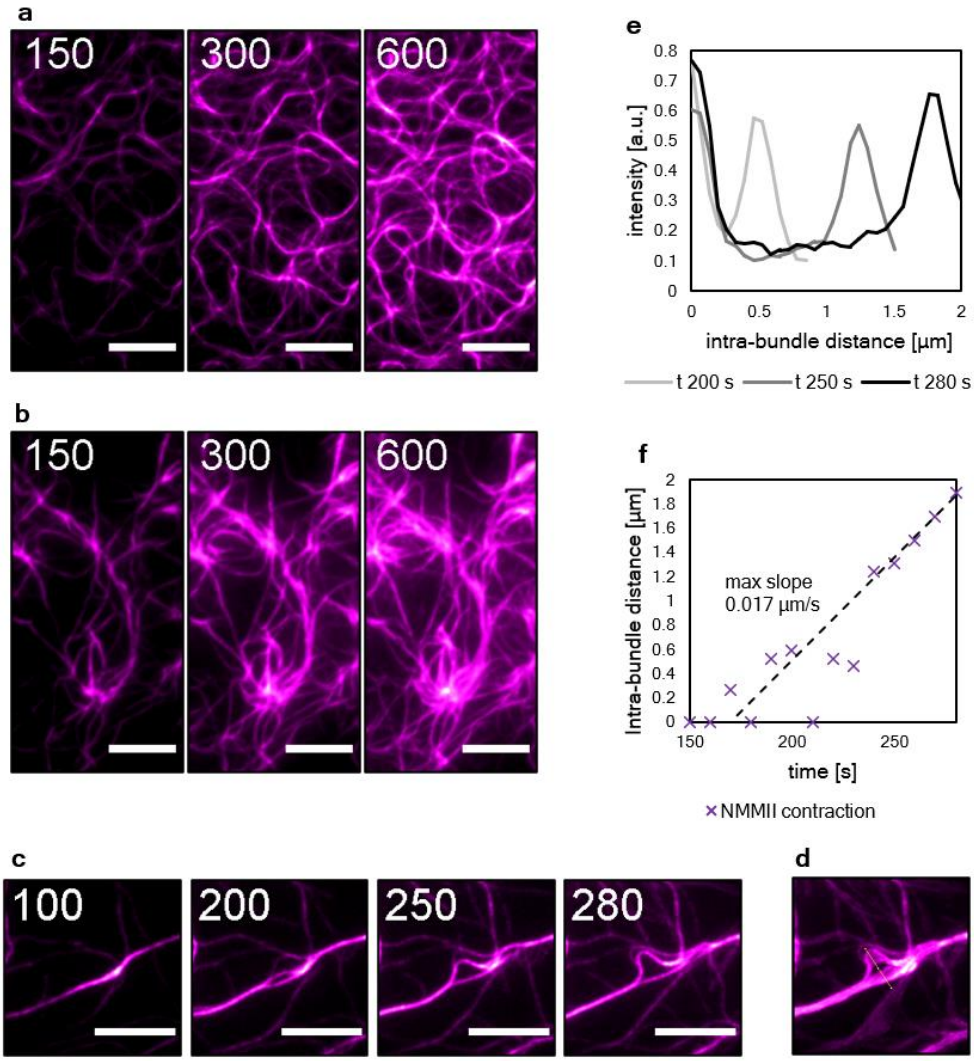

Figure 5.5: The rearrangement of bundled VASP networks by NMMII is caused by intra-bundle contractions. **a** Time resolved TIRF imaging of actin network (magenta) polymerization on VASP functionalized supported lipid bilayers in the absence of additional actin-binding proteins. **b** Polymerization in the presence NMMII. In both cases, time frames at 150 s, 300 s and 600 s after the initiation of the experiment are shown. The elongation of filaments along preexisting filaments within the bundles can be observed, effectively leading to wider bundles over time with VASP alone, while in the presence of NMMII the fluctuation of bundles and also the emergence of clusters could be observed. Scale bars = 10 µm. **c** Magnification to visualize the activity of NMMII. Intra-bundle contractions leading to bundle fluctuation and splitting of bundles occurred only in the presence of NMMII. Here, time frames at 100 s, 200 s, 250 s and 280 s are shown. Scale bars = 2 µm. **d** Intensity projection of every frame between 100 s and 300 s at a frame rate of 10 s. A line (yellow) was drawn to evaluate the intensity profiles of the two bundles over time. **e** Intensity profiles at 200 s, 250 s and 280 s after the initiation of the experiment representing the previously shown yellow line. The data were normalized to the first peak which represents the lower of the two split bundles. **f** The distance between the two intensity peaks over time is shown and represent the

distance of the split bundles. The distance fluctuated initially since the bundles joined and split multiple times but after about 250 s the bundles began to split with a linear velocity. The slope was determined for the five last time-frames to calculate the speed of contraction (0.017 µm/s).

5.4 Time resolved analysis of the model actin cortex

The elongation of filaments is tracked by subtracting time-resolved TIRF images of a network without NMMII from 200 s to 600 s after initial polymerization (Figure 5.6a) frame by frame. The subtracted frames are color-coded and then projected on a single layer (Figure 5.6b). Thus, the growth mechanism of VASP networks without NMMII is visualized. After the polymerization of the initial single filaments, subsequently elongated filaments grow alongside the previously grown network. In this way, bundles grew wider and increased in intensity filament by filament. The bundles themselves act as tracks for new filaments as shown previously[99], guiding the growth of the network. While the growth of the network in the presence of NMMII looks similar during the initial phase, this changes drastically once initial bundles have formed after 200 s (Figure 5.6c-d).

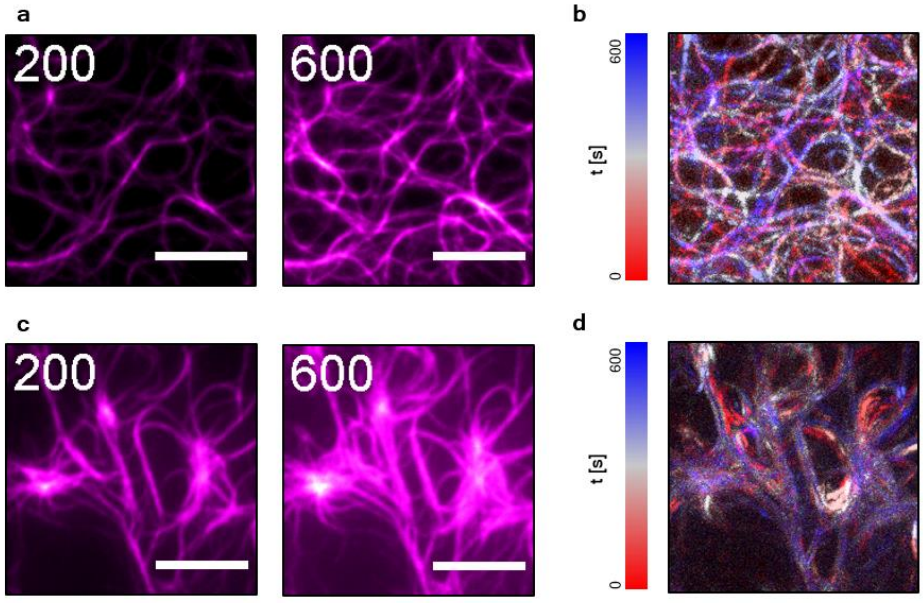

Figure 5.6: The growth mechanism in VASP anchored actin networks is dependent on the presence of NMMII. **a** Time resolved TIRF images of a VASP-anchored actin (magenta) network at 200s and 600s after initiation of actin polymerization. **b** Time frames were subtracted from each other to visualize freshly incorporated actin over time. The subtracted frames are color coded with a temporal lookup table from red over white to blue to show that filament growth occurs alongside previously formed bundles. This is apparently due to barbed-end elongation of filaments that are guided and captured by VASP within the bundles. **c** Time resolved images of the network in the presence of NMMII. Here, clusters without visible inward contraction were observed. **d** Subtracted time frames of the networks with NMMII. Here, barbed end elongation along previously

formed filaments could not be observed. Monomers were incorporated over the entire area of the cluster. The intensity in the subtracted frames was partially affected by the fluctuations caused by the activity of NMMII. Time is in seconds, scale bars = 5 µm.

In this case, the elongation of individual filaments could not be observed. The growth and expansion of the clusters was achieved by a fundamentally different mechanism. The incorporation of monomers tracked by the temporal color code occurred evenly distributed over the surface area of the cluster. This led to a swelling of the cluster from the inside out, as more and more monomers were incorporated in the inner regions of the cluster at later stages.

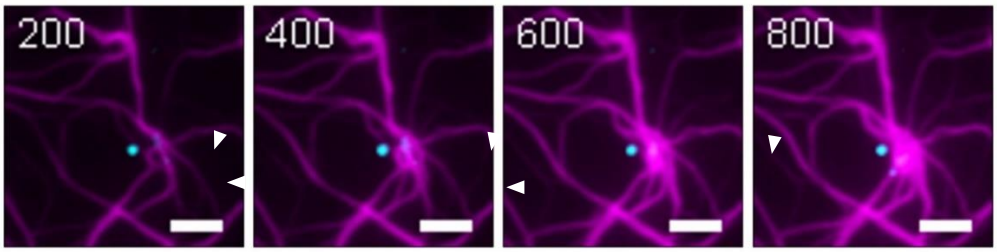

Figure 5.7: Localization of NMMII motors by fluorescent labeling and temporal development. Here, a 10% fraction of Atto-647N fluorescently labeled NMMII is added to an actin network anchored to a SLB and bundled by VASP. NMMII filaments (cyan) bound to actin (purple) are marked by white arrows. The activity of NMMII moving along the network precedes the initiation of a cluster. The intra-bundle rearrangement leads to several freshly nucleated filaments oriented pointing away from the cluster, likely due to the stress-induced rupturing activity of myosin that has been reported previously[8,100]. Additionally, the cluster swells as monomers get incorporated. This leads to the hypothesis that stresses induced by the activity of NMMII cause the formation of free barbed ends. The time scale shown is in seconds, scale bars = 3 µm.

To confirm that the motor activity is indeed responsible for the occurrence of cluster growth, Atto-647N fluorescently labeled motors were used and indeed found to colocalize with bundles that developed into clusters (Figure 5.7). The swelling of the cluster was rather heterogeneous; however, clusters grew generally much wider as compared to the bundles formed by VASP in the absence of NMMII (Figure 5.8a) suggesting that the expansion of these clusters is primed by the intra-bundle contractions mediated by NMMII. Moreover, the clusters nucleated novel filaments and bundles that are elongated in an orientation facing away from the cluster. To illustrate nucleation, a yellow line is drawn to analyze the directionality of filaments growing along the line (Figure 5.8b). A kymograph (Figure 5.8c) corresponding to the yellow line depicts how filaments grow away from the cluster, while filaments elongating towards the opposite direction could not be observed. Dashed, yellow lines are drawn for each new filament to better visualize each observable elongation event. The growth mechanisms were evaluated by analyzing the actin flow using an optical flow algorithm on fluorescence images, both in absence of NMMII (Figure 5.8d)

and presence of NMMII (Figure 5.8e). When only VASP was present, elongating filaments grew along the tracks formed by previously formed bundles as visualized by the vectors in the flow field that are predominantly orientated along the bundles of the network. By contrast, in presence of NMMII, the clusters formed by expansion which is shown by vector orientations pointing away from the direction of the bundle. This is also represented by plotting the absolute value of the scalar product between the flow and the bundle direction vectors (Figure 5.8f). The correlation shows how the orientation of the vectors is much less aligned in the cluster-swelling network type.

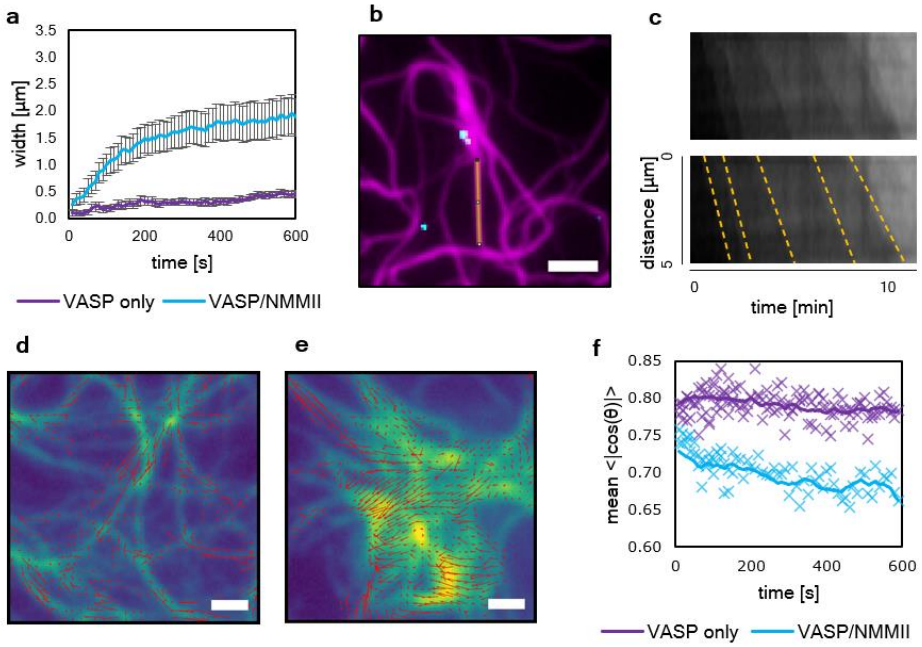

Figure 5.8: Quantification and correlation of motor localization and the emergence of clusters. **a** The width of arbitrarily chosen bundles and clusters over time. On average, in the presence of NMMII bundles grew much wider (up to 2 µm in width). The increase in width without NMMII depends on the barbed-end elongation of filaments and thus occurs on a much slower time scale. At least 10 individual bundles or clusters were measured. **b** A fraction of 20% labeled NMMII (cyan) was used to visualize the localization of the motor in the network. Where motors were present, clusters slowly appeared in the network, which indicated a strong correlation between the motor activity and the emergence of actin clusters. A line is drawn at one of the bundles emerging from a cluster with labeled active motors to identify the directionality of filaments growing along the bundle. Scale bars = 3 µm. **c** A Kymograph analysis. The bottom kymograph has dashed, yellow lines to better visualize individual filaments growing alongside the cluster. Here, it is shown that the bundles emerging from the clusters display directional growth. Most filaments that grew on the bundles emerging from clusters were elongated away from the cluster but not towards the cluster. **d** A flow analysis of the network growth with VASP and actin only reveals that actin is polymerized mostly alongside bundles as indicated by the actin flow vectors (red). Both growth directions alongside each bundle are equally represented, indicating that bundles are composed of random arrays of actin filament. **e** A flow analysis in the presence of NMMII reveals how clusters are formed in a swelling manner, growing from the inside towards the outside of the cluster. **f** The

mean absolute value <|cos(Θ)|> of the cosine of the angle Θ between the local actin's flow and the local bundle orientation shows how uniformly the vectors are distributed in both cases. For a random collection of angles, the expected value is 2/π ~ 0.64, while 1 would represent a network where all vectors point towards the same direction. In the presence of only VASP, the alignment between bundles and actin flow is relatively high (0.8) due to the growth of filaments alongside previously formed bundles. In the presence of VASP and NMMII, the mean angle is initially very close (0.75) but slowly decays (0.65 after 10 min) due to the altered growth mechanism by cluster swelling.

5.5 Intra-bundle contractions alter the cortex growth mechanism

To corroborate that VASP networks in the presence of NMMII are polymerized by an altered growth mechanism, a second pool of monomers with a different color was added to growing networks both in the absence (Figure 5.9a) and presence of NMMII (Figure 5.9b).

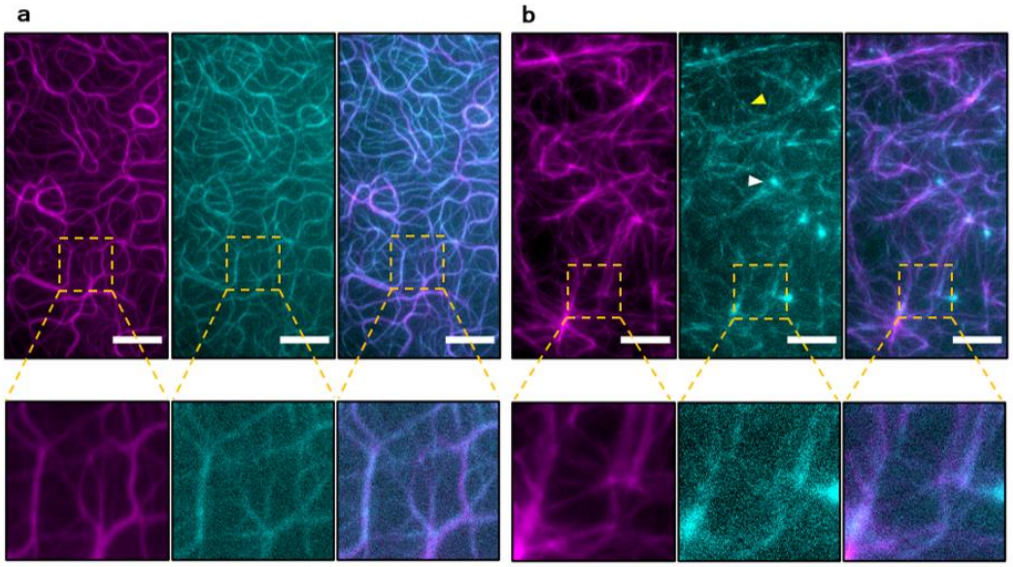

Figure 5.9: Addition of differently labeled to identify the difference in growth mechanism between networks without and with NMMII. **a** First, actin containing a 10% fraction of Atto 488-labeled monomers (magenta) was pre-polymerized for 20 min on a VASP functionalized supported lipid bilayer (left image). Then, an additional 10% fraction of Atto 647N-labeled monomers (cyan) was added to the polymerization mixture and allowed to be incorporated for 10 more minutes (middle image). The right image depicts an overlay of both channels. The filament elongation could be observed along the previously formed bundles. **b** Actin containing 488-labeled actin was pre-polymerized as before but with NMMII in solution (left). The second color (middle) is incorporated at previously formed clusters and alongside previously formed bundles, however much less uniformly compared to the network without NMMII. This leads to individual spots and dashed lines appearing in the second color indicating that monomers are incorporated preferentially on filament-barbed ends created by rupturing within the network due to intra-bundled stresses. An example of this type of incorporation is shown by a yellow arrow. Additionally, new clusters formed in regions where no clusters have

been pre-polymerized. An example for one of those clusters is marked with a white arrow. This is visualized best in an overlay of both images (right). Scale bars = 10 µm.

The networks were polymerized for 20 min with a 10% fraction of fluorescently labeled monomers and the resulting networks are shown in purple. Then, a second 10% fraction of monomers labeled with a different fluorescent label was added. The second color is shown in cyan after 10 min of incorporation. In the presence of NMMII, the incorporation of monomers occurred over a wider area and was mostly pronounced around clusters. Alongside bundles, the incorporation of monomers was inhomogeneous, much in contrast to the networks without NMMII. Not only the swelling of previous clusters could be observed, but also the formation of new clusters. This evidence allowed for the postulation of an altered growth mechanism, specifically tied to the occurrence of intra-bundle contractions mediated by NMMII (Figure 5.10). Intra-bundle contractions create stress in the bundle, leading to nicking of individual filaments along the bundle, in contrast to skeletal muscle myosin II which is able to rupture bundles completely[8,100]. Monomers bind novel filament barbed ends and can either lead to reannealing and thus swelling of the cluster, or elongation of new filaments, leading to bundles elongating away from the cluster.

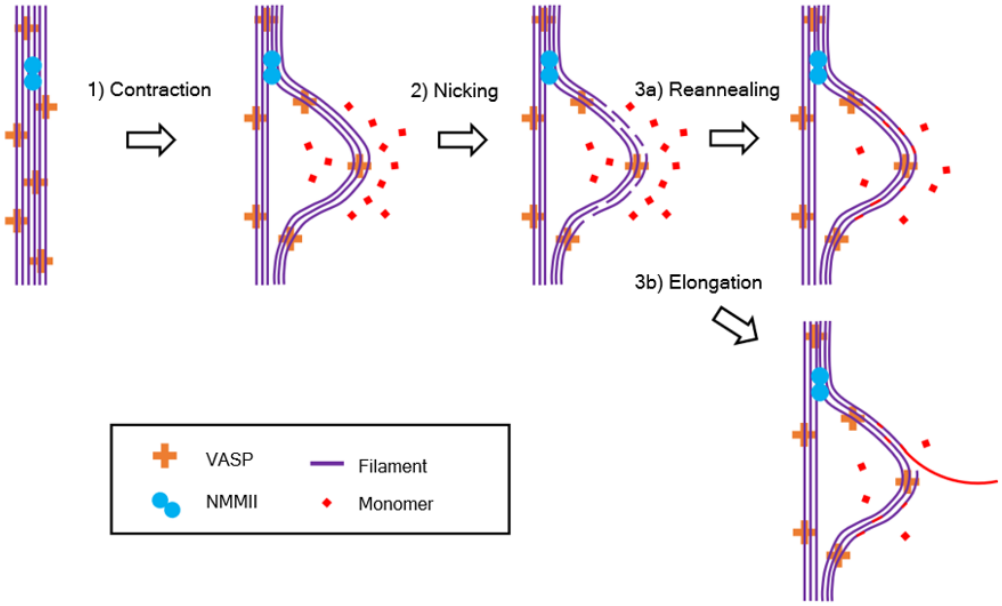

Figure 5.10: Network growth mechanism by cluster expansion. Mechanism explaining the altered growth mechanism in networks containing NMMII. Due to the transient crosslinking by the lipid anchored VASP (orange crosses), individual filaments (magenta lines) can be pulled along each other by NMMII (cyan circles), resulting in intra-bundle contractions. Stress built up by the contraction can lead to severing of individual filaments, which either creates barbed ends that can elongate away from the complex,

or reannealing of the ends while incorporating free monomers (red dots). The latter mechanism explains the cluster swelling growth that has been observed in these networks.

As a proof of concept, fascin was added to replace VASP. Fascin is able to crosslink bundles and should therefore prevent contractions on an intra-bundle level[29]. Indeed, no swelling of clusters and no intra-bundle contraction could be observed when bundles were cross-linked by fascin (Figure 5.11a-d).

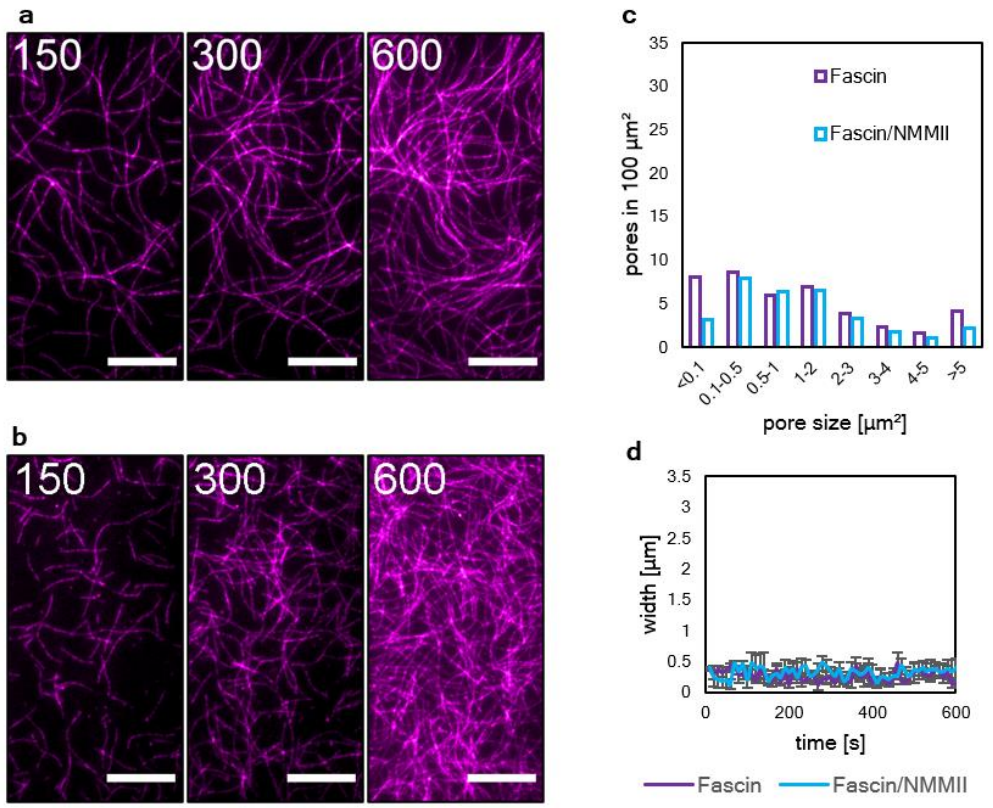

Figure 5.11: Intra-bundle contractions are inhibited in actin networks cross-linked by fascin. Fascin is known to form stable bundles and is associated with crosslinking of parallel actin filaments in stress fibers[90]. Here, 500 nM fascin is used to crosslink actin on a SLB both **a** in the absence and **b** in the presence of NMMII. The bundles formed in the absence of NMMII appear generally longer, which is best seen at the early stages of polymerization after 150 s of the initiation of the experiment. However, no contractions can be observed and the architecture of the network is the same when NMMII is present. No formation of clusters occurs, which emphasizes the causality of the intra-bundle contraction and cluster swelling. The depicted time scale is in seconds, scale bars = 10 µm. The network architecture is quantified by analyzing **c** the pore sizes of the network at 10 minutes after initiation the experiment and **d** the width of bundles over time. In both the histogram and the temporal development of the bundle width, no significant difference between the networks can be observed.

5.6 Discussion

This chapter describes a growth mechanism of active actin networks based on the contraction of filaments on an intra-bundle level by NMMII, which stands in

strong contrast to contractions mediated by skeletal muscle myosin II. Contractions by skeletal muscle myosin II are much faster and reach across multiple bundles (Figure 5.12), leading to well described, globally contractile networks[97,101-104].

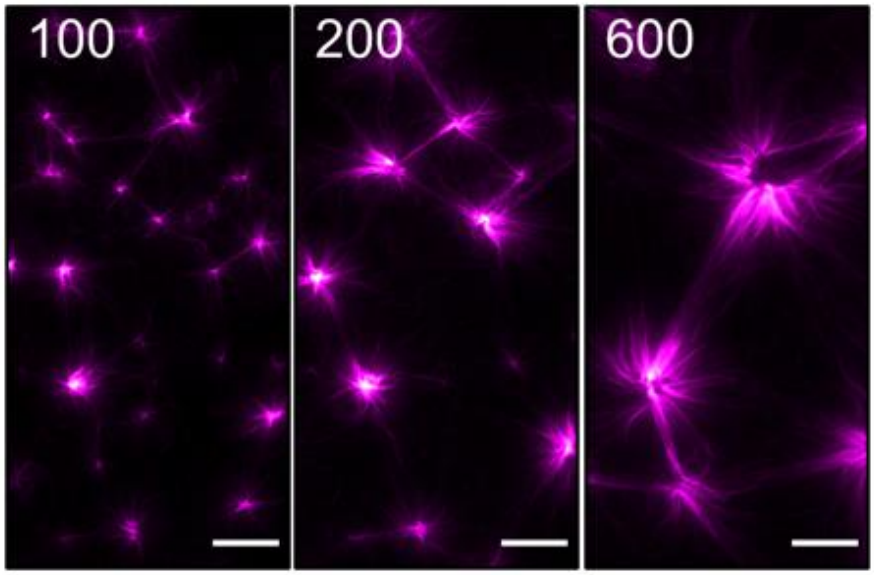

Figure 5.12: Skeletal muscle Myosin II contracts along bundles in actin networks anchored by VASP. Instead of 200 nM NMMII, 200 nM skeletal muscle myosin II is used. In contrast to the small, local contractions of NMMII, skeletal muscle myosin II is able to contract across multiple bundles and pull filaments towards the centers of clusters with a visible center. Although networks with both types of myosin II are highly dynamic, here the dynamics lead to the well described state that can be observed in similar networks with different nucleators[105]. The contractions on inter-bundle level are likely possible due to the larger filaments formed by skeletal muscle myosin II[36,106]. The depicted time scale is in seconds, scale bars = 10 µm.

Yet, expansions should be possible and have long been predicted to exist theoretically[107]. The difficulty of the experimental realization of these networks is the dependence on many different factors that are hard to control in reconstitution experiments, but can easily be varied in simulations[108]. The crucial difference in the presented system compared to the well described, globally contractile systems is the choice of motor, but also the lateral unrestricted bundling by methylcellulose or VASP. Only in the system described here, splitting of bundles is possible due to the fluidity of the SLB as opposed to anchoring towards a solid substrate that would stabilize the bundles. This exceeds previous reconstructions of actin cortices by displaying a new functionality of actin networks in vivo. Split bundles prime clusters and lead to stress and fluctuations that allow for the incorporation of monomers on a wide surface area through the formation of free ends. These barbed ends can be easily tracked in the presented experiments due to the high resolution of TIRF

microscopy (Figure 5.13). While networks without NMMII elongate predominantly along previously formed actin filaments, NMMII primes and extends clusters by a mechanism of extension, nicking and repair. This effectively leads to a swelling of actin clusters that can also produce extensions by elongation of individual, nicked filaments in the bundles.

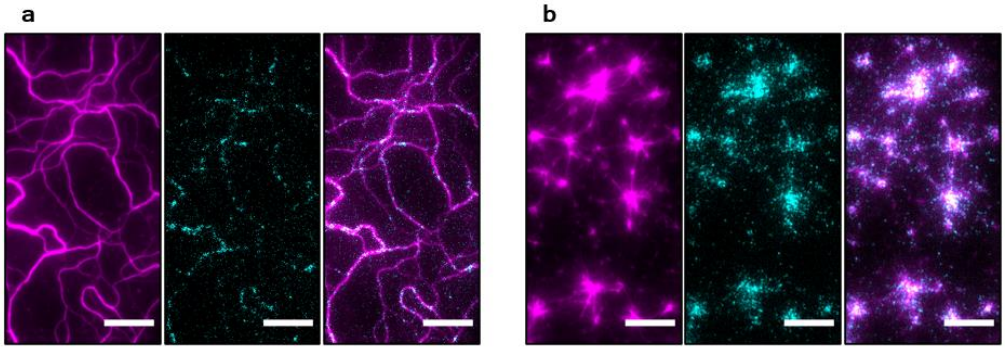

Figure 5.13: Tracking of barbed ends by addition of labeled capping protein as marker. Capping protein is labeled via an Atto488N NHS-ester. Here, actin labeled by an Atto532 NHS-ester is shown in purple and labeled capping protein is shown in cyan. 50 nM capping protein is added to a network anchored to a SLB and bundled by VASP **a** in the absence and **b** in the presence of NMMII 10 minutes after the initiation of the network polymerization. When no NMMII is present, the barbed ends marked by capping protein are distributed alongside the bundles relatively homogeneously. Cluster swelling can be observed only in the network containing NMMII. The localization of the barbed ends as indicated by the presence of labeled capping protein is pronounced at the cluster, especially at the centers of the clusters. This is in agreement with the model of cluster swelling, as barbed ends are created by the myosin-induced stresses. The network architecture is slightly altered in the presence of capping protein. This is most likely due to shorter filaments, as long bundles connecting all the clusters don't form as compared to similar networks in the presence of VASP and NMMII shown for example in figure 2. Scale bars = 10 µm.

For biomimetic reconstitution experiments, due to their physiological role, Arp2/3 and formins such as mDia1 are a more common choice as membrane associated nucleator[109-113]. Although VASP elongates filaments similarly to formins[92,114], striking differences like profilin-independent recruitment of actin monomers have been reported[115]. A crucial difference is also the role of VASP in the formation of filopodia[116], microspikes[94] and cell motility[117], where different modes of action have been reported: Enduring processive elongation while surface bound and short lived non-processive elongation and bundling while in solution[99]. *In vivo*, a direct colocalization of VASP and myosin cannot typically be observed[118]. However, they are likely to interact through force transmitted by myosin via the cortical actin network and in focal adhesions connected by stress fibers[119]. The interplay of VASP, actin and NMMII reported here might very well contribute to the explanation of various cortical functions, as this system alone can account for some of the challenging requirements of lamellipodium based

motility or force development in the adhesion system: Contractility, stability, actin turnover and symmetry breaking, in this case by a novel mechanism of cluster swelling.

This extends our current understanding of dynamics in active actomyosin cortices. Although previous work has demonstrated high dynamics[120,121] or strong contractility[105] in reconstituted active actomyosin cortices, the system presented here establishes an important bridge between the two extremes. Ultimately, these findings can explain the molecular basis of how active actin cortices break symmetry to initiate polarized cell motility[122] or even generate stress fibers[123] within highly dynamic lamellipodia by means of NMMII-mediated actin reorganization.

6. Conclusion and Outlook

This thesis provides an experimental framework for the reconstitution of global actin turnover and concludes several molecular principles from quantifying and analyzing the dynamics underlying these networks. Together, the presented findings contribute to the progression of several related branches of scientific research:

1. Molecular mechanisms were identified which contribute to our understanding of related processes in vivo. One example for one of those processes is the formation of stress fibers. The cellular cortex is initially a disordered, yet order can emerge for example by crosslinking bundles into highly ordered, parallel bundles resulting in a stiffened network[124–126]. Detailed models of how the cortex can break its symmetry are however rarely discussed[127,128]. The presented mechanism can explain how a symmetry-break can occur by expansion of clusters and can be discussed just as well in the context of cells.
2. In vitro reconstitutions of artificial cells were limited by the lacking ability of recreating actin turnover until now. Due to this limitation, cytoskeletal vesicles were not able to produce protrusions or active shape changes, mimicking cell motility or processes like the formation filopodia[32,110,129–133]. Without a recycling mechanism for monomer recovery only a single round of polymerization can be reconstituted, thus a static network forms, especially when nucleators like Arp2/3 or formin are used which deplete the monomer pool fast. The system presented in this thesis provides the ability of maintained actin turnover, effectively allowing a continuous polymerization at the membranes while ATP is available.
3. The existence of expansile networks have been predicted in silico. Here, an experimental framework has been presented to support the theoretical predictions. Conversely, the models described here can also be challenged by computational models. The concept of protein depletion by actin binding suggests also its implementation in future simulations of cytoskeletal processes.

With these insights, it is possible to produce motile artificial cells by combining the active cytoskeletal turnover with the ability to break the symmetry of the cortex. Motility could for example be achieved by placing the cytoskeletal vesicles in microfluidics channels. In a channel, vesicles are expected to actively crawl to compensate for the forces maintained by the actin treadmilling which are explained by Brownian ratchet models[134].

Another possibility already tested in this thesis is the encapsulation in phase separating vesicle. However, the turnover has shown to mix the phases. This is an interesting observation and is in agreement with the consequences of an active turnover, however makes it impossible to mimic the phase-separation as observed in lipid rafts in vivo[135,136]. Another idea was to embed treadmilling vesicles within an outside actin network stabilized by a crosslinker (Figure 6.1).

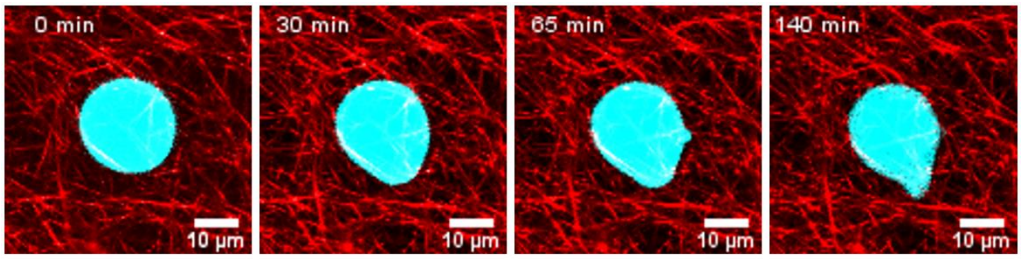

Figure 6.1: Embedding a vesicle with globally treadmilling actin in a fascin network. A treadmilling vesicle containing encapsulated, treadmilling actin (cyan). The turnover is directed to the membrane by formin. The vesicle is embedded in a stable actin-fascin network (red). The osmolarity of the outside solution is 40 mOsm higher to create excess membrane and produce floppy, deformable vesicles. Deformations of the vesicles can be observed as it tries to move through the mesh created by the actin-fascin network. However, the pore size of the mesh seems to be too small for the vesicle to pass through.

The vesicle actively deformed and expanded multiple blebs to reach through pores, however the mesh size was too small for the vesicle to fit through. Ideally, a more suitable outside network such as collagen should be used to represent the extracellular matrix. Yet, this experiment demonstrates how studies could be designed in the future to achieve the long-standing goal of artificial motile cells.

Appendix

A1 MST binding curves

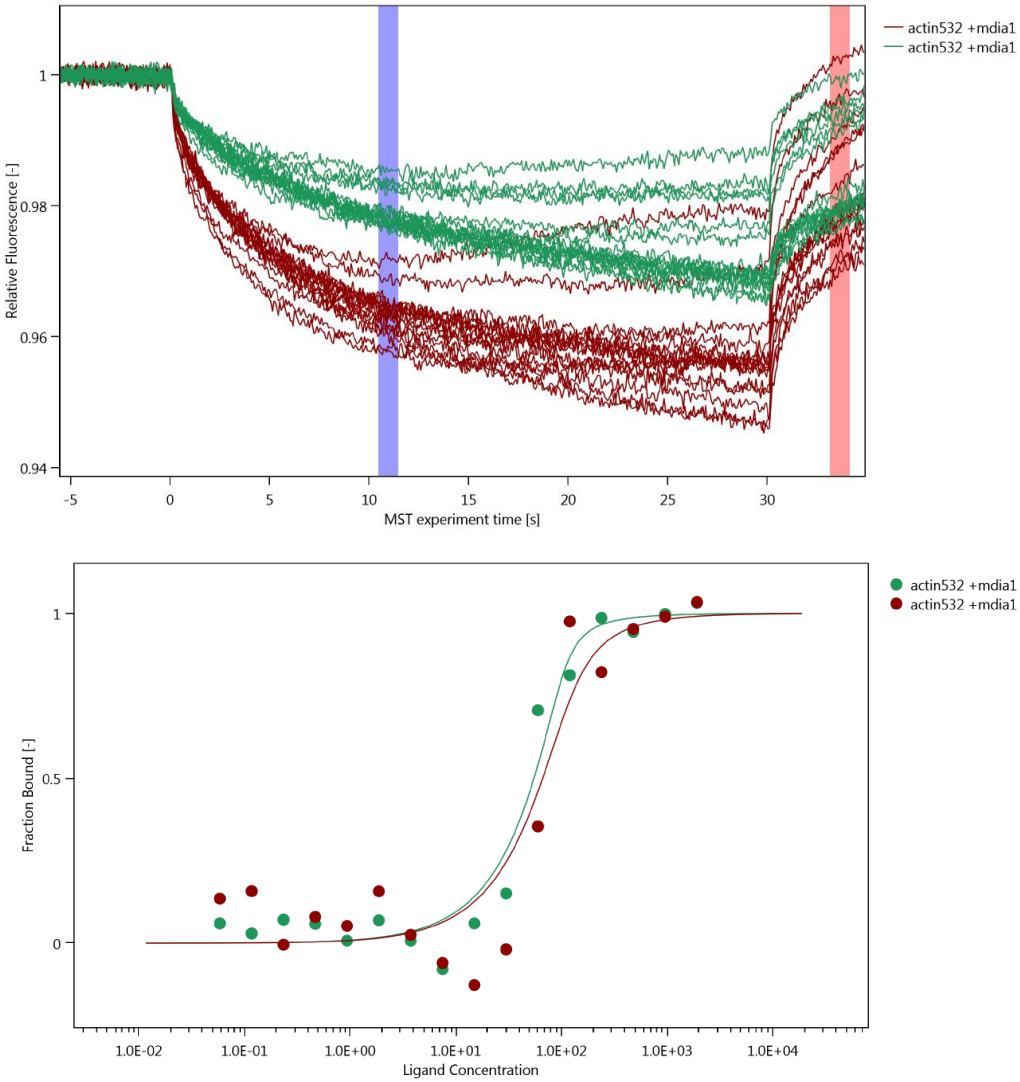

Figure A.1: MST traces and binding curve of mDia1 ligand (formin) on G-ATP-actin532 fluorophore.

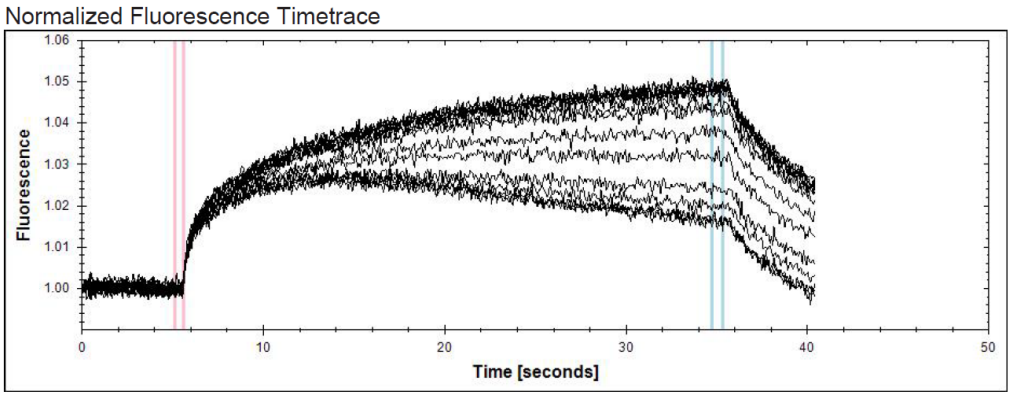

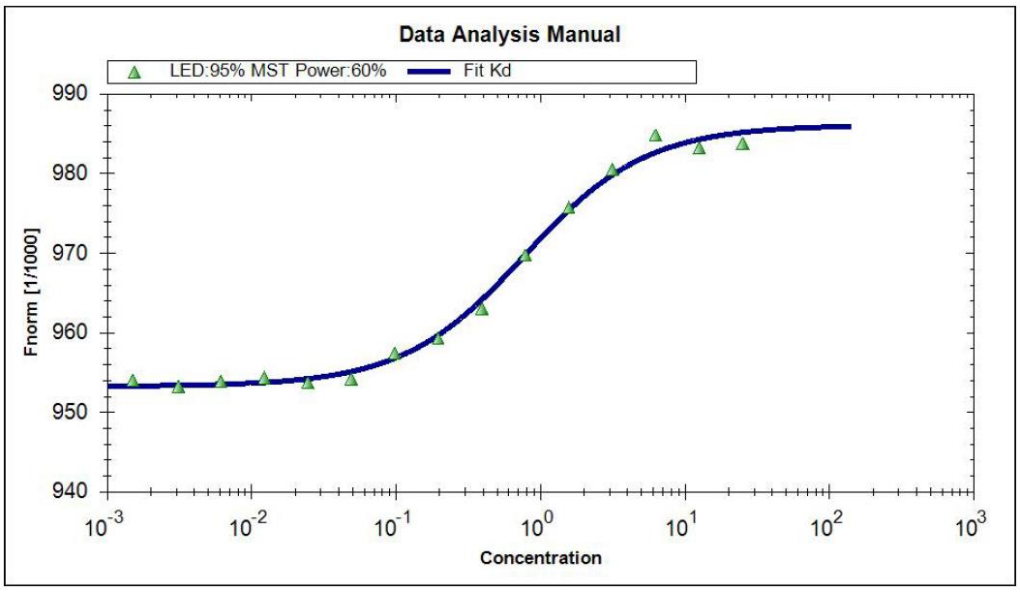

Figure A.2: MST traces and binding curve of profilin ligand on G-ATP-actin488 fluorophore.

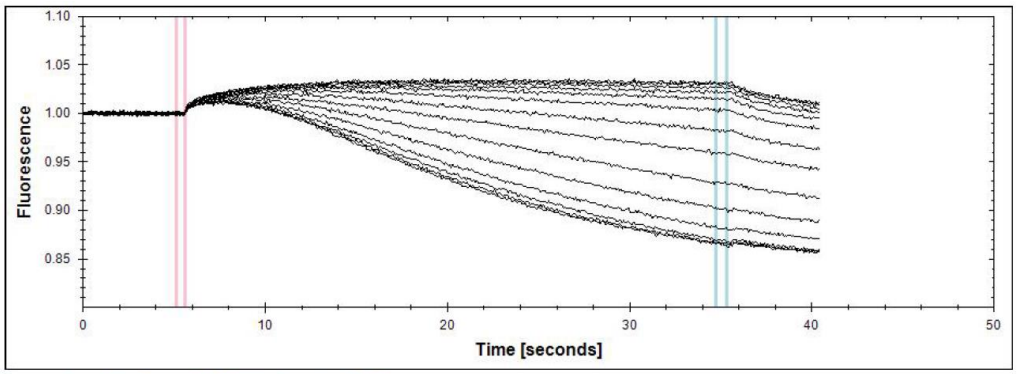

hot region: HotStart=34.73 HotLength=0.60
cold region ColdStart=5.10 ColdLength=0.48

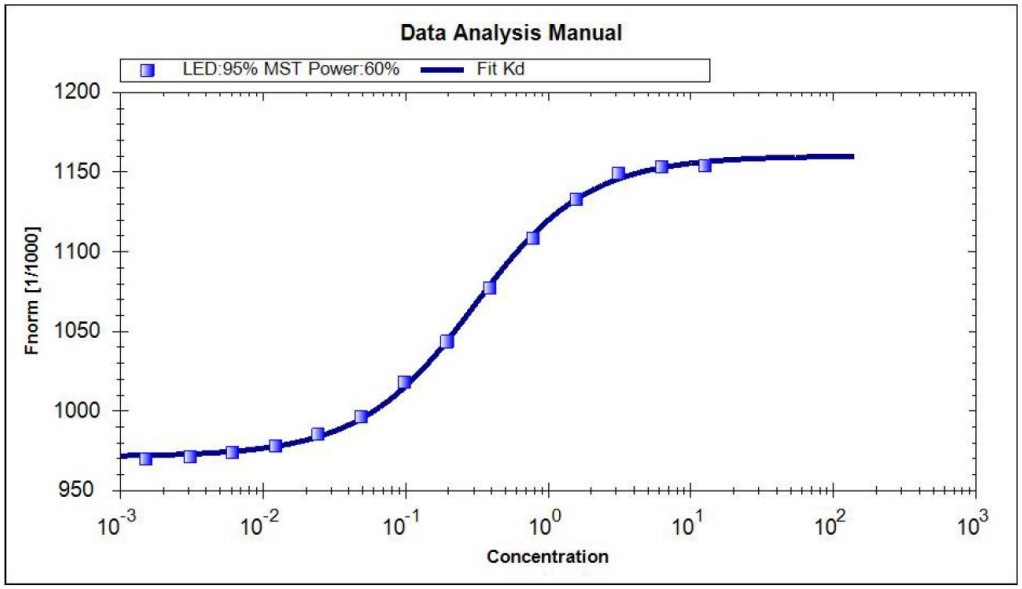

Figure A.3: MST traces and binding curve of profilin ligand on F-actin488 fluorophore.

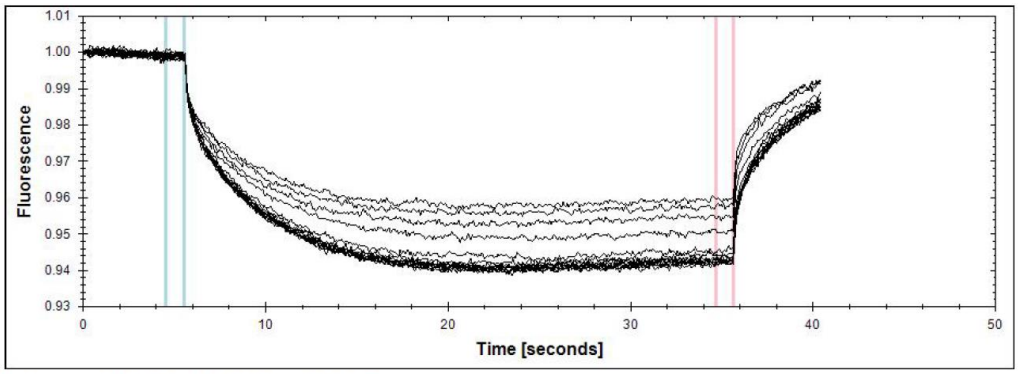

hot region: HotStart=4.55 HotLength=0.97
cold region ColdStart=34.65 ColdLength=0.97

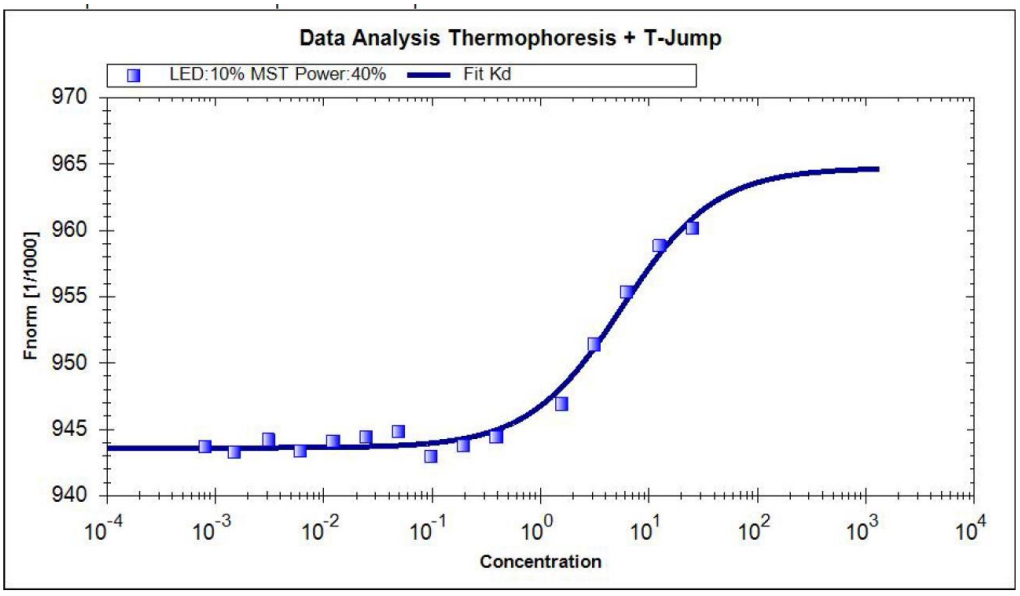

Figure A.4: MST traces and binding curve of cofilin ligand on G-ATP-actin647N fluorophore.

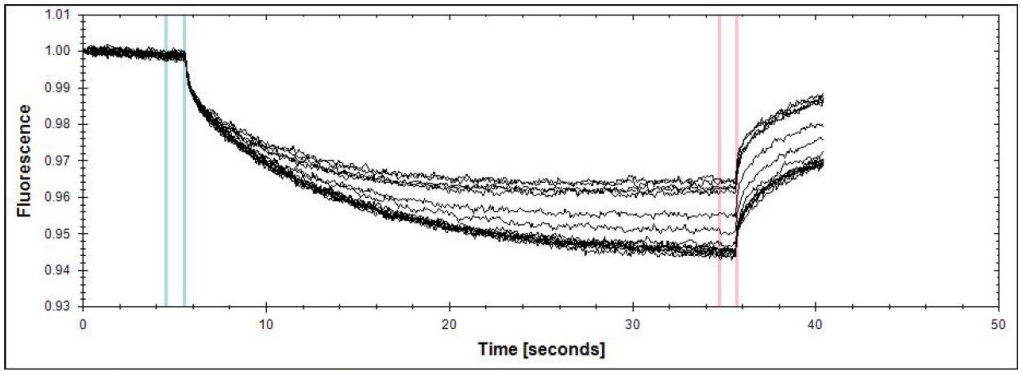

hot region: HotStart=4.55 HotLength=0.97
cold region ColdStart=34.72 ColdLength=0.97

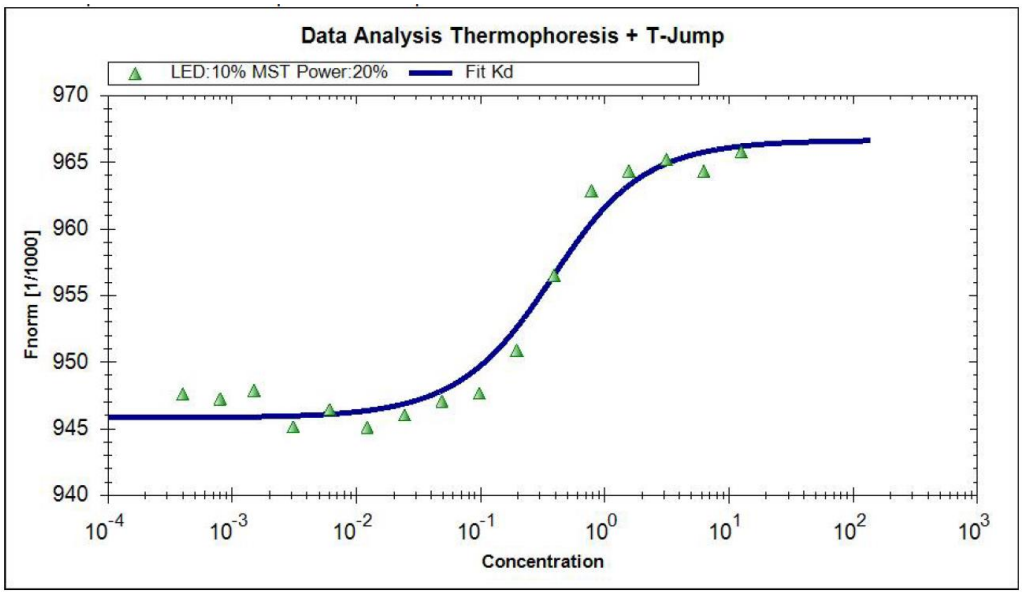

Figure A.5: MST traces and binding curve of cofilin ligand on G-ADP-actin647N fluorophore.

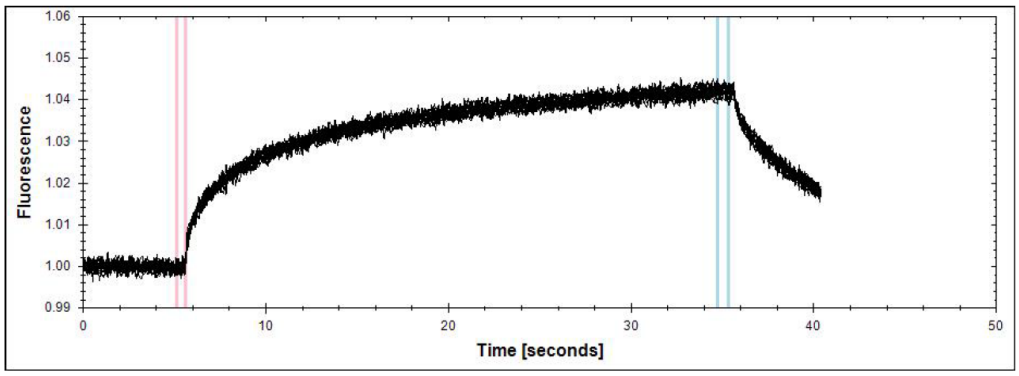

hot region: HotStart=34.73 HotLength=0.60
cold region ColdStart=5.10 ColdLength=0.48

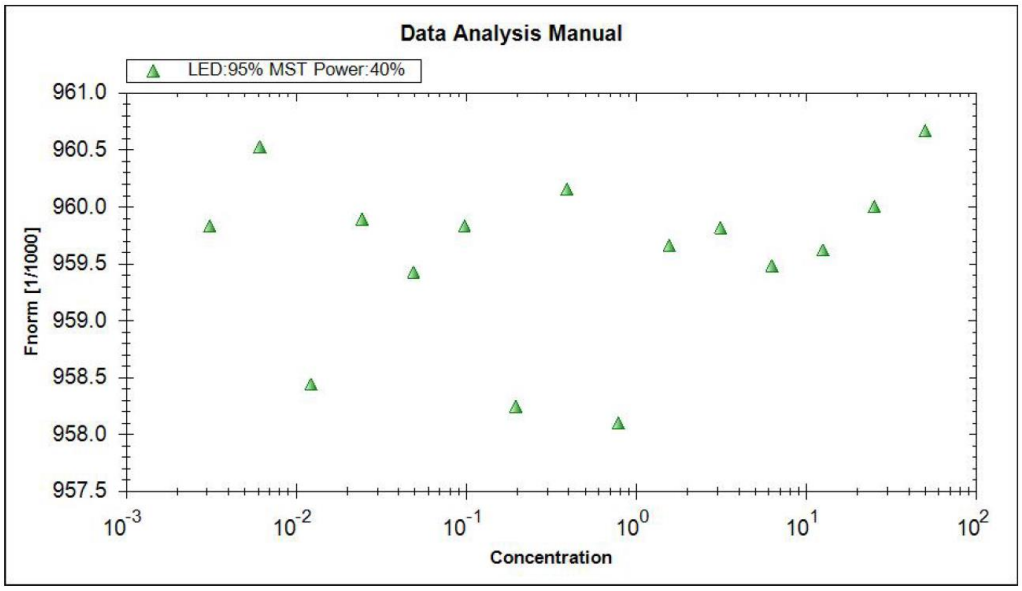

Figure A.6: MST traces and binding curve of BSA ligand on G-ATP-actin488 fluorophore.

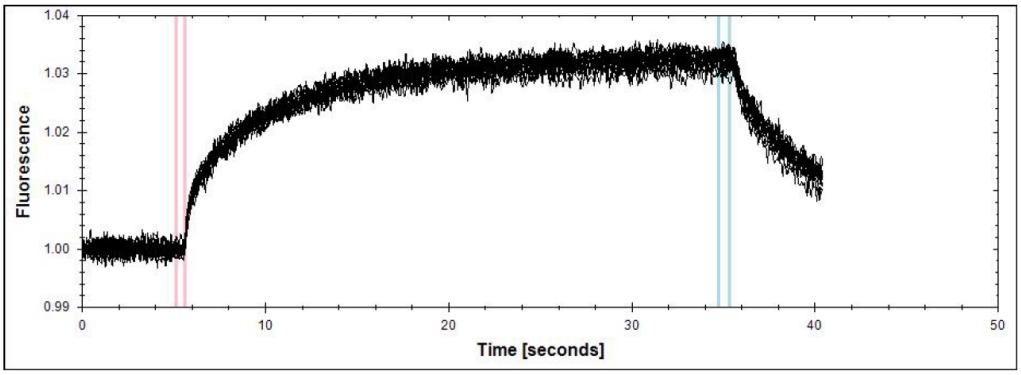

hot region: HotStart=34.73 HotLength=0.60
cold region ColdStart=5.10 ColdLength=0.48

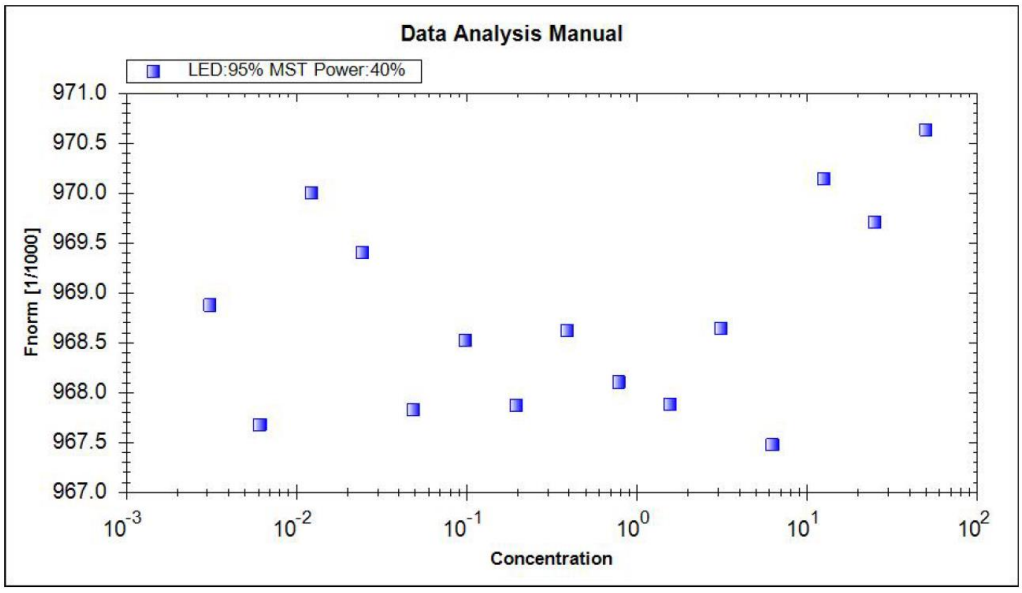

Figure A.7: MST traces and binding curve of BSA ligand on F-actin488 fluorophore.

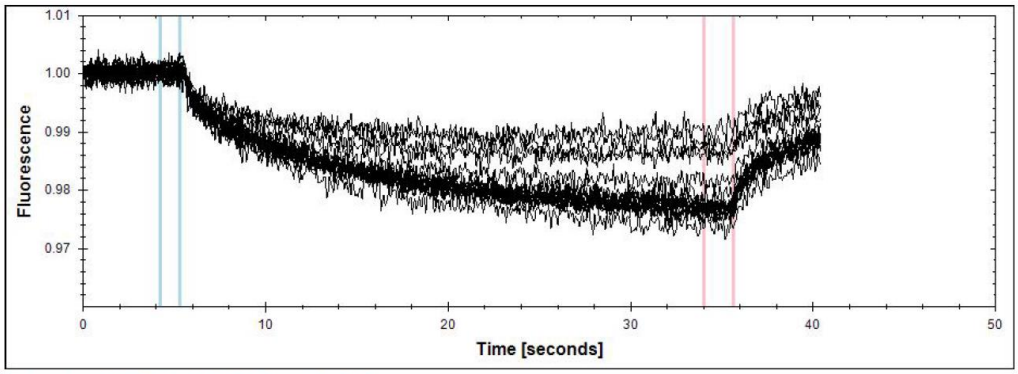

hot region: HotStart=4.25 HotLength=1.05
cold region ColdStart=34.01 ColdLength=1.61

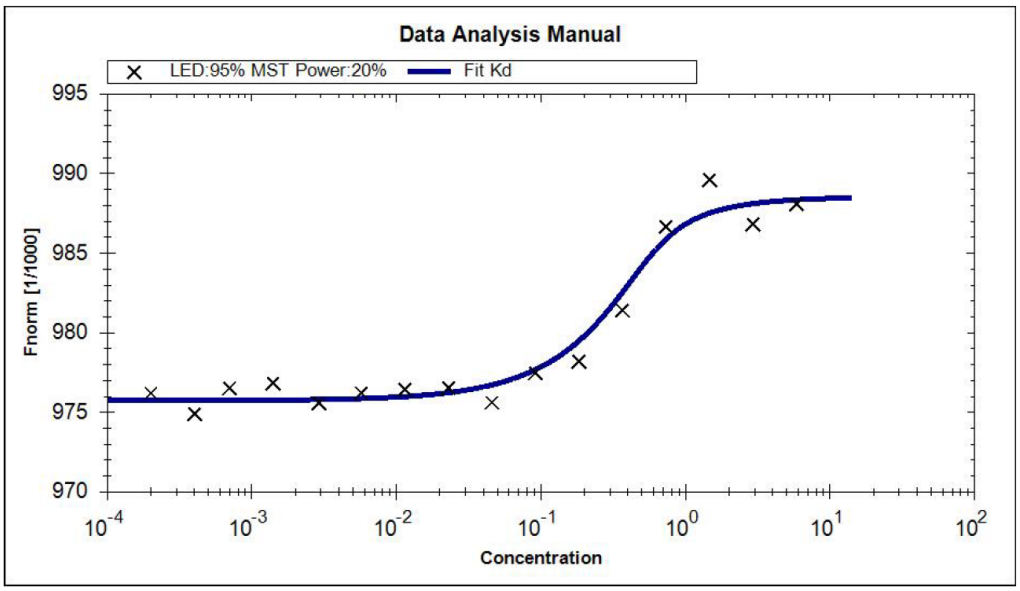

Figure A.8: MST traces and binding curve of ADP-actin ligand on mCherry-hCof fluorophore in the presence of CAP1.

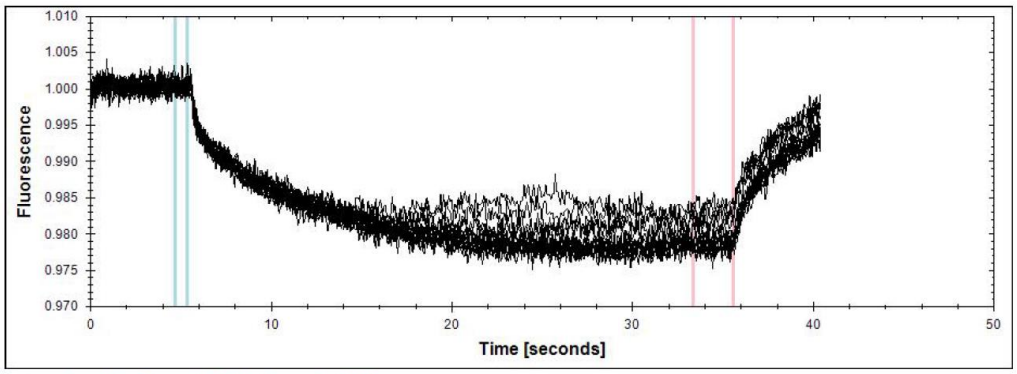

hot region: HotStart=4.69 HotLength=0.66
cold region ColdStart=33.36 ColdLength=2.19

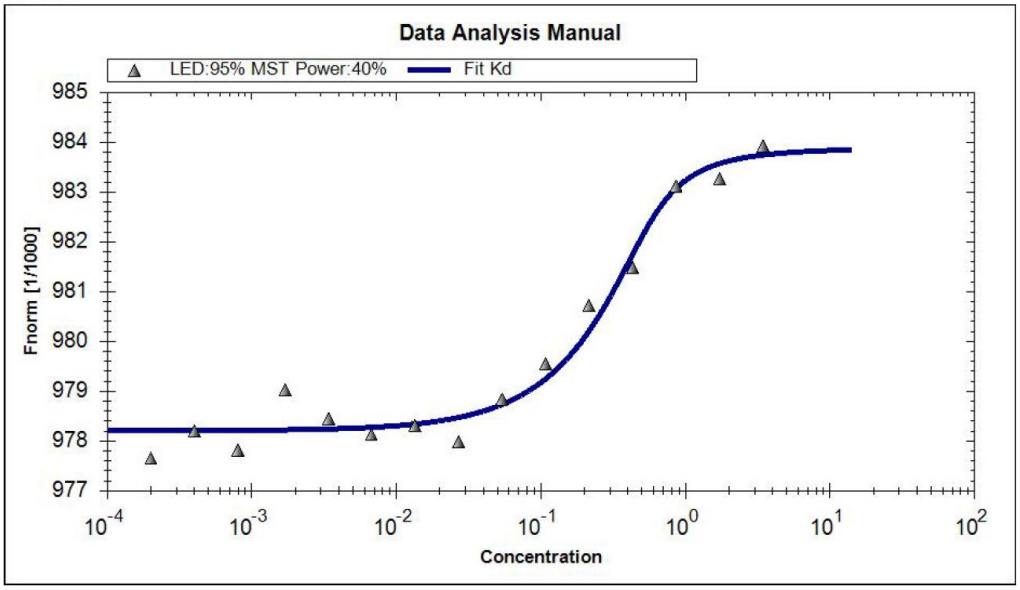

Figure A.9: MST traces and binding curve of CAP1 ligand on mCherry-hCof fluorophore in the presence of ADP-actin.

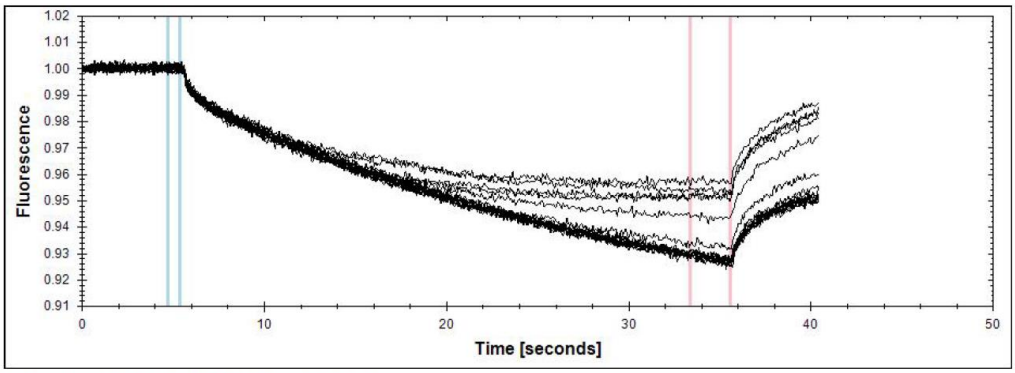

hot region: HotStart=4.69 HotLength=0.66
cold region ColdStart=33.36 ColdLength=2.19

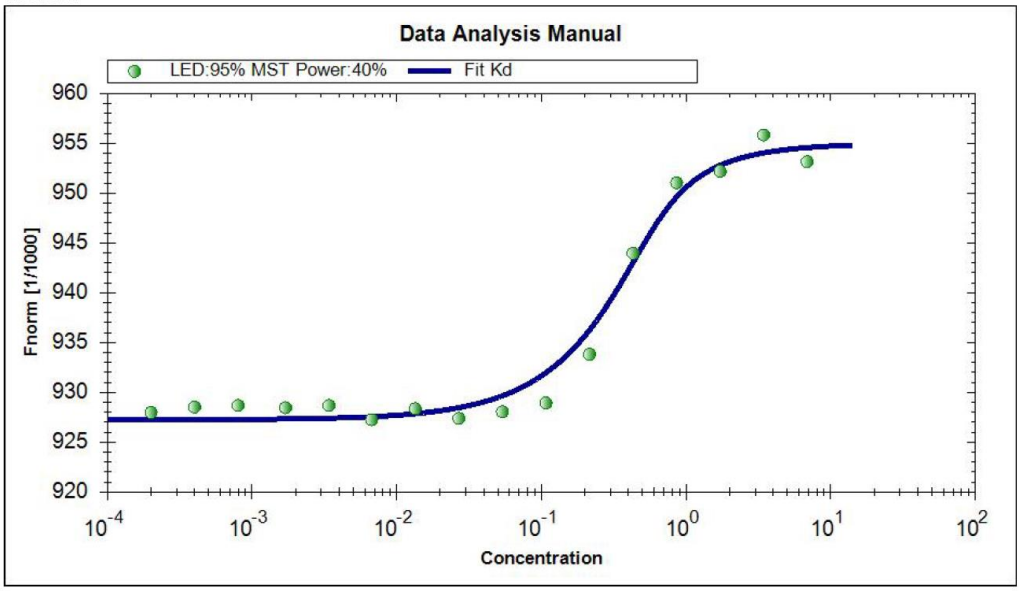

Figure A.10: MST traces and binding curve of CAP1 ligand on mCherry-hCof fluorophore.

A2 Full List of Publications

Authors	**Philip Bleicher**, Timon Nast-Kolb, Alfredo Sciortino , Yu Alice de la Trobe, Thomas Pokrant, Jan Faix & Andreas R. Bausch
Title	Intra-bundle contractions enable extensile properties of active actin networks
Journal	N/A (submitted to Scientific Reports)
Year	N/A (submitted 2020)

Authors	**Philip Bleicher**, Alfredo Sciortino & Andreas R. Bausch
Title	The dynamics of actin network turnover is self-organized by a growth-depletion feedback
Journal	Scientific Reports
Year	2020

Authors	Katharina Dürre, Felix C. Keber, **Philip Bleicher**, Fridtjof Brauns, Christian J. Cyron, Jan Faix & Andreas R. Bausch
Title	Capping protein-controlled actin polymerization shapes lipid membranes
Journal	Nature Communications
Year	2018

Authors	Katrin Franz-Oberdorf, Bernadette Eberlein, Kathrin Edelmann, **Philip Bleicher**, Elisabeth Kurze, Dominic Helm, Klaus Olbrich, Ulf Darsow, Johannes Ring & Wilfried Schwab
Title	White-fruited strawberry genotypes are not per se hypoallergenic
Journal	Food Research International 100
Year	2017

A3 List of figures

Appendix

A4 List of Tables

References

1. Lazarides, E. & Weber, K. Actin antibody: the specific visualization of actin filaments in non muscle cells. *Proc. Natl. Acad. Sci. U. S. A.* (1974) doi:10.1073/pnas.71.6.2268.

2. Melak, M., Plessner, M. & Grosse, R. Actin visualization at a glance. *J. Cell Sci.* (2017) doi:10.1242/jcs.189068.

3. Spracklen, A. J., Fagan, T. N., Lovander, K. E. & Tootle, T. L. The pros and cons of common actin labeling tools for visualizing actin dynamics during Drosophila oogenesis. *Dev. Biol.* (2014) doi:10.1016/j.ydbio.2014.06.022.

4. Huehn, A. *et al.* The actin filament twist changes abruptly at boundaries between bare and cofilin-decorated segments. *J. Biol. Chem.* (2018) doi:10.1074/jbc.AC118.001843.

5. de la Cruz, E. M. How cofilin severs an actin filament. *Biophysical Reviews* (2009) doi:10.1007/s12551-009-0008-5.

6. McCullough, B. R., Blanchoin, L., Martiel, J. L. & De La Cruz, E. M. Cofilin Increases the Bending Flexibility of Actin Filaments: Implications for Severing and Cell Mechanics. *J. Mol. Biol.* (2008) doi:10.1016/j.jmb.2008.05.055.

7. Suarez, C. *et al.* Cofilin tunes the nucleotide state of actin filaments and severs at bare and decorated segment boundaries. *Curr. Biol.* (2011) doi:10.1016/j.cub.2011.03.064.

8. Schmoller, K. M., Semmrich, C. & Bausch, A. R. Slow down of actin depolymerization by cross-linking molecules. *J. Struct. Biol.* (2011) doi:10.1016/j.jsb.2010.09.003.

9. Carlier, M. F. *et al.* Actin depolymerizing factor (ADF/cofilin) enhances the rate of filament turnover: Implication in actin-based motility. *J. Cell Biol.* (1997) doi:10.1083/jcb.136.6.1307.

10. Shekhar, S. & Carlier, M.-F. Enhanced Depolymerization of Actin Filaments by ADF/Cofilin and Monomer Funneling by Capping Protein Cooperate to Accelerate Barbed-End Growth. *Curr. Biol.* **27**, 1990-1998.e5 (2017).

11. Carlier, M. F. & Shekhar, S. Global treadmilling coordinates actin

turnover and controls the size of actin networks. *Nature Reviews Molecular Cell Biology* (2017) doi:10.1038/nrm.2016.172.

12. Nishida, E. Opposite Effects of Cofilin and Profilin from Porcine Brain on Rate of Exchange of Actin-Bound Adenosine 5′-Triphosphate. *Biochemistry* (1985) doi:10.1021/bi00326a015.

13. Kotila, T. *et al.* Structural basis of actin monomer re-charging by cyclase-Associated protein. *Nat. Commun.* (2018) doi:10.1038/s41467-018-04231-7.

14. Moriyama, K. & Yahara, I. Human CAP1 is a key factor in the recycling of cofilin and actin for rapid actin turnover. *J. Cell Sci.* (2002).

15. Kotila, T. *et al.* Mechanism of synergistic actin filament pointed end depolymerization by cyclase-associated protein and cofilin. *Nat. Commun.* **10**, 5320 (2019).

16. Chugh, P. & Paluch, E. K. The actin cortex at a glance. *J. Cell Sci.* (2018) doi:10.1242/jcs.186254.

17. Biro, M. *et al.* Cell cortex composition and homeostasis resolved by integrating proteomics and quantitative imaging. *Cytoskeleton* (2013) doi:10.1002/cm.21142.

18. Kaji, N. *et al.* Cell cycle-associated changes in Slingshot phosphatase activity and roles in cytokinesis in animal cells. *J. Biol. Chem.* (2003) doi:10.1074/jbc.M305802200.

19. Chugh, P. *et al.* Actin cortex architecture regulates cell surface tension. *Nat. Cell Biol.* (2017) doi:10.1038/ncb3525.

20. Bovellan, M. *et al.* Cellular control of cortical actin nucleation. *Curr. Biol.* (2014) doi:10.1016/j.cub.2014.05.069.

21. Cao, L. *et al.* SPIN90 associates with mDia1 and the Arp2/3 complex to regulate cortical actin organization. *Nat. Cell Biol.* (2020) doi:10.1038/s41556-020-0531-y.

22. Castellano, F., Clainche, C. Le, Patin, D., Carlier, M. F. & Chavrier, P. A WASp-VASP complex regulates actin polymerization at the plasma membrane. *EMBO J.* (2001) doi:10.1093/emboj/20.20.5603.

23. Litschko, C. *et al.* Functional integrity of the contractile actin cortex is safeguarded by multiple Diaphanous-related formins. *Proc. Natl. Acad.*

Sci. U. S. A. (2019) doi:10.1073/pnas.1821638116.

24. Vavylonis, D., Kovar, D. R., O'Shaughnessy, B. & Pollard, T. D. Model of formin-associated actin filament elongation. *Mol. Cell* (2006) doi:10.1016/j.molcel.2006.01.016.

25. Amann, K. J. & Pollard, T. D. The Arp2/3 complex nucleates actin filament branches from the sides of pre-existing filaments. *Nat. Cell Biol.* (2001) doi:10.1038/35060104.

26. Winkelman, J. D., Bilancia, C. G., Peifer, M. & Kovar, D. R. Ena/VASP Enabled is a highly processive actin polymerase tailored to self-assemble parallel-bundled F-actin networks with Fascin. *Proc. Natl. Acad. Sci. U. S. A.* (2014) doi:10.1073/pnas.1322093111.

27. Harker, A. J. *et al.* Ena/VASP processive elongation is modulated by avidity on actin filaments bundled by the filopodia cross-linker fascin. *Mol. Biol. Cell* (2019) doi:10.1091/mbc.E18-08-0500.

28. Luo, T., Mohan, K., Iglesias, P. A. & Robinson, D. N. Molecular mechanisms of cellular mechanosensing. *Nat. Mater.* (2013) doi:10.1038/nmat3772.

29. Adams, J. C. Roles of fascin in cell adhesion and motility. *Current Opinion in Cell Biology* (2004) doi:10.1016/j.ceb.2004.07.009.

30. Winkelman, J. D. *et al.* Fascin- and α-Actinin-Bundled Networks Contain Intrinsic Structural Features that Drive Protein Sorting. *Curr. Biol.* (2016) doi:10.1016/j.cub.2016.07.080.

31. Paluch, E. K. & Raz, E. The role and regulation of blebs in cell migration. *Current Opinion in Cell Biology* (2013) doi:10.1016/j.ceb.2013.05.005.

32. Loiseau, E. *et al.* Shape remodeling and blebbing of active cytoskeletal vesicles. *Sci. Adv.* (2016) doi:10.1126/sciadv.1500465.

33. Henson, J. H. *et al.* The ultrastructural organization of actin and myosin II filaments in the contractile ring: New support for an old model of cytokinesis. *Mol. Biol. Cell* (2017) doi:10.1091/mbc.E16-06-0466.

34. Spudich, J. A. & Watt, S. The regulation of rabbit skeletal muscle contraction. I. Biochemical studies of the interaction of the tropomyosin-troponin complex with actin and the proteolytic fragments of myosin. *J.*

Biol. Chem. (1971).

35. Studier, F. W. Protein production by auto-induction in high density shaking cultures. *Protein Expr. Purif.* (2005).

36. Niederman, R. & Pollard, T. D. Human platelet myosin: II. In vitro assembly and structure of myosin filaments. *J. Cell Biol.* (1975) doi:10.1083/jcb.67.1.72.

37. Pollard, T. D. Purification of Nonmuscle Myosins. *Methods Enzymol.* (1982) doi:10.1016/0076-6879(82)85033-7.

38. Wienken, C. J., Baaske, P., Rothbauer, U., Braun, D. & Duhr, S. Protein-binding assays in biological liquids using microscale thermophoresis. *Nat. Commun.* (2010) doi:10.1038/ncomms1093.

39. Wang, Y. L. & Taylor, D. L. Exchange of 1,N6-etheno-ATP with actin-bound nucleotides as a tool for studying the steady state exchange of subunits in F-actin solutions. *Proc. Natl. Acad. Sci. U. S. A.* (1981) doi:10.1073/pnas.78.9.5503.

40. Veatch, S. L. & Keller, S. L. Separation of Liquid Phases in Giant Vesicles of Ternary Mixtures of Phospholipids and Cholesterol. *Biophys. J.* (2003) doi:10.1016/S0006-3495(03)74726-2.

41. Dürre, K. & Bausch, A. R. Formation of phase separated vesicles by double layer cDICE. *Soft Matter* (2019) doi:10.1039/c8sm02491j.

42. Shekhar, S. Microfluidics-Assisted TIRF Imaging to Study Single Actin Filament Dynamics. *Curr. Protoc. cell Biol.* (2017) doi:10.1002/cpcb.31.

43. Reymann, A. C. *et al.* Turnover of branched actin filament networks by stochastic fragmentation with ADF/cofilin. *Mol. Biol. Cell* (2011) doi:10.1091/mbc.E11-01-0052.

44. Mizuno, H., Tanaka, K., Yamashiro, S., Narita, A. & Watanabe, N. Helical rotation of the diaphanous-related formin mDia1 generates actin filaments resistant to cofilin. *Proc. Natl. Acad. Sci. U. S. A.* (2018) doi:10.1073/pnas.1803415115.

45. Boujemaa-Paterski, R. *et al.* Network heterogeneity regulates steering in actin-based motility. *Nat. Commun.* (2017) doi:10.1038/s41467-017-00455-1.

46. Blanchoin, L., Pollard, T. D. & Mullins, R. D. R. D. Interactions of

ADF/cofilin, Arp2/3 complex, capping protein and profilin in remodeling of branched actin filament networks. *Curr. Biol.* (2000) doi:10.1016/S0960-9822(00)00749-1.

47. Jansen, S. *et al.* Single-molecule imaging of a three-component ordered actin disassembly mechanism. *Nat. Commun.* (2015) doi:10.1038/ncomms8202.

48. Shekhar, S. & Carlier, M.-F. Single-filament kinetic studies provide novel insights into regulation of actin-based motility. *Mol. Biol. Cell* (2015) doi:10.1091/mbc.e15-06-0352.

49. Manhart, A. *et al.* Reconstitution of the equilibrium state of dynamic actin networks. *bioRxiv* 437806 (2018) doi:10.1101/437806.

50. Suarez, C. & Kovar, D. R. Internetwork competition for monomers governs actin cytoskeleton organization. *Nature Reviews Molecular Cell Biology* (2016) doi:10.1038/nrm.2016.106.

51. Antkowiak, A. *et al.* Sizes of actin networks sharing a common environment are determined by the relative rates of assembly. *PLOS Biol.* **17**, e3000317 (2019).

52. Balcer, H. I. *et al.* Coordinated Regulation of Actin Filament Turnover by a High-Molecular- Weight Srv2/CAP Complex, Cofilin, Profilin, and Aip1. *Curr. Biol.* (2003) doi:10.1016/j.cub.2003.11.051.

53. Bertling, E., Quintero-Monzon, O., Mattila, P. K., Goode, B. L. & Lappalainen, P. Mechanism and biological role of profilin-Srv2/CAP interaction. *J. Cell Sci.* (2007) doi:10.1242/jcs.000158.

54. Freeman, N. L., Chen, Z., Horenstein, J., Weber, A. & Field, J. An actin monomer binding activity localizes to the carboxyl-terminal half of the Saccharomyces cerevisiae cyclase-associated protein. *J. Biol. Chem.* (1995) doi:10.1074/jbc.270.10.5680.

55. Gottwald, U., Brokamp, R., Karakesisoglou, I., Schleicher, M. & Noegel, A. A. Identification of a cyclase-associated protein (CAP) homologue in Dictyostelium discoideum and characterization of its interaction with actin. *Mol. Biol. Cell* (1996) doi:10.1091/mbc.7.2.261.

56. Nomura, K., Ono, K. & Ono, S. CAS-1, a C. elegans cyclase-associated protein, is required for sarcomeric actin assembly in striated muscle. *J. Cell Sci.* (2012) doi:10.1242/jcs.104950.

57. Hliscs, M. *et al.* Structure and function of a G-actin sequestering protein with a vital role in malaria oocyst development inside the mosquito vector. *J. Biol. Chem.* (2010) doi:10.1074/jbc.M109.054916.

58. Gieselmann, R. & Mann, K. ASP-56, a new actin sequestering protein from pig platelets with homology to CAP, an adenylate cyclase-associated protein from yeast. *FEBS Lett.* (1992) doi:10.1016/0014-5793(92)80043-G.

59. Jansen, S., Collins, A., Golden, L., Sokolova, O. & Goode, B. L. Structure and mechanism of mouse cyclase-associated protein (CAP1) in regulating actin dynamics. *J. Biol. Chem.* (2014) doi:10.1074/jbc.M114.601765.

60. Zhang, H. *et al.* Mammalian adenylyl cyclase-associated protein 1 (CAP1) regulates cofilin function, the actin cytoskeleton, and cell adhesion. *J. Biol. Chem.* (2013) doi:10.1074/jbc.M113.484535.

61. Makkonen, M., Bertling, E., Chebotareva, N. A., Baump, J. & Lappalainen, P. Mammalian and malaria parasite cyclase-associated proteins catalyze nucleotide exchange on G-actin through a conserved mechanism. *J. Biol. Chem.* (2013) doi:10.1074/jbc.M112.435719.

62. Mattila, P. K. *et al.* A high-affinity interaction with ADP-actin monomers underlies the mechanism and in vivo function of Srv2/cyclase-associated protein. *Mol. Biol. Cell* (2004) doi:10.1091/mbc.E04-06-0444.

63. Chaudhry, F., Little, K., Talarico, L., Quintero-Monzon, O. & Goode, B. L. A central role for the WH2 domain of Srv2/CAP in recharging actin monomers to drive actin turnover in vitro and in vivo. *Cytoskeleton* (2010) doi:10.1002/cm.20429.

64. Nomura, K. & Ono, S. ATP-dependent regulation of actin monomer-filament equilibrium by cyclase-associated protein and ADF/cofilin. *Biochem. J.* (2013) doi:10.1042/BJ20130491.

65. Quintero-Monzon, O. *et al.* Reconstitution and dissection of the 600-kDa Srv2/CAP complex: Roles for oligomerization and cofilin-actin binding in driving actin turnover. *J. Biol. Chem.* (2009) doi:10.1074/jbc.M808760200.

66. Swiston, J., Hubberstey, A., Yu, G. & Young, D. Differential expression

of CAP and CAP2 in adult rat tissues. *Gene* (1995) doi:10.1016/0378-1119(95)00522-8.

67. Yu, G., Swiston, J. & Young, D. Comparison of human CAP and CAP2, homologs of the yeast adenylyl cyclase-associated proteins. *J. Cell Sci.* (1994).

68. Dodatko, T. *et al.* Crystal structure of the actin binding domain of the cyclase-associated protein. *Biochemistry* (2004) doi:10.1021/bi049071r.

69. Machesky, L. M. & Poland, T. D. Profilin as a potential mediator of membrane-cytoskeleton communication. *Trends Cell Biol.* (1993) doi:10.1016/0962-8924(93)90087-H.

70. Mockrin, S. C. & Korn, E. D. Acanthamoeba Profilin Interacts with G-Actin to Increase the Rate of Exchange of Actin-Bound Adenosine 5'-Triphosphate. *Biochemistry* (1980) doi:10.1021/bi00564a033.

71. Carlsson, L., Nyström, L. E., Sundkvist, I., Markey, F. & Lindberg, U. Actin polymerizability is influenced by profilin, a low molecular weight protein in non-muscle cells. *J. Mol. Biol.* (1977) doi:10.1016/0022-2836(77)90166-8.

72. Pantaloni, D. & Carlier, M. F. How profilin promotes actin filament assembly in the presence of thymosin β4. *Cell* (1993) doi:10.1016/0092-8674(93)90544-Z.

73. Goldschmidt-Clermont, P. J., Machesky, L. M., Doberstein, S. K. & Pollard, T. D. Mechanism of the interaction of human platelet profilin with actin. *J. Cell Biol.* (1991) doi:10.1083/jcb.113.5.1081.

74. Wolven, A. K., Belmont, L. D., Mahoney, N. M., Almo, S. C. & Drubin, D. G. In vivo importance of actin nucleotide exchange catalyzed by profilin. *J. Cell Biol.* (2000) doi:10.1083/jcb.150.4.895.

75. Dhont, J. K. G., Wiegand, S., Duhr, S. & Braun, D. Thermodiffusion of charged colloids: Single-particle diffusion. *Langmuir* (2007) doi:10.1021/la062184m.

76. Jerabek-Willemsen, M., Wienken, C. J., Braun, D., Baaske, P. & Duhr, S. Molecular interaction studies using microscale thermophoresis. *Assay and Drug Development Technologies* (2011) doi:10.1089/adt.2011.0380.

77. Seidel, S. A. I. *et al.* Microscale thermophoresis quantifies biomolecular interactions under previously challenging conditions. *Methods* (2013) doi:10.1016/j.ymeth.2012.12.005.

78. Baaske, P., Wienken, C. J., Reineck, P., Duhr, S. & Braun, D. Optical thermophoresis for quantifying the buffer dependence of aptamer binding. *Angew. Chemie - Int. Ed.* (2010) doi:10.1002/anie.200903998.

79. Zhou, G. L., Zhang, H., Wu, H., Ghai, P. & Field, J. Phosphorylation of the cytoskeletal protein CAP1 controls its association with cofilin and actin. *J. Cell Sci.* (2014) doi:10.1242/jcs.156059.

80. Chaudhry, F. *et al.* Srv2/cyclase-associated protein forms hexameric shurikens that directly catalyze actin filament severing by cofilin. *Mol. Biol. Cell* (2013) doi:10.1091/mbc.E12-08-0589.

81. Bertling, E., Quintero-Monzon, O., Mattila, P. K., Goode, B. L. & Lappalaines, P. Mechanism and biological role of profilin-Srv2/CAP interaction. *J. Cell Sci.* (2007) doi:10.1242/jcs.000158.

82. Martin, A. C. Pulsation and stabilization: Contractile forces that underlie morphogenesis. *Developmental Biology* (2010) doi:10.1016/j.ydbio.2009.10.031.

83. Lecuit, T., Lenne, P.-F. & Munro, E. Force Generation, Transmission, and Integration during Cell and Tissue Morphogenesis. *Annu. Rev. Cell Dev. Biol.* (2011) doi:10.1146/annurev-cellbio-100109-104027.

84. Vicente-Manzanares, M., Ma, X., Adelstein, R. S. & Horwitz, A. R. Non-muscle myosin II takes centre stage in cell adhesion and migration. *Nature Reviews Molecular Cell Biology* (2009) doi:10.1038/nrm2786.

85. Ma, X. *et al.* Nonmuscle myosin II exerts tension but does not translocate actin in vertebrate cytokinesis. *Proc. Natl. Acad. Sci. U. S. A.* (2012) doi:10.1073/pnas.1116268109.

86. Tinevez, J. Y. *et al.* Role of cortical tension in bleb growth. *Proc. Natl. Acad. Sci. U. S. A.* (2009) doi:10.1073/pnas.0903353106.

87. Guha, M., Zhou, M. & Wang, Y. L. Cortical actin turnover during cytokinesis requires myosin II. *Curr. Biol.* (2005) doi:10.1016/j.cub.2005.03.042.

88. Schirenbeck, A., Arasada, R., Bretschneider, T., Schleicher, M. & Faix,

J. Formins and VASPs may co-operate in the formation of filopodia. in *Biochemical Society Transactions* (2005). doi:10.1042/BST20051256.

89. Hotulainen, P. & Lappalainen, P. Stress fibers are generated by two distinct actin assembly mechanisms in motile cells. *J. Cell Biol.* (2006) doi:10.1083/jcb.200511093.

90. Elkhatib, N. *et al.* Fascin plays a role in stress fiber organization and focal adhesion disassembly. *Curr. Biol.* (2014) doi:10.1016/j.cub.2014.05.023.

91. Haviv, L., Gillo, D., Backouche, F. & Bernheim-Groswasser, A. A Cytoskeletal Demolition Worker: Myosin II Acts as an Actin Depolymerization Agent. *J. Mol. Biol.* (2008) doi:10.1016/j.jmb.2007.09.066.

92. Breitsprecher, D. *et al.* Molecular mechanism of Ena/VASP-mediated actin-filament elongation. *EMBO J.* (2011) doi:10.1038/emboj.2010.348.

93. Schirenbeck, A. *et al.* The bundling activity of vasodilator-stimulated phosphoprotein is required for filopodium formation. *Proc. Natl. Acad. Sci. U. S. A.* (2006) doi:10.1073/pnas.0511243103.

94. Damiano-Guercio, J. *et al.* Loss of ENA/VASP interferes with lamellipodium architecture, motility and integrin-dependent adhesion. *Elife* (2020) doi:10.7554/eLife.55351.

95. Lenz, M. Geometrical origins of contractility in disordered actomyosin networks. *Phys. Rev. X* (2014) doi:10.1103/PhysRevX.4.041002.

96. Sanchez, T., Chen, D. T. N., Decamp, S. J., Heymann, M. & Dogic, Z. Spontaneous motion in hierarchically assembled active matter. *Nature* (2012) doi:10.1038/nature11591.

97. Murrell, M. P. & Gardel, M. L. F-actin buckling coordinates contractility and severing in a biomimetic actomyosin cortex. *Proc. Natl. Acad. Sci. U. S. A.* (2012) doi:10.1073/pnas.1214753109.

98. Umemoto, S. & Sellers, J. R. Characterization of in vitro motility assays using smooth muscle and cytoplasmic myosins. *J. Biol. Chem.* (1990).

99. Breitsprecher, D. *et al.* Clustering of VASP actively drives processive, WH2 domain-mediated actin filament elongation. *EMBO J.* (2008) doi:10.1038/emboj.2008.211.

100. Ideses, Y., Sonn-Segev, A., Roichman, Y. & Bernheim-Groswasser, A. Myosin II does it all: Assembly, remodeling, and disassembly of actin networks are governed by myosin II activity. *Soft Matter* (2013) doi:10.1039/c3sm50309g.

101. Köster, D. V. *et al.* Actomyosin dynamics drive local membrane component organization in an in vitro active composite layer. *Proc. Natl. Acad. Sci. U. S. A.* (2016) doi:10.1073/pnas.1514030113.

102. Schuppler, M., Keber, F. C., Kröger, M. & Bausch, A. R. Boundaries steer the contraction of active gels. *Nat. Commun.* (2016) doi:10.1038/ncomms13120.

103. Koenderink, G. H. & Paluch, E. K. Architecture shapes contractility in actomyosin networks. *Current Opinion in Cell Biology* (2018) doi:10.1016/j.ceb.2018.01.015.

104. Wollrab, V. *et al.* Polarity sorting drives remodeling of actin-myosin networks. *J. Cell Sci.* (2019) doi:10.1242/jcs.219717.

105. Murrell, M., Thoresen, T. & Gardel, M. Reconstitution of contractile actomyosin arrays. in *Methods in Enzymology* (2014). doi:10.1016/B978-0-12-397924-7.00015-7.

106. Pollard, T. D. Electron microscopy of synthetic myosin filaments: Evidence for cross-bridge flexibility and copolymer formation. *J. Cell Biol.* (1975) doi:10.1083/jcb.67.1.93.

107. Lenz, M., Gardel, M. L. & Dinner, A. R. Requirements for contractility in disordered cytoskeletal bundles. *New J. Phys.* (2012) doi:10.1088/1367-2630/14/3/033037.

108. Lenz, M. Reversal of contractility as a signature of self-organization in cytoskeletal bundles. *Elife* (2020) doi:10.7554/eLife.51751.

109. Simon, C. *et al.* Actin dynamics drive cell-like membrane deformation. *Nat. Phys.* (2019) doi:10.1038/s41567-019-0464-1.

110. Dürre, K. *et al.* Capping protein-controlled actin polymerization shapes lipid membranes. *Nat. Commun.* (2018) doi:10.1038/s41467-018-03918-1.

111. Bleicher, P., Sciortino, A. & Bausch, A. R. The dynamics of actin network turnover is self-organized by a growth-depletion feedback. *Sci.*

Rep. **10**, 6215le (2020).

112. Manhart, A. *et al.* Quantitative regulation of the dynamic steady state of actin networks. *Elife* (2019) doi:10.7554/eLife.42413.

113. Senger, F. *et al.* Spatial integration of mechanical forces by α-actinin establishes actin network symmetry. *J. Cell Sci.* (2019) doi:10.1242/jcs.236604.

114. Chesarone, M. A. & Goode, B. L. Actin nucleation and elongation factors: mechanisms and interplay. *Current Opinion in Cell Biology* (2009) doi:10.1016/j.ceb.2008.12.001.

115. Samarin, S. *et al.* How VASP enhances actin-based motility. *J. Cell Biol.* (2003) doi:10.1083/jcb.200303191.

116. Young, L. E., Latario, C. J. & Higgs, H. N. Roles for Ena/VASP proteins in FMNL3-mediated filopodial assembly. *J. Cell Sci.* (2018) doi:10.1242/jcs.220814.

117. Bear, J. E. *et al.* Negative regulation of fibroblast motility by Ena/VASP proteins. *Cell* (2000) doi:10.1016/S0092-8674(00)80884-3.

118. Burnette, D. T. *et al.* A role for actin arcs in the leading-edge advance of migrating cells. *Nat. Cell Biol.* (2011) doi:10.1038/ncb2205.

119. Tojkander, S., Gateva, G., Husain, A., Krishnan, R. & Lappalainen, P. Generation of contractile actomyosin bundles depends on mechanosensitive actin filament assembly and disassembly. *Elife* (2015) doi:10.7554/eLife.06126.001.

120. Köhler, S., Schaller, V. & Bausch, A. R. Structure formation in active networks. *Nat. Mater.* (2011) doi:10.1038/nmat3009.

121. Sonal *et al.* Myosin-II activity generates a dynamic steady state with continuous actin turnover in a minimal actin cortex. *J. Cell Sci.* (2019) doi:10.1242/jcs.219899.

122. Yam, P. T. *et al.* Actin-myosin network reorganization breaks symmetry at the cell rear to spontaneously initiate polarized cell motility. *J. Cell Biol.* (2007) doi:10.1083/jcb.200706012.

123. Lehtimäki, J. I., Rajakylä, E. K., Tojkander, S. & Lappalainen, P. Generation of stress fibers through myosin-driven re-organization of the actin cortex. *bioRxiv* 2020.06.30.179283 (2020)

doi:10.1101/2020.06.30.179283.

124. Walcott, S. & Sun, S. X. A mechanical model of actin stress fiber formation and substrate elasticity sensing in adherent cells. *Proc. Natl. Acad. Sci. U. S. A.* (2010) doi:10.1073/pnas.0912739107.

125. Burridge, K. & Guilluy, C. Focal adhesions, stress fibers and mechanical tension. *Experimental Cell Research* (2016) doi:10.1016/j.yexcr.2015.10.029.

126. Tavares, S. *et al.* Actin stress fiber organization promotes cell stiffening and proliferation of pre-invasive breast cancer cells. *Nat. Commun.* (2017) doi:10.1038/ncomms15237.

127. Abu Shah, E. & Keren, K. Symmetry breaking in reconstituted actin cortices. *Elife* (2014) doi:10.7554/elife.01433.

128. Carvalho, K. *et al.* Actin polymerization or myosin contraction: Two ways to build up cortical tension for symmetry breaking. *Philos. Trans. R. Soc. B Biol. Sci.* (2013) doi:10.1098/rstb.2013.0005.

129. Deek, J., Maan, R., Loiseau, E. & Bausch, A. R. Reconstitution of composite actin and keratin networks in vesicles. *Soft Matter* (2018) doi:10.1039/c7sm00819h.

130. Maan, R., Loiseau, E. & Bausch, A. R. Adhesion of Active Cytoskeletal Vesicles. *Biophys. J.* (2018) doi:10.1016/j.bpj.2018.10.013.

131. Tsai, F. C. & Koenderink, G. H. Shape control of lipid bilayer membranes by confined actin bundles. *Soft Matter* (2015) doi:10.1039/c5sm01583a.

132. Pontani, L. L. *et al.* Reconstitution of an actin cortex inside a liposome. *Biophys. J.* (2009) doi:10.1016/j.bpj.2008.09.029.

133. Guevorkian, K., Manzi, J., Pontani, L. L., Brochard-Wyart, F. & Sykes, C. Mechanics of Biomimetic Liposomes Encapsulating an Actin Shell. *Biophys. J.* (2015) doi:10.1016/j.bpj.2015.10.050.

134. Dickinson, R. B. Models for actin polymerization motors. *Journal of Mathematical Biology* (2009) doi:10.1007/s00285-008-0200-4.

135. Heberle, F. A. & Feigenson, G. W. Phase separation in lipid membranes. *Cold Spring Harb. Perspect. Biol.* (2011) doi:10.1101/cshperspect.a004630.

136. Soloviov, D. *et al.* Functional lipid pairs as building blocks of phase-separated membranes. *Proc. Natl. Acad. Sci. U. S. A.* (2020) doi:10.1073/pnas.1919264117.